LBL-17624

Lawrence Berkeley Laboratory
UNIVERSITY OF CALIFORNIA

Accelerator & Fusion
Research Division

AN INTENSE NON-RELATIVISTIC CESIUM ION BEAM

M.C. Lampel
(Ph.D. Thesis)

February 1984

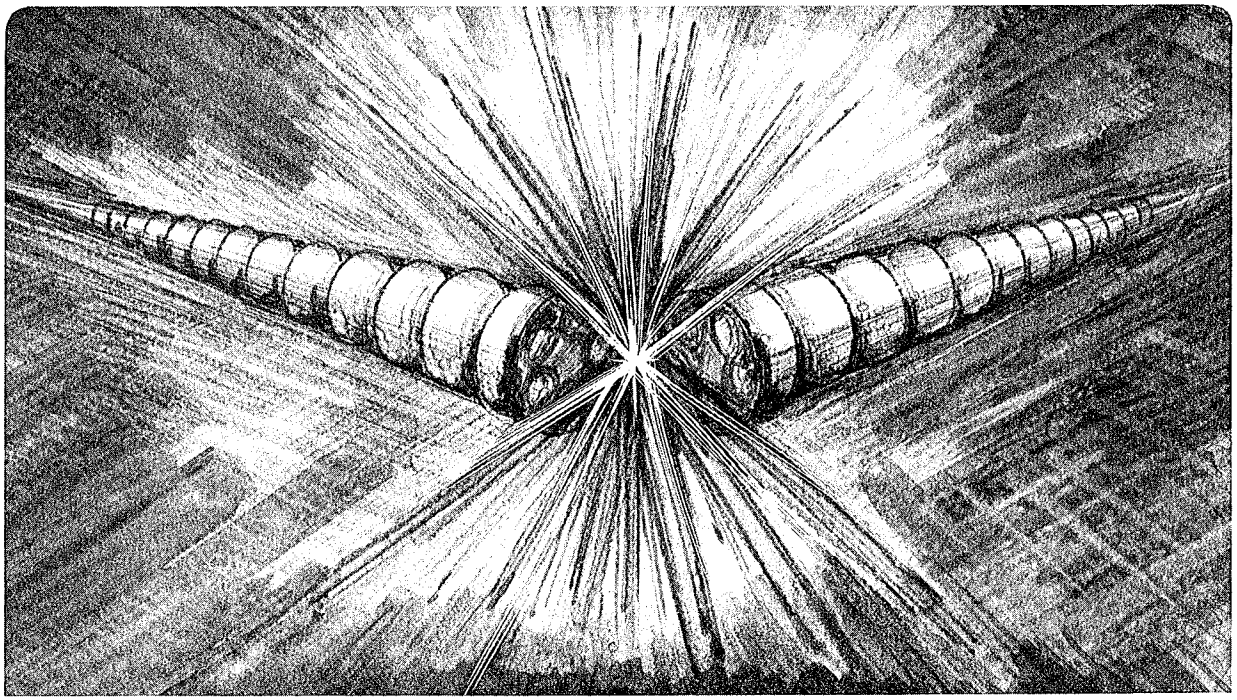

Prepared for the U.S. Department of Energy under Contract DE-AC03-76SF00098

LBL-17624

AN INTENSE NON-RELATIVISTIC CESIUM ION BEAM*

Michael Carl Lampel

Lawrence Berkeley Laboratory
University of California
Berkeley, California 94720

February 1984

* This work was supported by the Office of Energy Research, Office of Basic Energy Sciences, Department of Energy under Contract No. DE-AC03-76SF00098.

AN INTENSE NON-RELATIVISTIC CESIUM ION BEAM

Michael Carl Lampel

ABSTRACT

The Heavy Ion Fusion group at Lawrence Berkeley Laboratory has constructed the One Ampere Cesium Injector as a proof of principle source to supply an induction linac with a high charge density and high brightness ion beam. This is studied here. An electron beam probe was developed as the major diagnostic tool for characterizing ion beam space charge. Electron beam probe data inversion is accomplished with the EBEAM code and a parametrically adjusted model radial charge distribution. The longitudinal charge distribution was not derived, although it is possible to do so. The radial charge distribution that is derived reveals an unexpected halo of trapped electrons surrounding the ion beam. A charge fluid theory of the effect of finite electron temperature on the focusing of neutralized ion beams (Nucl. Fus. 21, 529 (1981)) is applied to the problem of the Cesium beam final focus at the end of the injector. It is shown that the theory's predictions and assumptions are consistent with the experimental data, and that it acounts for the observed ion beam radius of ~5 cm, and the electron halo, including the determination of an electron Debye length of ~10 cm.

Dr. Denis Keefe
Senior Staff Scientist
Lawrence Berkeley Laboratory
University of California
Berkeley, California

Wulf B. Kunkel
Professor of Physics
University of California
Berkeley, California

DEDICATION

In loving memory of my father,

J. Murray Lampel

who truly believed that education was a golden key

to the riches of the world.

ACKNOWLEDGEMENTS

I am very happy to take this opportunity to express my heartfelt gratitude to the many people who have aided me in the research, analysis, and writing of my thesis.

First I must thank my loving wife, Karen, for sticking by me and providing moral support even though this endeavor stretched out two years longer than I originally promised.

I offer my gratitude and thanks to my advisor, Dr. Denis Keefe, whose insistence on meticulous attention to detail has saved me from many errors and pitfalls in all stages of my work and writing, and without whose patient support I would never have been able to pursue research in the fascinating field of intense particle beams.

I owe much to Dr. Joseph Shiloh. He suggested the possibility of my developing the Electron Beam Probe and guided my first stumbling steps as an experimentalist, providing daily support and counsel. Many thanks.

My faculty advisor, Prof. Wulf Kunkel, deserves credit for taking upon himself the obligation of ensuring I performed work worthy of a doctoral candidate at the University of California. I have great admiration for his characteristic zeal and his deep knowledge of Plasma Physics.

My thanks to Dr. Richard Sah for pointing the way in the analysis of the Electron Beam Probe data. I would like to acknowledge the many helpful discussions with Drs. Lloyd Smith, L. Jackson Laslett, Edward Lee, Andy Faltens, Stephen Rosenblum, and Charles Kim, of L.B.L., and Drs. Les Thode and Don Lemons, of LANL. I would especially like to

thank Dr. David Judd for his introducing me to the subject of accelerator physics and his enthusiastic support for me in my pursuit of research in this field.

Thanks are due to Professors Ken Crowe and Michael Lieberman for serving on my thesis committee with interest in the subject and a kind regard for me.

I am grateful to Messrs. Chet Pike, Sandy Goss, Tom Purtell, and Augie Kruser for their help in all things electrical, and to Messrs. Dave Vanecek, C.P. Johnson, Ralph Hipple, Bill Ghiorso, and Ed Edwards for their help in all things mechanical. My thanks to Dr. Warren Chupp for imparting some of his vast knowledge of the nitty-gritty of experimental physics.

The camaraderie I enjoyed with my officemates, Mr. Michael Tiefenback, Mr. Geoffrey Krafft and Dr. David Douglas, in many hours of discussion of all matters relevant to physics and mankind will always be treasured.

I owe a large debt of gratitude to Mrs. Joy Kono, whose expert typing and unfailing good humor eased greatly the pain and tedium involved in preparing this manuscript.

Finally my love and gratitude to my family for being supportive through a lifetime of study, and especially to my mother and my father who started me off so well.

CONTENTS

		Page
I.	INTRODUCTION	1
	Conclusions, Results Summarized	3
	Overview of Inertial Confinement Fusion and the LBL Program	4
	Introduction and Thermonuclear Reaction: Lawson Crit.	4
	Achieving Fusion on Earth: Magnet Confinement and Inertial Confinement	6
	Heavy Ion Fusion	11
II.	THE DESCRIPTION OF THE APPARATUS	15
	The Cesium Injector	15
	Electron Beam Probe	19
	The Diagnostic Tank and Auxiliary Diagnostics	21
	Diagnostic Tank	22
	Large Faraday Cup	22
	Small Faraday Cup	23
	Bias Cylinder	24
III.	OPERATION OF THE ELECTRON BEAM PROBE	27
	Introduction	27
	Principles of Electron Beam Probe Operation	28
	The EBEAM Code	29
	Model Distributions	33
	Simple Harmonic Oscillator	35

Page

The Applicability of the Two-Dimensional Simulation to the Three Dimensional Problem: The Three-Dimensional Simulation 41

IV. THE EXPERIMENTAL DATA 43

Experimental Errors 44

Demonstration of the Existence of Negative Charge 48

Model Distributions Used 50

The First Experimental Configuration 52

The Second and Third Experimental Configurations 52

Neutralization Experiment 55

Time Resolved Electron Beam Probe Data 56

Summary 58

V. THEORY OF THE ELECTRON DISTRIBUTION 59

Cesium Beam Neutralization 59

The Invariance of the Debye Length 62

Basic Equations for Electron Equilibria 65

Applicability to the Cesium Ion Beam 68

The Unlikelihood of a Hollow Electron Distribution 71

Effect of Partial Neutralization Upon the Ion Beam Envelope 73

Conclusion and Summary 74

REFERENCES 77

LIST OF TABLES

		Page
Table 1.1	Fusion Reactions	5
Table 1.2	Driver Requirements for Power Production	11
Table 3.1	Comparison of Theory and Code Deflection Calculation	40
Table 4.1	Ion Beam Line Charge and Percent Neutralization . .	45
Table 4.2	Ion Beam Radial Charge Distributions Derived from EBP Data Using EBEAM	46
Table 5.1	Electron Gas Parameters	70

LIST OF FIGURES

		Page
Figure 1.1	One Ampere Cesium Ion Source with EBP and SFC in the Diagnostic Tank	79
Figure 1.2	D-T Targets: Crosssectional View	80
Figure 2.1	Transients in Cesium Current Pulse	81
Figure 2.2	Cesium Current Pulse with Transients Eliminated . .	82
Figure 2.3	Three-Quarter View of the Diagnostic Tank with EBP, LFC, SFC, and Voltage Cylinder	83
Figure 2.4	EBP Electron Gun	84
Figure 2.5	HIF EBP Electron Gun Power Supply Schematic	85
Figure 2.6	Electron Gun Wiring Schematic	86
Figure 2.7	EBP Electron Gun with Sleeve	87
Figure 2.8	The Large Faraday Cup (LFC)	88
Figure 2.9	The Small Faraday Cup (SFC)	89
Figure 2.10	R-Θ Probe Support Rails	90
Figure 3.1	End View of the Diagnostic Tank Showing EBP	91
Figure 3.2	Example Data Set of EBP Traces	92
Figure 3.3	Rectangular, Gaussian, and Bennett Radial Distribution Functions	93
Figure 3.4	EBEAM Code Calculation of Azimuthal Deflection vs. Electron Gun Angle for the Gaussian Distribution . .	94
Figure 3.5	EBEAM Code Calculation of Azimuthal Deflection vs. Electron Gun Angle for the Rectangular Distribution	95
Figure 3.6	EBEAM Code Calculation of Azimuthal Deflection vs. Electron Gun Angle for the Bennett Distribution . .	96
Figure 3.7	Geometry for the Analysis of Small Angle Deflections	97
Figure 3.8	3-D EBEAM Code Calculation of Longitudinal and Azimuthal Deflection (a Trace) for an Electron Gun Angle of 35°	98
Figure 3.9	2-D and 3-D Azimuthal Deflections Calculated by EBEAM Compared	99

		Page
Figure 4.1	6-1-82 Data: Azimmuthal Deflection vs. Electron Gun Angle	100
Figure 4.2A	6-1-82 Azimuthal Data and the Best Computer Fit . .	101
Figure 4.2B	Model Charge Distribution Giving Best Fit to 6-1-82 Data	101
Figure 4.3A	6-2-82 Azimuthal Deflection Data and the Best Computer Fit	102
Figure 4.3B	Model Charge Distribution Giving Best Fit to 6-2-82 Data	102
Figure 4.4	Azimuthal Deflection vs. Voltage Cylinder Bias at 4.9° E-Gun Angle	103
Figure 4.5	Pearson Probe Current Measuring Electron Energy Distribution for Configuration III	104
Figure 4.6A	9-1-82 Azimuthal Deflection Data and the Best Computer Fit Using Two Gaussian Distribution Functions	105
Figure 4.6B	Two Gaussian Model Charge Distribution Giving the Best Fit to 9-1-82 Azimuthal Deflection Data . . .	105
Figure 4.7A	9-1-82 Azimuthal Deflection Data and the Best Computer Fit Using a Gaussian and R^2 x Gaussian Distribution Functions	106
Figure 4.7B	Gaussian + R^2 x Gaussian Model Charge Distribution Giving the Best Fit to 9-1-82 Azimuthal Deflection Data	106
Figure 4.8A	9-1-82 Azimuthal Deflection Data and the Best Computer Fit Using a Trapezoidal and R^2 x Gaussian Distribution Functions	107
Figure 4.8B	Trapezoidal + R^2 x Gaussian Model Charge Distribution Functions	107
Figure 4.9	Gaussian Fit to SFC Measurements	108
Figure 4.10A	6-14-82 Azimuthal Deflection Data and Best Computer Fit	109
Figure 4.10B	Model Charge Distribution Giving Best Fit to 9-1-82A Data	109
Figure 4.11A	9-1-82A Azimuthal Deflection Data and Best Computer Fit	110

Page

Figure 4.11B Model Charge Distribution Giving Best Fit to 9-1-82A Data 110

Figure 4.12A 9-2-82 Azimuthal Deflection Data and Best Computer Fit 111

Figure 4.12B Model Charge Distribution Giving Best Fit to 9-2-82 Data 111

Figure 4.13 Configuration I: Pearson Probe Current Measuring Electron Energy Distribution . . . 112

Figure 4.14 Configuration II: Pearson Probe Current Measuring Electron Energy Distribution . . 113

Figure 4.15 Azimuthal Deflection vs. Voltage Cylinder Bias at 16° E-Gun Angle 114

Figure 4.16 Azimuthal Deflection vs. Voltage Cylinder Bias at 32.5° E-Gun Angle 115

Figure 4.17A 6-30-82 Azimuthal Deflection Data and the Best Computer Fit 116

Figure 4.17B Model Charge Distribution Giving the Best Fit for 6-30-82 Data 116

Figure 4.18A 6-30-82A Azimuthal Deflection Data and the Best Computer Fit 117

Figure 4.18B Model Charge Distribution Giving the Best Fit for 6-30-82A Data 117

Figure 4.19A 6-30-82B Azimuthal Deflection Data and the Best Computer Fit 118

Figure 4.19B Model Charge Distribution Giving the Best Fit for 6-30-82B Data 118

Figure 4.20A 6-30-82C Azimuthal Deflection Data and the Best Computer Fit 119

Figure 4.20B Model Charge Distribution Giving the Best Fit for 6-30-82C Data 119

Figure 4.21 A Time Resolved Trace 120

Figure 5.1 Electrons Streaming into Cesium Ion Beam 121

Figure 5.2 An Electron Trajectory in the Cesium Beam 122

		Page
Figure 5.3A	Electron Trajectory in a Circular "Waterbag" Potential	123
Figure 5.3B	Electron Trajectory in a Stadium "Waterbag" Potential	124
Figure 5.4A	Radial Electron Charge Distribution for a Rectangular Radial Ion Charge Distribution for $R/\lambda_D = 1$	125
Figure 5.4B	Radial Electron Charge Distribution for a Rectangular Radial Ion Charge Distribution for $R/\lambda_D = 10$	125
Figure 5.5	Radial Electron Charge Distribution for the Rigid Rotor Electron Model with $\omega << \omega_p/2$	126
Figure 5.6	Radial Electron Charge Distribution for the Rigid Rotor Electron Model with $\omega \simeq \omega_p/2$	127
Figure 5.7	Solutions to the RMS Focal Spot Equation (Eq. 13), in Terms of Dimensionless Parameters R_F/R_O, R_O/λ_D, and $\tan^2 \psi/k$. R_F is the Focused Beam Radius, R_O is the Initial Beam Radius, λ_D is the Electron Debye Length, ψ is the Beam Focal Angle, and k is the Ion Beam Perveance	128

Chapter I - INTRODUCTION

Intense ion beams are interesting because of their great promise as drivers for inertial confinement fusion (ICF). Multiple intense beams of heavy ions with several GeV kinetic energy per ion and total power in the 100 TW range focused onto a deuterium-tritium pellet for a duration of ~20 ns is one scenario which may produce a successful thermonuclear burn in a manageable microexplosion. This goal places stringent requirements on the ion beams to have low emittance, high current, and small energy spread.

As part of the development program for such beams the Heavy Ion Fusion group at the Lawrence Berkeley Laboratory has developed a prototype ion injector capable of supplying a low energy high quality cesium beam to an accelerator. This machine is called the One Ampere Cesium Injector (Fig. 1.1). It is designed to supply one ampere of Cs^+ ions at 2 MeV kinetic energy with nearly uniform density and laminar flow focused to a radius of 7-8 cm. It is a three stage drift tube accelerator. The drift tube lengths are picked to allow for a 3 μs long pulse. As shown the beam waist is designed to occur near the end of the third drift tube. The major diagnostics are located in the diagnostic tank downstream of the accelerator.

Naturally, a major effort to characterize the actual beam produced was a large part of the injector development. Diagnostic tools included large and small Faraday cups, scintillators used with an optical multi-channel analyzer (OMA), and the Electron Beam Probe (EBP). These diagnostic devices were used to measure ion beam emittance, current, space charge distribution, and the beam envelope. The

scintillator and OMA, and the Faraday cups are standard diagnostic devices for measuring these beam characteristics. The Electron Beam Probe (EBP) was developed as an independent tool for determining total current and the space charge distribution. Unlike the other devices it is a non-destructive ion beam diagnostic, enabling its simultaneous use with another device, such as the large Faraday cup.

Electron beams have been used from time to time in the past as probes for plasmas. Uses have included detection of plasma waves (Ref. 1.1) and examination of plasma potential well structure (Ref. 1.2). A Russian paper (Ref. 1.3) suggests a method of utilizing an electron beam to probe both the magnetic and electric fields of an ion beam with cylindrical symmetry. However, until now an electron beam probe has not been applied to the measurement of a partially neutralized ion beam with the intent of determining ion and electron charge distribution. So this probe enables a look into the regime of non-neutral non-uniform plasmas.

The EBP is sensitive to space charge density and there is no need (or way) to render the probe insensitive to any electron space charge present. In contrast, a Faraday cup measuring ion current must be insensitive to any electrons present if it is to work correctly. This particular difference between measurements with the EBP and the small, movable Faraday cup led to the discovery and examination of a trapped halo of secondary electrons present in the Cs^+ beam.

The examination of this halo and the ion beam, the origin of the halo, and a theoretical model for halo-ion beam dynamics whose predictions are compared with experiment comprise the heart of this dissertation. This is of interest for two reasons: (1) For proper

acceleration the total space charge present must be strictly controlled. This is most easily accomplished by elimination of all electrons. (2) The understanding of the halo-ion beam system may have a bearing on the question of the final focusing of an ion beam, neutralized by electrons with finite temperature, onto a DT target.

Conclusions, Results Summarized

A self consistent picture of how the ion beam generates and maintains its halo of trapped electrons can be understood as follows. The ion beam when it is roughly thirty centimeters in diameter passes through a strongly focusing grid mounted on a 30 cm diameter drift tube. Some small fraction of the ions which are lost to the beam generate secondary electrons off the grid and drift-tube surfaces. Roughly 80% of the ion beam space charge is neutralized this way. The electrons very rapidly become isotropic and have a "temperature" about equal to the remaining potential of the ion beam, a few hundred electron volts.

As the ion beam continues to drift it is focusing. The change in potential as this happens does work on the electrons, heating them. In fact, the heating occurs in such a way that the Debye length of the electrons is a constant. For the case at hand $\lambda_D \sim 1/2\, R_b$, R_b = original RMS ion beam radius. As the radius of the ion beam becomes less than the electron Debye length the electrons no longer contract with the beam. As the ion beam contracts even more, a core of high density ions appears in a halo of low density electrons, just what is seen empirically.

This model will be examined for consistency with the experimental data in chapter five. Before that the experimental apparatus and operation will be outlined in chapter two, electron beam probe optics in chapter three, and the empirically fitted experimental data in chapter four. This chapter concludes with a brief discussion of the inertial confinement fusion program.

OVERVIEW OF INERTIAL CONFINEMENT FUSION AND THE LBL PROGRAM

Introduction and Thermonuclear Reaction: Lawson Criterion

While the work done for this thesis was performed within the framework of the Heavy Ion Fusion group at the Lawrence Berkeley Laboratory, in a larger sense the framework includes the national and international effort directed toward inertial confinement fusion. A short summary of this effort is appropriate. A detailed review is given by Keefe (Ref. 1.7).

Thermonuclear fusion of light nuclei offers promise as long term energy source because of the tremendous energy available in a small amount of fuel. The whole effort of research is directed toward igniting the fuel and controlling the burn so that neither too much nor too little energy is produced at a given time.

A variety of candidate reactions that have been considered are shown in Table 1.1 (Ref. 1.4). The prime candidate for the first commercial controlled thermonuclear burn is the reaction $D+T \rightarrow {}^{4}He+N$ yielding 17.6 MeV per reaction and having the greatest yield compared to input energy of any of the listed reactions. Just as important for a first attempt is that it requires the lowest plasma temperature to start. Later systems may move to reactions producing only charged

TABLE 1.1 Fusion Reactions

	Reaction energy (MeV)	Threshold plasma temperature (keV)	Maximum energy gain per fusion
$D + T \rightarrow {}^4He + N$	17.6	4	1800
$D + D \rightarrow {}^3He + N$	3.2	50	70
$D + D \rightarrow T + P$	4.0	50	80
$D + {}^3He \rightarrow {}^4He + P$	18.3	100	180
${}^6Li + P \rightarrow {}^3He + {}^4He$	4.0	900	6
${}^6Li + D \rightarrow {}^7Li + P$	5.0	> 900	6
${}^6Li + D \rightarrow T + {}^4He + P$	2.6	> 900	3
${}^6Li + D \rightarrow 2({}^4He)$	22.0	> 900	22
${}^7Li + P \rightarrow 2({}^4(He)$	17.5	> 900	18
${}^{11}B + P \rightarrow 3({}^4He)$	8.7	300	30

particles so that more efficient direct conversion to electrical energy may be possible.

For a successful deuterium-tritium thermonuclear burn two conditions need to be satisfied simultaneously: One, the plasma temperature should be near $kT = 20$ KeV. Two, the hot plasma must remain hot and confined long enough for a significant amount of fuel to burn. This last is related to the Lawson criterion. Quite simply it can be shown that in the initial stages

$$\frac{\text{Energy out}}{\text{Energy in}} \quad 2\times10^{-13}\ n\tau \quad (cm^{-3})$$

where n is particle density (cm^{-3}) and τ is the confinement time (sec.). Thus the Lawson criterion for scientific breakeven:

$$n\tau \gtrsim 5 \times 10^{12} \text{ cm}^{-3} \text{ s} .$$

While for an economically feasible commercial reactor:

$$n\tau \cong 10^{15}$$

Achieving Fusion on Earth: Magnetic Confinement and Inertial Confinement

On the earth two methods of plasma confinement and heating present themselves, in historical order, inertial confinement and magnetic confinement. Large scale inertial confinement was shown to be a success with the explosions of the first hydrogen bombs. At the time no feasible method of scaling this process to manageable proportions for commercial power plant operation was known. Thus hope came for harnessing this power from the concept of magnetic confinement. The underlying principle of magnetic confinement is to satisfy the Lawson criterion by maximizing τ, the confinement time, while allowing n, the density, to remain small -- a tiny fraction of atmospheric density. After more than three decades of work overcoming physical and technological barriers completely unguessed at in the beginning, the realization of scientific breakeven in a magnetic confinement vessel is expected in the U.S. with the operation of the Tokamak Fusion Test Reactor, TFTR. Other countries, working alone or collaboratively expect to achieve this goal on similar machines very soon as well.

Exciting as achieving scientific breakeven is it is not the goal of these programs. That goal is providing an economically competitive power plant based on the enormous potential energy supply reliance on hydrogen isotopes can provide. It is the economics of power production and reactor design from which the rekindled interest in inertial confinement fusion derives motivation now.

The concept of imploding a small pellet of nuclear fuel to create a "microexplosion" releasing several megajoules was first proposed by the laser community early on (Ref. 1.5). At the time lasers seemed an ideal driver capable of delivering easily focused intense pulses of radiation to provide power densities great enough to compress matter to one thousand times solid density and hold it there long enough for a significant burn. Confidence was high that one decade could see development of both target designs and lasers showing scientific breakeven and leading to rapid commercial development.

A pellet, or target, is a small sphere containing the D-T fuel (Fig. 1.2). In fact there are many possible designs which one might use depending upon the characteristics of the driving pulse and the desired yield. For instance, aside from the fuel, the materials in and thicknesses of surrounding layers vary considerably between a design developed for a laser driver or a heavy ion beam. Still, targets fall into two major classes "single-shell" and "double-shell" (Fig. 1.2). Each has an outer layer of ablative material. Just as in a rocket, when energy from laser light or short range ions is deposited there, the ablative material is ejected, creating an inward force upon the remaining material. In the single shell design there may be several layers within, with the fuel always the innermost layer. Under ideal

conditions compressional heating can be quite modest (on average ~ 200 eV) but a small volume in the center can be raised to ~ 20 keV by the converging shock wave created in the fuel. This is the condition necessary for ignition to occur at the center and a burn wave due to α-particle heating to pass into the rest of the fuel. The double-shell design is a modification in which a shell of dense material, containing D-T fuel, is suspended in the center. Thus, the imploding outer shell collides with and transfers energy to the inner shell, driving the inner fuel to ignition. The burn wave then propagates outward to the main fuel layer and ignites it. Double shelled targets of multiple layers have also been considered.

Laser target interactions are far more complex than originally contemplated (Ref. 1.6). Coupling laser beam energy into the target is much less efficient than originally hoped with best coupling occurring at a wavelength a fraction of a nanometer. Lasers have been developed to operate at such frequencies but the optics of such a system is formidable. Moreover the efficiency of such lasers is not expected to exceed 5% by very much, if at all. Together with the low coupling efficiency noted above, this means extremely powerful lasers will be needed for ignition. Keefe (Ref. 1.7) points out that the major problem facing the laser is that operation with favored double-shell targets will demand an energy input per pulse approaching 10 MJ following the best estimates, 100 times the energy of the originally proposed Nova glass laser (Ref. 1.8) and thus would carry far too high a price tag for commercial operation.

Nevertheless, laser fusion research is continuing in this country primarily at the Lawrence Livermore National Laboratory where Novette (a scaled down Nova) will continue to be used in beam pellet studies.

Proposals from the accelerator community for the use of particle beams (Ref. 1.9) emphasized that not only would an intense beam of high energy heavy ions provide a particularly effective driver for pellet implosion, but that several decades of accelerator development and operation could be capitalized upon to greatly shorten the engineering steps between scientific breakeven and a working power plant. Still, physics issues concerning the pellet must be resolved, as well as proving the feasibility of applying accelerator technology successfully.

The central issue for the pellet physics is whether a small amount of D-T fuel can be burned successfully under laboratory conditions. The major driver issue, as can be appreciated from the laser fusion community's difficulties, is the ability to couple energy from the beam to the surface layers of the pellet.

Successful implosion occurs, given proper target design, when the driver, laser or particle beam, supplies the following: 1) A specific energy deposition into the pusher of $\sim 20\ MJg^{-1}$. 2) A total energy of $Q \approx 1$ MJ, an order of magnitude more than required for an ideal implosion, after accounting for fluid instabilities, imperfections in the target, and illumination asymmetries. 3) Focused power on the order of $\sim 2 \times 10^{14}\ W/cm^2$. 4) A shaped pulse rising from an initial low power to peak for the last 10 ns or so. For a commercial power plant it is necessary for the driver to have a high repetition rate (1-10 Hz), high efficiency (10-30% or more), long lifetime, and long term reliability.

While beam-pellet interactions will determine the ultimate utility of using particle beams, and is a major research area for any program, other considerations play a crucial role in determining what type accelerator and what type of particle are best suited for ICF. These considerations lead to driver requirements for power production as shown in Table 1.2 (Ref. 1.7). These requirements are based on consideration of beam-pellet interactions, the implosion dynamics, and the need to provide economical electrical power to the nation.

As just mentioned, successful implosion of a target demands an irradiance $S \sim 2 \times 10^{14}$ Wcm^{-2}, a specific energy deposition $W \sim 20$ MJg^{-2}, and a time scale $t \sim 10^{-8}$ s. Now $W = St/R$, where R is the particle range in gcm^{-2}. It can be shown that because of the necessary irradiance, energy deposition, and time scale the range of any ion is constrained to $R = 0.1$ gcm^{-2}. This leads to dramatic differences in beam current and kinetic energy required, depending on the mass of the ion. Typical specifications are (Ref. 17):

1) for electrons: ~ 1 MeV and 100 megamperes;
2) for protons: ~ 5 MeV and 20 megamperes;
3) for heavy ions ($A > 200$): ~ 10 GeV and 20 kiloamperes.

It has been pointed out that a laser capable of producing 10 MJ per pulse might have a prohibitive cost. At the other end pulsed power technology can cheaply and efficiently provide the energy and power needed using light ion beams. A major program is ongoing at Sandia National Laboratory to investigate this approach. At present the major obstacles to overcome are:

1. Space charge forces of megamperes of protons (or any light ion) at energies at or below 10 MeV.

2. Large beam emittance (transverse phase space (x,x',y,y')) limiting focal spot size.

3. The single pulse nature of the pulse power technology being used.

At this point in time it seems real breakthroughs in physics understanding and advances in technological expertise are needed to solve these problems.

TABLE 1.2 Driver Requirements for Power Production

Energy - 1 to 10 MJ
Power - 100 to 600 TW
Pulse shape - control needed
(Driver efficiency) x (target gain) = $\eta G > 10$
Focusing - to a few millimeters at 5 to 10 m from the reactor wall
Reliability - > 80 on-time
Lifetime - 30 years
Repetition rate - 1 to $10 s^{-1}$
Cost - (a few) x 10^8 $ per GWe of electrical output

HEAVY ION FUSION

The remaining major effort addressing inertial confinement fusion revolves around the concept of using heavy ions to produce a driver.

Space charge defocusing forces are reduced by orders of magnitude. For not only are heavy ion beams stiffer with respect to a given space charge field due to their much higher mass but because, for instance, kiloamps of 10 GeV ^{207}Pb provide the same power as mega-amps of 10 MeV protons the total space charge is less by several orders of magnitude. Thus, kiloamps of high kinetic energy heavy ions are much easier to focus than protons, opening up the possibility of using conventional accelerator technology to provide a driver.

Thus a heavy ion beam seems the best choice as a driver. Of course, this method still needs to be proven. Are there unexpectedly complex ion-target interactions? Is there an accelerator technology that can economically accelerate beams of heavy ions to currents of kiloamperes and particle energies of several GeV? The answer to the first question can be (and is) explored using conventional accelerators such as the Bevalac at Lawrence Berkeley Laboratory. The answer to the second is being sought in the R and D programs sponsored in the U.S. by the Department of Energy.

At Berkeley we in the Heavy Ion Fusion group have pursued the development of the linear induction accelerator as a promising answer to the second question. Induction linacs can be very efficient (> 25%) and can handle multi-kiloamperes of current in a conceptually simple design requiring a beam, or several beams, to be accelerated in a single pass through the accelerator and then aimed at and focused onto the pellet. This type of accelerator is capable of the necessary repetition rate, and if multiple beams were accelerated simultaneously an elimination of emittance degrading beam manipulations could be achieved.

An induction linac does need an injector to provide a beam with particle energy 3 ~ 10 MeV because at very low velocities the cost of induction acceleration is high. The Cs^{+1} 1 Amp 2 MeV Injector is a prototype of such an injector.

In transporting, accelerating, and focusing these intense beams two beam characteristics are critical; emittance and space charge. Emittance of a beam is the area occupied in (x,x',y,y',z,z') phase space, where the angle $x' \equiv dx/ds$ with s as the path the beam centroid follows. Generally z is taken as the beam path, with energy spread and timing errors replacing (z'). The quantities (x,x'), (y,y') are generally considered independent. Together the two pairs (x,x'), (y,y') are labeled transverse emittance. Energy and timing errors can affect the beam in many ways. Transverse emittance plays a key role as well in determining instabilities and in putting constraints on focusing the beam; for instance, with a given distance a beam must travel through a reaction chamber to a pellet, the emittance determines how large the beam must be to begin with, if it is to focus to a spot the size of the pellet.

Now, space charge is also a key characteristic in determining beam instabilities (through betatron tune depression) and focusing constraints. Space charge may be one of the toughest problems to overcome in achieving HIF as it is in Light Ion Fusion. Several ideas have been put forward on neutralization of ion beams to enhance focusing by reducing space charge forces.

The HIF group at Berkeley has designed several experiments to explore some of these problems in preparation of construction of a proof-of-principle heavy ion induction linac. The Single Beam

Transport Experiment explores a range of parameters for a high space charge beam to check various instabilities predicted by theory and simulation (Ref. 1.10) for an electrostatic focusing channel. The Neutralized Beam Focusing Experiment examines a novel method of strong focusing by neutralizing an ion beam with cold electrons and then applying a solenoid magnetic field (Ref. 1.11). The 1 Ampere Cesium Injector demonstrates production, acceleration, and focusing of an intense Cs^+ beam to a point suitable for injection into an induction linac (Ref. 1.10). The Long Pulse Induction Unit has demonstrated acceleration of that beam once it has left the injector (Ref. 1.11). The program is now moving on the design of a high temperature experiment (Ref. 1.12). The goal of this experiment is the heating of a target plasma to greater than 50 eV enabling study of ion plasma interactions.

Chapter 2 - DESCRIPTION OF THE APPARATUS

This chapter covers descriptions of the HIF Cesium Injector and its design and operation and the design and operation of the diagnostic devices used to acquire the data analyzed in this thesis. These topics will be covered in the following order: The Cesium Injector. Then the Electron Beam Probe. Next, the placement of the diagnostics in the diagnostic tank. Finally, the auxiliary diagnostics used: the large Faraday cup, the small Faraday cup, the Electron Beam Probe (EBP), and the Bias Cylinder.

The Cesium Injector

The Heavy Ion Fusion Group of the Lawrence Berkeley Laboratory has constructed a large aperture contact ionized Cs^{+1} ion source and drift tube linac as a cesium ion injector prototype. The system configuration is shown in Fig. 1.1. A contact-ionization (Ref. 2.1) ion source was chosen because in principle it is very bright. The contact ionization source is a 28 cm diameter iridium coated plate, heated by filaments placed behind, to a temperature of 1200°K-1400°K. The plate is supplied with neutrals from a water-cooled Cs metal reservoir. A spark plug above the reservoir is fired into it vaporizing Cs which is sprayed onto the hot plate. Most of the cesium atoms are adsorbed on the surface as ions. The emission rate is dependent upon the fractional coverage of the anode (hot plate) with cesium atoms and on the temperature of the anode.

The Cs^{+1} injector was designed with the aid of Herrmannsfeldt's EGUN code (Ref. 2.3). The object of the design was to transport and

accelerate a beam of ions to 1 ampere at 2 MeV. The optics were chosen to provide the required current focused to a small (~ 8 cm radius) waist that would allow the beam to enter the smaller aperture of induction modules for further acceleration.

When the diode (the first accelerator gap) is in space charge limited operation, where the Child-Langmuir current is less than the emission limit, the beam is uniform in the transverse direction and is insensitive to the non-uniformities of the Cs coverage and of the anode temperature. The Pierce electrode enhances the extracted beams uniformity and allows the beam to propagate across the gap without suffering expansion due to the high space charge present. The applied voltage across the gap is obtained by simultaneously pulsing the anode (hot plate) positive and the cathode (first drift tube with grid) negative. Crowbars on both cut off the voltage pulse and thus the Cs beam.

An ion transit time through the first acceleration gap is roughly one microsecond. So large transient current fluctuations are possible through a large fraction of the 3 μs pulse. In fact transients occurred through a large fraction of the Cs beam (Fig. 2.1). However, by properly tailoring the voltage transients are effectively suppressed (Fig. 2.2). It has been found (Ref. 2.2) that this is accomplished by applying a time dependent voltage pulse approximating the analytic form:

$$V = V_0 \left[\frac{4}{3}\left(\frac{t}{\tau}\right) - \frac{1}{3}\left(\frac{t}{\tau}\right)^4 \right] \quad \text{for} \quad t < \tau; \quad V = V_0 \quad \text{for} \quad t \geq \tau \, .$$

Once the beam is generated it passes into the first of three stainless steel 60 cm diam. drift tubes. The second and third drift tubes are progressively longer because the beam is lengthened as it is accelerated. The second acceleration occurs in the gap between drift tube 1 (DT1) and drift tube 2 (DT2) when DT1 is grounded through its crowbar and DT2 is pulsed negatively by its Marx generator. All pulse power for acceleration is provided by four 500,000 volt Marx generators, one for the source and one each for the three drift tubes. They are all controlled, as are the crowbars, through several stages of switches by a single master timer which the operator sets. When the beam head reaches the end of the second drift tube the second drift tube is crowbarred to ground and the third drift tube is pulsed to negative voltage. When the beam head reaches the end of the third drift tube it is crowbarred and the beam then drifts into the diagnostic tank, or induction modules.

The beam is focused as it passes through the acceleration gaps between drift tubes. At the front end of each drift tube is a grid (98%, 98% and ~ 88% transparent respectively). The first two are flat and the last curved (in both vert. and horiz. dimensions). The third grid is curved to provide the strong electrostatic focusing needed to bring the beam radius from nearly 26 cm to an 8 cm waist where it would enter either induction modules (since installed) for additional acceleration or the diagnostic tank. Control of the focusing, and hence the beam envelope, is achieved by altering the firing and crowbarring times of the three drift tubes with respect to each other through the master timer. This was the method of "tuning" the accelerator when beam

quality eroded over running periods of a few weeks due to line voltage drift, and changes in Marx and crowbar firing for unknown reasons.

The pressure in the system was typically 2×10^{-6} Torr with an operating range from ~ 5×10^{-7} - 7×10^{6} Torr. The lower limit was set by ultimate pump speed (including an LN cryopanel) while the upper limit is due to inability to operate the electron beam probe because of phosphor plate flashover (which will be described in a later section).

Both the background gas pressure and the imperfect transparency of the grids served to reduce the beam current. The three grids reduced the beam to ~ 85% of the diode output and at 1.5×10^{-6} torr the gas reduced the beam by another 6% so that ~ 80% of the diode output was left to enter the diagnostic tank (or an induction module).

Although designed to operate at 2 MeV, 1 A the majority of experimental work was done at 1 MeV or 1.2 MeV with a corresponding drop in Child-Langmuir current. As noted before, due to grid and residual gas effects beam current was cut down to ~ 80% of the diode current. Therefore about 250 mA at 1 MeV was expected with a pulse length of ~ 3 μs.

While operating, the beam envelope was found to agree substantially with the calculations done by EGUN (Ref. 2.4). However the location of the beam waist was never precisely determined. It is quite likely that the waist location drifted somewhat during the course of longtime accelerator operation due to changing focal properties as Marx generator voltages drifted.

ELECTRON BEAM PROBE

The electron beam probe is depicted in Fig. 2.3. It consists of a pivoted electron gun whose beam is directed across the diagnostic tank to land on a P22 green phosphor coated plate. A polaroid camera is used to record the traces produced on the phosphor plates.

The electron gun (Fig. 2.4) is a commercially available gun produced for use in black and white television sets and has a price of $5 per gun when purchased in small quantities (1-2 dozen). The electron gun is powered by the "HIF E-beam Diagnostic Probe Gun Power Supply (Fig. 2.5). The wiring diagram (Fig. 2.6) shows normal operating ranges for the gun elements. The electron beam is accelerated from the (negative) cathode potential to ground potential so that no electric field due to the gun is present in the diagnostics tank. The typical accelerating potential for the electron gun was 5 kV. The simple accel-decel-accel focusing arrangement used in the gun is well known (Ref. 2.5) and for this application provided excellent results. The electron beam spot on the phosphor plates was kept under 3 mm diameter, with no focusing adjustments over a wide range of path lengths (~20-100 cm). The gun was pulsed using an HP214 pulse generator providing a 3 μs long +200 V square pulse fed to the electron gun grid through a 150 nf, 20 kV isolating capacitor. Additional electron gun current enhancement was achieved when necessary by using a PARC EGG pulser connnected to the cathode through another capacitor. Both pulsers were slaved to the Cesium Injector master timer to achieve synchronization with the ion beam pulse. When mounted in the diagnostic tank the electron gun, wire leads, and pivot are all shielded by a stainless steel

sleeve (Fig. 2.7) to prevent sparking initiated by ions, electrons, and gas bursts.

The phosphor coated plate was made by rolling stainless steel sheet metal to have a radius of curvature of 12", equal to the inner radius of the diagnostic tank. The plate was then sprayed with a solution of P22 green phosphor, a binding agent, and a solvent. Once the plate was dry a 2.5 cmx2.5 cm grid pattern was overlaid using 1.5 mm draftsmans tape. The plate was set into the diagnostic tank and held in place by a lead brick. By using two such plates, each ~12.8 cm wide, placed end to end, over 180° of the diagnostic tank circumference was covered.

The accelerator typically ran with a repetition rate of 0.2 Hz controlled by a master timer. In order to gather data the polaroid camera used had to be synchronized with the pulse. To do this a circuit was constructed to override the master timer and pulse the accelerator when the camera shutter was opened by tying the camera's bulb switch to an HP power supply. The best data acquisition method was found to consist of letting the master timer pulse the machine two or three times between manual firing. The camera was timed to be as close to the .2 Hz repetition rate as possible, but an operator induced timing error of ~ 0.1 sec enters into the cycle at this point. This in turn affects the beam envelope and energy because of the different recharging times the timing error allows the Marx generators which determine the accelerating voltages. Moreover, slight variations in focusing can have a disproportionately large effect upon the production of secondary electrons. This is because a small change in angle for ions at the outer fringes of the beam can easily change by factors of

about unity the relatively small number of ions colliding with the third drift tube. Thus timing errors directly affect beam neutralization in a major way, thus contributing to pulse to pulse data scatter.

The major operating difficulty of the EBP was phosphor plate flashover. It was found that, except for a a drift tube breakdown due to a crosbar failure, flashover was avoided below a pressure of $\sim 7 \times 10^{-6}$ Torr, as long as a nearby ion gauge was turned off. The next most troublesome problem was the electron gun itself starting a discharge. This discharge was avoided by several steps: 1) leaving the just mentioned ion gauge off; 2) operating the gun below 15 kV; 3) using the stainless steel sleeve described previously; 4) keeping the electron gun and surrounding hardware as clean as possible.

The electron gun was mounted to allow rotation in the transverse plane of the diagnostic tank. As viewed from upstream of the gun, positive rotation was clockwise, with 0° defined as the electon gun pointing straight down. The field of view of the Polaroid camera in azimuthal extent ran from $\sim -7^{\circ}$ to $+58^{\circ}$.

THE DIAGNOSTIC TANK AND AUXILIARY DIAGNOSTICS

Four different diagnostic devices were used in studying the Cs^{+} ion beam:

1) A large Faraday cup (LFC) to measure total beam current.

2) A small movable Faraday cup (SFC, R-Θ probe), in two different configurations, to measure ion beam current profile.

3) The electron beam probe (EBP) for measuring net charge distribution (e^-,Cs^+), as described in the previous section.

4) A bias cylinder used in conjunction with the EBP for measuring the electron energy distribution.

Diagnostic Tank

As shown in Fig. 2.3, the diagnostic tank containing the electron beam probe, Faraday cups and voltage cylinder is located at the end of the drift tube accelerator with a 16" diameter isolation valve in between. The diagnostic tank is two feet in diameter and originally nearly six feet long. An additional three foot section was added after the R-Θ probe was removed to give additional drift distance for the ion beam (see small Faraday cup section). When the EBP was being used the SFC was retracted into a port to prevent interference. The separation between the bias cylinder and the EBP was enough that any deflection of the electron beam due to voltage on the cylinder was negligible.

Large Faraday Cup

During the experiments discussed a large Faraday cup was placed at the downstream end of the diagnostic tank. This cup was used to monitor the total ion current on a pulse to pulse basis, so that data collected with the EBP was done with as nearly identical current pulses as was possible.

This cup was used as an absolute measure of the ion current. A major problem was the generation of plasma and secondary electrons off the collector when hit by the ion beam. Therefore the cup was

constructed as follows (Fig. 2.8): The collector and a biasable grid were placed behind a grounded grid. Also the collector was surrounded on the sides and rear by a grounded cylinder. Separation between collector and grids is 0.5" so that plasma generated by the ion beam impact cannot cause a breakdown interfering with the signal. The cup is normally operated with the collector biased to +250 V and the first grid biased to -500 V. In this manner secondary electrons generated off the collector are retained, preventing spurious current amplification. At the same time free electrons in the diagnostic tank or traveling with the beam are rejected by the negative second grid preventing signal interference. The biasing is done through battery boxes capable of -1 KV to +1 KV range. The collector signal is passed through the battery box and shown on a Tektronix 7834 storage oscilloscope, equipped with a Polaroid camera.

Small Faraday Cup

The small Faraday cup (SFC) is a 1 cm^2 aperture current monitoring device built for scanning across the ion beam (Fig. 2.9). In this manner ion beam current density can be measured directly.

Two different mountings for the SFC have been used. In the original mounting, the SFC was movable in r, θ, and z. This configuration, called the R-θ Probe, gave maximal freedom of movement permitting detailed scans of the entire ion beam. Unfortunately this configuration, even when the R-θ Probe was not being used, interfered physically with the electron beam probe operation. Rails (Fig. 2.10) that supported legs for the R-θ probe to travel along blocked parts of the phosphor coated plates and interferred with nearby electron beam

trajectories. Therefore, during most of the EBP experimental work the R-Θ probe assembly was removed from the diagnostic tank. The SFC was remounted on a rigid coaxial cable extending through a sliding seal, allowing travel across a diameter of the diagnostic tank (from top to bottom) a few cm upstream of the electron gun location. In this configuration the SFC could be drawn into a side port and out of the diagnostic tank proper. This second configuration also permitted the LFC to be located at the downstream end of the diagnostic tank.

The small Faraday cup consists of three components: collector, ring, and outer box. The outer box is grounded and has a 1 cm^2 aperture in the upstream side to allow a beamlet through. The collector is opposite the aperture, on the inside of the box, and several centimeters separate the two. Placed within this space is the ring with its axis concentric with the apeture's center. The collector is biased positively to prevent secondary emission and the ring is biased negatively to prevent any electrons from the outside to hit the collector.

Bias Cylinder

After early measurements wih the EBP had given the unexpected result that significant numbers of electrons were trapped in the ion beam potential it was realized that a method of stripping them out of the beam would be very useful for a number of reasons. First, the presence of electrons is not desired during the acceleration and focusing of the ion beam. Second, the EBP derived total current could be checked against the current measured on the large Faraday cup, providing one test of the inversion technique used for the EBP data. Third,

if the electrons could be stripped out as a function of energy information helpful in the determination of the electron dynamics might be obtained. This last measurement could be done in at least two ways: Collecting the electrons directly as they are stripped out of the ion beam; or using the EBP to determine the electrons stripped out indirectly.

The method of stripping the electrons that was used was biasing a cylinder the beam passed through, upstream of the EBP. Applying positive voltage to the cylinder allowed a measurement of the electrons stripped out because they were collected onto the cylinder. Negative voltage would also strip electrons from the ion beam because the ion beam potential was not great enough to pull all the electrons through the negative potential inside the cylinder, however in this case electrons were ejected from the cylinder so direct electron current measurements could not be made.

Generally, so there are no physical obstructions to the beam, a cylinder like this should have a diameter a few times the beam diameter and no grids at either end to interfere with the beam. Then, to obtain a region inside the cylinder that is nearly equipotential (to ~1%), independent of radius, the cylinder length should be at least five times the diameter. However, in the diagnostic tank space upstream of the EBP was limited. The EGUN calculated envelope showed that the ion beam diameter as ~15 cm. The beam passed through a valve of ~40 cm diameter, therefore, the most practical cylinder diameter was ~30 cm, if, to make use of all available space, the cylinder was placed partially inside the valve. But there was far less than 1.5 m in the upstream end of the diagnostic tank, so a suitably long cylinder could

not be used. Therefore a short (30 cm) cylinder was used with 0.5 mil crosswires at each end supporting a 0.5 mil axial wire running through the cylinder. Transparency with these wires is better than 99.9% reducing the number of secondary electrons to acceptable levels (< 5 mA). Moreover the wires ensure that the potential in the center plane of the cylinder stays within 2 of the applied voltage on the cylinder. The cylinder is connected through high voltage coax both inside and outside the diagnostic tank to a 22 KV, 5.5 mA trickle power supply. The voltage on the cylinder was varied from -20 kV to +20 KV during experiments.

A Pearson probe ferrite core was used to measure the electron current on the cylinder. The probe was placed on the inner conductor of the coax connecting the power supply and the cylinder. Output was viewed on the Tektronix storage scope. The calibration of the Pearson probe was 0.1 V/Amp and had a response time of a few nanoseconds. Signals of a few tens of millivolts were typical, with pulses lasting several microseconds, so that the probe was well within its linear response range during its operation.

Chapter 3 - OPERATION OF THE ELECTRON BEAM PROBE

Introduction

This chapter is concerned with describing the EBP data used in deriving the ion beam radial charge distribution, with the method used to invert the data, and with examining the validity of this method. The azimuthal deflection data is obtained from measurements of the photographs of the electron beam spot deflections. To invert the data a model charge distribution is first assumed; the model parameters are adjusted until the difference (in a least squares sense) between calculated and experimentally measured azimuthal deflections are minimized. The computer code EBEAM is the tool used to calculate deflections for model distributions and will be discussed in detail. The validity of the inversion method is examined by:

1) Testing for the sensitivity of EBEAM to violating the assumption of azimuthally symmetric electric fields in the diagnostic tank.

2) Comparing azimuthal deflections as calculated by EBEAM to deflections calculated analytically for a particular two-dimensional case.

3) Comparing calculated deflections for large electron gun angles done with EBEAM to calculated deflections using a modified EBEAM and a finite length ion beam model to determine the significance, if any, of ignoring finite length effects.

Principles of Electron Beam Probe Operation

As described in Ch. 2, the EBP electron gun directs a beam across the diagnostic tank to produce a spot on the phosphor plates (Fig. 3.1). In the presence of the changing space charge fields due to the drifting ion beam the electron beam path changes as well, so that the spot is moved rapidly (~3 μs) through a curve on the phosphorus plates leaving a trace that is photographed. By changing the electron gun angle between pulses a sequence of such traces, a data set, is collected (Fig. 3.2).

For the 30 cm radius diagnostic tank and small electron gun angles, changing the electron gun angle by 1° displaces the electron beam as it passes near the tank axis 5 mm radially from its previous trajectory, about twice the 2-3 mm beam diameter. Taking the electron beam diameter as the resolution obtainable with the probe then 0.5° increments are the smallest useful changes in electron gun angle. The electron beam can also be pulsed at 10 MHz with the HP pulse generator, allowing ~1 cm axial resolution of the cesium beam.

Measurement of the electron gun angle and the azimuthal deflection is made using a microscope fitted with a micrometer. Electron gun angles range from ~-7° to ~58° with an RMS measurement error of ±0.1°. Azimuthal deflections range in magnitude from 0 cm to < 15 cm and have an RMS error of ± 1 mm. As will be discussed later neither of these errors plays a major role in the uncertainties associated with the derived radial charge distributions.

The EBEAM Code

EBEAM is a two-dimensional code designed to calculate electron trajectories given the electron gun angle, through a model charge distribution to determine azimuthal deflection which it then compares to the experimentally measured deflection. It does this for each measured deflection in a data set and then produces an overall estimate of how nearly deflections the code calculated agree with the experimentally measured deflections. The minimization of discrepancies in a least squares sense between calculation and experiment through modification of parameters leads to a model distribution that is a best fit to the actual distribution. A cutoff on parametric adjustment of the model distribution is naturally imposed when discrepancies between the calculated and the experimental deflection data become equal to the experimental measurement uncertainty of the azimuthal deflections. A useful measure of this discrepancy is the RMS deviation, σ, between model data and experimental data; where:

$$\sigma^2 = \frac{1}{n-1} \sum_{i=1}^{n} \left[A_C(i) - A_E(i) \right]^2$$

and

n = number of data

A_C = EBEAM calculated azimuthal deflection

A_E = experimentally measured deflection

The azimuthal deflections are calculated in a straightforward manner. The program starts with the parametric inputs for the trial charge distribution, the experimentally measured deflections and their

electron gun angles, θ_g, the initial kinetic energy of the electron beam, and the initial position of the electron gun in the diagnostic tank.

The program is now in a position to calculate the electron orbit through the space charge. It does this by calculating the electric field at the electron gun and then, assuming constant acceleration for a small distance, calculates a new position and velocity, and then continues to do this step by step. The (n+1)'st step is related to the n'th step by the equations

$$v\Big((n+1)\Delta t\Big) = v(n\Delta t) + \frac{e}{m} E\Big(r(n\Delta t)\Big)(\Delta t)$$

$$r\Big((n+1)\Delta t\Big) = r(n\Delta t) + v(n\Delta t)\Delta t + \frac{1}{2}\frac{e}{m} E\Big(r(n\Delta t)\Big)(\Delta t)^2$$

EBEAM uses Cartesian coordinates for expressing all vector quantities. The electric field is calculated by determining the charge per unit length, Q, within r and using Gauss' Law for an infinitely long cylindrically symmetric charge:

$$E = \frac{Q}{2\pi\epsilon_0 |\vec{r}|}$$

The charge/length, Q, is calculated in a separate subroutine which contains the parametrically controlled model radial charge distribution.

All this assumes an azimuthally symmetric beam centered in the diagnostic tank. However, if the ion beam is displaced from the

center by a small amount it is a very good approximation to take the electric field as azimuthally symmetric about the displaced ion beam axis. A provision for this is in the EBEAM code and allows for a sensitive method of determining the location of the ion beam axis, within the diagnostic tank.

An estimate of the effect an off axis beam would have on the electric field is readily calculated. The potential, including image charge, for a displaced line charge in a grounded cylinder is:

$$\phi = \frac{Q}{2\pi\epsilon_o} \ln\left[\frac{z-z_1}{z-b^2/z_1^*}\right] - \ln\left[\frac{z-z_1^*}{z-b^2/z_1}\right]$$

where

$$i = \sqrt{-1}$$

$z = x+iy$ in the complex plane,

$z^* =$ complex conjugate,

and $b =$ cylinder radius,

$z_1 =$ displacement of line charge

and $z_{image} =$ placement of image charge $= b^2 z_1 / |z_1|^2$.

The complex electric field produced by this potential can be written simply as

$$E = \frac{Q}{2\pi\epsilon_o(z-z_1)} - \frac{Q}{2\pi\epsilon_o(zb^2 z_1/z_1^2)} .$$

Now from data to be presented in Ch. 4, Table 4.2, beam displacements are known to be generally less than 4 mm. The tank radius is 300 mm. Taking a 3 mm displacement for an example the location of the image charge is at 200 b or 30,000 mm = 30 m. The electric field due to the image charge is roughly 1% of the magnitude of the source electric field. Image charge forces are negligible.

The electron gun because it is at ground potential and extends roughly nine centimeters into the diagnostic tank is another perturbation in the otherwise symmetric radial electric field. The major effect is to make the electric field more intense between the gun mouth and the beam.

An approximation for the effect this perturbation has on the electron beam trajectory was included in EBEAM. Because the field intensifies so that the potential between the beam and the gun mouth is the same as between the beam and the tank wall,

[7]

$$-\int_{\text{beam radius}}^{\text{tank wall}} \vec{E}_u \cdot d\vec{\ell} = -\int_{\text{beam radius}}^{\text{gun mouth}} (\vec{E}_u + \vec{E}_p) \cdot d\ell$$

E_u = unperturbed electric field due the ion beam,

E_p = perturbed electric field induced by electron gun.

The potential of the perturbed part of the field, between gun and beam, can be written as:

$$V_p \equiv -\int_{\text{beam radius}}^{\text{electron gun mouth}} \vec{E}_p \cdot d\vec{\ell} = -\int_{\text{electron gun mouth}}^{\text{tank wall}} \vec{E}_u \cdot d\vec{\ell}$$

The right hand side of this equation is easy to evaluate. The approximation is then to take this potential and add it to the potential of the electron gun itself,

$$V_G' = V_G + V_p ,$$

thus modifying the electron beam initial kinetic energy. Calculation of the trajectory is through the unperturbed electric field but with a perturbed kinetic energy. Typically this correction was less than 10% of the unperturbed kinetic energy, with higher order corrections negligible.

Model Distributions

The EBEAM code uses a model charge distribution $\rho_m(r)$, charge/volume, to calculate Q, the total charge/length, within a radius R:

$$Q = 2\pi \int_0^R r dr \, \rho_m(r) .$$

The model charge distribution $\rho_m(r)$, is a linear combination of functions with parameters to control amplitude and width. These functions are:

1) Gaussian, having amplitude and width as two parameters.

2) Gaussian times radius squared: $Ar^2 \exp\left(-r^2/s_A^2\right)$ again with amplitude and width as parameters.

3) Trapezoid distribution of given amplitude and width, with a linearly falling edge of a given slope, giving three parameters.

4) The Bennett model: $B/\left(1 + r^2/s_B^2\right)^2$ with amplitude and width parameters.

Figure 3.3 compares distributions (1), (3), and (4) for equal rms beam radius and current. Usually two trial functions at a time are used together to build a model distribution. When electrons are present one trial function is positive and one negative, however when electrons are not present two functions are still used to enable modeling of the large radius tail of the ion distribution. Azimuthal deflection vs. electron gun angle for distributions (1),(3),(4) are shown in Figs. 3.4, 3.5, and 3.6 respectively. Note that distribution (3) as shown in Fig. 3.5 has a sharper breaking slope at maximum deflection indicative of the sharp break in the distribution and rapid falloff at the model's edge.

An important feature to note, besides the linearity of the initial deflection at small angles, is the shape of the curves at large angles. Well beyond the unneutralized ion beam rms radius, when the electron beam path is outside all (or nearly all) the charge, the deflections show the same dependence. Many measurements at large angles simply

remeasure the total charge of the ion beam, giving confidence this single most important beam characteristic can be accurately determined.

Simple Harmonic Oscillator

Before discussing the applicability of the two dimensional model to what is essentially a three dimensional problem it seems worthwhile to check if the program is a good representation of two dimensional electron beam deflection. The first check is to assure that the step size, Δt, is small enough that the approximations are very good. The best test of this is to halve the step size to make certain that this has no effect on the results: Halving the step size in EBEAM changes calculated deflections by less than 5 parts in 10^4. A second check is to compare computational results against analytic results, if a solvable case exists. For the electron beam there is one model charge distribution for which the orbit equations can be easily written: a uniform charge of radius R and density ρ.

Consider a uniform charge density, ρ, of radius R. It is straightforward to calculate the orbit of an electron with energy E, and angular momentum ℓ, within this distribution. The electrostatic potential is:

$$\phi(r) = -\frac{\rho}{4\epsilon_0} r^2 \qquad \epsilon_0 = 8.85\times10^{-12}\ \text{F/m}$$

This is a two dimensional harmonic oscillator potential for which the equation of an ellipse is the orbit of a particle within the bounds of this potential.

The velocity of the particle is:

$$v = \sqrt{2m(E-V)}/m \ .$$

with

$$V \equiv e\phi(r)$$

The angular momentum:

$$\ell = mvr \sin \theta_v \qquad \theta_v = \text{angle between } v \text{ and } r \ .$$

Substituting for v and writing V explicitly:

$$\ell = r \sin \theta_v \sqrt{2m\left(E - \frac{e\rho}{4\epsilon_o} r^2\right)}$$

Now r_{max} and r_{min} occur when $\sin \theta_v = 1$. Rewriting:

$$r_{\substack{max \\ min}} = \left[\frac{2\epsilon_o E}{e\rho} \pm \sqrt{\left(\frac{2\epsilon_o E}{e\rho}\right)^2 - \frac{2\epsilon_o \ell^2}{me\rho}}\right]^{1/2}$$

Making use of the well known fact that orbits in a harmonic oscillator potential are ellipses the equation for the orbit can be written:

$$1 = \frac{x^2}{r_{max}^2} + \frac{y^2}{r_{min}^2} \ .$$

The problem being considered is shown in Fig. 3.7. Only the arc PS for which $r < R$ (the particle inside the potential) is of interest. This arc represents the path an electron would take if launched and

collected at a radius R at points P and S respectively. PQ represents the undeflected path, D is the deflection, the length of arc between Q and S. The angle of PQ, α, is given by

$$\tan \alpha = y' = \frac{- r_{min}\, x/r_{max}^2}{\sqrt{1 - \frac{x^2}{r_{max}^2}}} .$$

Point P is the intersection of circle and ellipse. For an eccentric ellipse little error is introduced if the coordinates of P are taken as $(-R,\ r_{min}\sqrt{1-(R^2/r_{max}^2)})$. Two other angles are defined θ_p and θ_g:

$$\theta_p = \sin^{-1}\left(\frac{r_{min}\sqrt{1-R^2/r_{max}^2}}{R}\right) \approx \frac{r_{min}}{R}\sqrt{1 - \frac{R^2}{r_{max}^2}} ,$$

$$\theta_g = \alpha + \theta_p .$$

From the examination of the two isosceles triangles POS and POQ it is apparent the angle, θ_D, subtended by arc QS is:

$$\theta_D = 2\alpha .$$

Thus the deflection, D, is:

$$D = R\theta_D = 2\alpha R .$$

To obtain the final result showing that the deflection, D, is linear in the initial angle, θ_g, for small angles, the small angle approximation for sine and tangent are used. Thus:

$$\alpha = \frac{-r_{min}\, x}{\sqrt{r_{max}^4 - r_{max}^2\, R^2}}$$

Recall

$$r_{min} = \left[\frac{2\epsilon_o E}{e\rho} - \sqrt{\left(\frac{2\epsilon_o E}{e\rho}\right)^2 - \frac{2\epsilon_o \ell^2}{me\rho}} \right]^{1/2} .$$

Now

$$\ell = \sqrt{2mE}\, R \sin\theta_g = \sqrt{2mE}\, R\, \theta_g \qquad \theta_g << 1 .$$

Expanding the inner square root in the expression for r_{min} and cancelling terms

$$r_{min} \cong R\theta_g .$$

This result is hardly surprising, but from the derivation it is seen that this expression for r_{min} is valid for

$$\ell << \sqrt{\frac{2m\epsilon_o}{e\rho}}\, E \qquad \text{or} \qquad \theta_g << \frac{1}{R}\sqrt{\frac{\epsilon_o E}{e\rho}} .$$

For instance, for $R = .3$ m, $E = 5500$ eV, $\rho = 2\text{x}10^{-7}$ C/m^3

$$\theta_g << 1.6 \text{ rad} .$$

This shows the simple expression for r_{min} is good as long as the small angle approximation is appropriate.

Finally, noting that

$$r_{max}^2 \approx \frac{4\epsilon_o E}{e\rho}$$

and taking $x = -R$;

$$\alpha = \frac{R^2\,\theta_g}{\frac{4\epsilon_o E}{e\rho}\left(1 - R^2/(4\epsilon_o E/e\rho)\right)^{1/2}}$$

and

$$D = \frac{R^3\,\theta_g}{\frac{4\epsilon_o E}{e\rho}\left(1 - R^2(4\epsilon_o E/e\rho)^{-1}\right)^{1/2}} = d\theta_g$$

Using the values given for R,E,ρ (.3 m, 5500 V, $2\times10^{-7}C/m^3$); $d = 0.0581$.

The EBEAM code was also used to calculate the azimuthal deflection of an electron within the uniform charge distribution of $\rho = 2 \times 10^{-7}.C/m^2$ and $R = 0.3$ m. Table 3.1 shows how theory and code compare. Theory and simulation agree to ~ 6%, indicating a slight error in the code (although as noted previously the numerical integration is accurate to a few parts in 10,000), but agreement is good enough for confidence in EBEAM in general.

The case for small angles examined has a problem of real interest (to the author at least!) associated with it. Both experimentally and numerically with EBEAM it is seen that small angle deflection is linear in the initial angle (electron gun angle) of the electron's velocity. However, in attempts to work out a simple theory for small angle

deflection for more general (and applicable) distributions of space charge, an easily evaluated approximation for the general coefficient d in the equation,

$$D = d\theta_g \qquad D = \text{deflection}, \quad \theta_g = \text{init. angle}$$

has not been found, but if an analytic expression could be found some real insight into the dynamics of the problem would be gained.

TABLE 3.1

Comparision of Theory and Code Deflection Calculation

Deflection Angle, θ_g (degrees)	Deflection, D (cm)	
	Theory	EBEAM
1°	0.101	0.097
2°	0.203	0.193
3°	0.304	0.290
4°	0.406	0.386
5°	0.507	0.482
6°	0.609	0.577
7°	0.710	0.672
8°	0.812	0.766
9°	0.913	0.859

The Applicability of the Two-Dimensional Simulation to the Three-Dimensional Problem: The Three-Dimensional Simulation

Now that EBEAM has been shown to agree with an analytic theory in two-dimensions, it is worthwhile to examine its range of validity in application to the actual three-dimensional analysis. Is the azimuthal deflection produced by the two-dimensional model equal to the maximum azimuthal deflection produced by a beam of finite length, in particular a beam of 3 m length?

First a model of the electric fields produced by a real beam is needed. This is supplied by making use of the exact solution of the potential of a line charge of finite length in free space (ref. 3.2):

$$V(r,z) = \frac{\lambda}{4\pi\epsilon_0} \ln\left\{\frac{\left[r^2-az+a^2/4\right]^{1/2} + \frac{a}{2} - z}{\left[r^2+az+a^2/4\right]^{1/2} - \frac{a}{2} - z}\right\}$$

where λ is the line charge density and a the line length. The real boundary conditions including ground potential being at $r = R_W$, the diagnostic tank radius, tend to make the actual electric field of the ion beam look more like that of an infinite beam than this model represents. The nearness of the equipotential of the tank wall makes the electric field more nearly radial than it otherwise would be. Therefore the model used is an upper bound on the discrepancies between real world and two dimensional simulation. This model should be applicable for large angles of the electron gun, when the electron beam path remains outside the ion beam radius.

The EBEAM code was modified to calculate both azimuthal and longitudinal deflection. A few lines of code suffice to add calculation of axial position and velocity given an equation for the axial electric field. The code was also modified to simulate the passage of the ion beam past the electron gun. Figure 3.8 shows a trace for large electron gun angle ($> 20^{\circ}$) calculated by the code. Figure 3.9 shows the agreement between the two dimensional and three dimensional calculations of azimuthal deflection at large angles. From the evidence the two dimensonal simulation is a very good model to use in determining the ion beam radial charge distribution.

Chapter 4 - THE EXPERIMENTAL DATA

This chapter presents the Electron Beam Probe data and the model distributions of radial charge which are derived using EBEAM. Supporting data from the Pearson probe and the small and large Faraday cups are presented as well.

The R-θ probe was used to scan the ion beam to obtain current density profiles. The beam was found to be off-center and elliptical at first. However, explanations and corrections for both problems were found. The distorted beam shape was due to an asymmetry of the third drift tube grid; this was easily corrected. The beam was recentered by adjusting the tilt of the third drift tube. Changing the tilt to first order changes the position of the electrostatic lens (DT3 grid) and so changes the beam focal spot. The original misalignment was traced to the hot plate being tilted at a small angle. When EBP experiments began in earnest the R-θ probe was removed because of its interference with the phosphor plates. The small Faraday cup was then remounted on a sliding rod. The large Faraday cup was also placed at the end of the diagnostic tank at that time to allow continued current monitoring.

The experimental data is organized into data sets, each set representing one experimental run. The data sets in turn are organized in groups according to different configurations of the accelerator. These configurations are:

1) A thin, relatively transparent curved grid on DT 3 (the original configuration of the accelerator).

2) A thick less transparent grid on DT3 to attempt an enhancement of secondary electrons produced from this grid over that in (1).

3) The original thin grid back on DT3, and an aperture plate on the end of DT2 to scrape off ions from the outer edges of the beam in an attempte to reduce secondary electron production off the inner surface of DT-3.

4) The original configuration (1) but with the voltage cylinder replaced with a biasable hexcel grid allowing a much higher fractional beam neutralization.

Information for all the data discussed is summarized in Table 4.1 and 4.2 according to individual runs and experimental configurations.

Experimental Errors

Before launching into a discussion of the data and its implications a brief discussion of experimental errors is needed. For any datum provided by the electron beam probe operating with the bias cylinder four quantities need to be measured: the e-gun voltage, the cylinder voltage, the e-gun angle, and the azimuthal deflection. All four are subject to some uncertainty. In general the two voltage measurements are good to about ±50 V generally 1% or less of the operating voltages, and are treated as completely known quantities. The other two measurements are more difficult and less accurate.

Electron gun angle and azimuthal deflection are both measured off the Polaroid pictures taken pulse to pulse. The trace appears on the phosphor plates against a 2.5 cm x 2.5 cm grid. The grid is uncertain

Table 4.1

Ion Beam Line Charge and Percent Neutralization

Data Set	Voltage Cylinder Bias (kV)	Net Line Charge (EBP) (6/m)	Total Line Charge* (LFC) (C/m)	Fract. Neutralization** (1-NLC/TLC)
		Configuration I: Thin Grid No Aperture Plate		
6-1-82	0.0	2.4×10^{-8}	12.8×10^{-8}	0.81
6-2-82	-10.0	10.0×10^{-8}	12.8×10^{-8}	0.22
6-14-82	+12.5	12.2×10^{-8}	11.9×10^{-8}	0.00
		Configuration II: Thick Grid No Aperture Plate		
9-1-82	0.0	3.2×10^{-8}	12.8×10^{-8}	0.75
9-1-82A	+10.0	13.4×10^{-8}	12.8×10^{-8}	0.00
9-2-82	+4.0	9.8×10^{-8}	12.8×10^{-8}	0.23
		Configuration III: Thin Grid with Aperture Plate		
10-22-82α	0.0	3.6×10^{-8}	12.8×10^{-8}	0.72
10-22-82β	+5.0	10.9×10^{-8}	12.8×10^{-8}	0.15
10-22-82γ	+15.0	13.6×10^{-8}	12.8×10^{-8}	0.00
		Configuration IV: Hexcel Grid Replacing Voltage Cylinder		
6-30-82	0.0	3.1×10^{-8}	12.8×10^{-8}	0.76
6-30-82A	-1.0	$< 10^{-9}$	12.8×10^{-8}	1.00
6-30-82B	-5.0	3.8×10^{-8}	12.8×10^{-8}	0.70
6-30-82C	+5.0	7.5×10^{-8}	12.8×10^{-8}	0.41

*12.8×10^{-8} C/m line charge corresponds to 150 mA for 1 MeV Cs^+

**Fractional Neutralization is underestimated by ~10% due to neglect of electrons extending λ_D beyond front and rear of the ion beam.

Table 4.2

Ion Beam Radial Charge Distributions Derived from EBP Data Using EBEAM

Data Set	Beam Misalignment (East-West)(mm)	Radial Charge Distribution, ρ ($\mu C/m^3$, r in cm)	RMS Radius* (cm)	σ (mm)
6-1-82	1.0	$27.0\ \exp(-r^2/2(2.6)^2) - 1.4\ \exp(-r^2/2(11.7)^2)$		3.3
6-2-82	1.5	$16.5\ \exp(-r^2/2(3.1)^2)$		3.1
6-14-82	5.7	$19.0\ \exp(-r^2/2(2.9)^2) + 0.7\ \exp(-r^2/2(7.1)^2)$	4.0	3.0
9-1-82	4.0	$23.0\ \exp(-r^2/2(2.6)^2) - 1.1\ \exp(-r^2/2(9.5)^2)$		3.0
9-1-82A	1.5	$14.5\ \exp(-r^2/2(3.5)^2) + 1.0\ \exp(-r^2/2(5.7)^2)$	3.9	4.7
9-2-82	3.5	$18.3\ \exp(-r^2/2(3.3)^2) - 0.6\ \exp(-r^2/2(9.2)^2)$		3.0
10-22-82α	-2.5	$15.1\ \exp(-r^2/2(3.1)^2) - 0.9\ \exp(-r^2/2(10.2)^2)$		7.1
10-22-82β	3.3	$18.5\ \exp(-r^2/2(2.4)^2) + 0.8\ \exp(-r^2/2(9.4)^2)$		4.3
10-22-82γ	4.0	$19.0\ \exp(-r^2/2(2.7)^2) + 1.1\ \exp(-r^2/2(8.5)^2)$	5.6	8.6
6-30-82	8.0	$2.7\ \exp(-r^2/2(4.2)^2$	4.2	3.8
6-30-82A	9.0	$7.8\ \exp(-r^2/2(3.9)^2) - 2.4(r^2/2(6.9)^2)\ \exp(-r^2/2(6.9)^2)$		
6-30-82B	6.5	$19.5\ \exp(-r^2/2(3.2)^2) - 0.9(r^2/2(7.1)^2)\ \exp(-r^2/2(7.1)^2)$		
6-30-82C	4.0	$17.5\ \exp(-r^2/2(3.0)^2) - 0.9(r^2/2(7.1)^2)\ \exp(-r^2/2(7.1)^2)$		

*RMS radius, $R \equiv \sqrt{(A\sigma_A^4+B\sigma_B^4)/(A\sigma_A^2+B\sigma_B^2)}$, A,B = amp;

σ_A, σ_B = RMS rad. of Gaussian function.

in two regards; first, the point of origin - 0° e-gun angle - is not located to better than two millimeters putting an absolute error of a few tenths of a degree on e-gun angle measurement. Also the grid itself is subject to line to line errors of a millimeter. [Grid errors affect both angle and deflection measurement but can be corrected for by averaging over several grid spacings.] A second level of error is introduced because the pictures are measured with a micrometer under a microscope, but again the measurement error amounts to less than a millimeter if care is taken. Generally total relative errors of one or two millimeters are acceptable when measuring over lengths of 5, 10, 20 cm. If this was all there was to the matter, then, a precise determination of radial density could be expected due to fairly precise measurements.

The greatest uncertainty comes in when a set of data is to be collected. Though e-gun and cylinder voltages remain the same and individual e-gun angle measurements remain accurate to ~0.1°, pulse to pulse variations in the injector produce variations in the beam and so variations in azimuthal deflection. These variations in deflection can be a centimeter in the worst cases. This uncertainty was reduced by averaging over two or three pulses, assuming errors in timing or voltage in the accelerator are distributed about the correct value. After taking a large amount of data (several thousand pulses) the rms variation of data was determined to be 3-4 mm after averaging 2 or 3 pulses for each datum. This number is used to determine whether a model distribution is acceptable. If the RMS deviation (as defined in Ch. 3) $\sigma \approx 3$ mm generally the model reproduces the data as well as can be expected.

Demonstration of the Existence of Negative Charge

The scan from 6-1-82 (Fig. 4.1, Table 4.1) is typical of what was first observed. This data is in conflict with the curves predicted by EBEAM at large electron gun angles (Fig. 3.5) for a uniform charge distribution of radius 4-6 cm. In particular the rapid dropoff of deflection at large angles does not agree with the predicted slow dropoff due to the assumed logarithmic potential encountered by the electron beam when its path lies outside the ion beam radius.

Several effects might cause this disagreement, among them electron beam image charge forces, ion beam image charge forces, or an error in EBEAM. Of these, the last one was addressed in the previous chapter and shown as being less than 6% of total deflection. The image charge forces induced by the electron beam itself are far too small to account for this departure from the simulation, the electron beam charge being roughly six orders of magnitude less than the ion beam charge. At the same time ion beam image charge effects are small because the ion beam is only one millimeter off center as determined by EBEAM. These anomalous effects being negligible, the only explanation of this rapid falloff is negative charge density at larger than expected radii which affects the electron beam path. As the deflections are less the fields encountered must be smaller leading to the conclusion that negative space charge exists at radii beyond the expected cesium ion beam radius. Figures 4.2A and 4.2B show a model fit to the data from 6-1-82 and the model charge distribution. Note the negative charge distribution, which extends to roughly 20 cm, without which the azimuthal deflections EBEAM would calculate would be much too large.

Of course, the real clincher in demonstrating the presence of negative space charge, presumably electrons, is to perform an experiment which shows explicitly some control over it. To do this the Voltage Cylinder, as described, was developed. Data on 6-1-82 was taken with the Voltage Cylinder at ground potential. Figures 4.3A and 4.3B respectively show data taken on 6-2-82 and the best computer fit, and the model charge distribution used to obtain the fit. In this case the Voltage Cylinder was biased negatively about 10,000 volts, sweeping electrons from the ion beam. The large angle deflection follows very closely the code calculations. The model distribution is a simple Gaussian beam profile:

$$\rho(r) = 1.65\times10^{-5} \exp-(r^2/(4.4)^2) \ \mu C/m^3$$

with r in centimeters. This demonstrates that the negative space charge exists and is electrons.

As additional proof of the existence of electrons (removing negative ions would have too much inertia to be swept away by 10 kV), Fig. 4.4 shows the variation of azimuthal deflection with bias cylinder voltage at a fixed electron gun angle (e-gun angle). As the cylinder voltage increases deflection increases as well up to some maximum deflection. This maximum indicates that all electrons have been swept out of the ion beam.

Corroborating this last observation Fig. 4.5 displays the electron current measured by the Pearson probe vs. Voltage Cylinder voltage. It is worthwhile noting that, while the Pearson probe data is only obtained for positive bias, the voltage cylinder works with either

positive or negative bias. Negative voltage prevents electrons passing through the cylinder from upstream, positive voltage traps electrons in the cylinder and collects them on the walls and wires. There is a small negative current (off the cylinder) with negative bias due to a small number of secondary electrons knocked off the cylinder and its equipotential wires. This small current is less than 5% of the ion current.

An inference as to the electron energy distribution can be made from these two measurements. Note that both azimuthal deflection and electron current increase nearly linearly before approaching maximum when they rapidly bend over and become flat. This indicates that the number of electrons biased out of the beam is linear in applied voltage indicating in turn that the electrons are uniformly distributed in energy up to some maximum where the knee occurs.

Model Distributions Used

Chapter 3 covered how a model charge distribution is constructed from different radial functions, each with parameters controlling amplitude (charge density) and width (beam radius). The functions used most extensively were the Gaussian, the modified Gaussian ($A\, r^2 \exp(-r^2/\sigma^2)$), and the trapezoidal (uniform to some radius and then a linear falloff). Also examined was the Bennett model, $(A/(1 + (r/\sigma)^2)^2)$ although it was not used extensively.

When fitting any set of data from an EBP scan only two functions were combined to construct the charge distribution. This was done to keep the number of parameters controlling the model distribution small. To obtain a good fit with only four parameters controlling the model

charge distribution density and radius to fit 30-40 data points would indicate that the model producing a good fit might provide information as to the underlying dynamics shaping the ion beam.

However, the data from the EBP can be fitted equally well using any number of combinations of two functions. For instance Figs. 4.6, 4.7 and 4.8 all show fits to the data scan of 9-1-82 and the model charge distributions used to obtain them. The first model is composed of two Gaussian functions, the second of a Gaussian and a modified Gaussian, the third a trapezoidal function and a modified Gaussian. Their RMS deviations are 3 mm, 3 mm, and 2.5 mm respectively, virtually indistinguishable in light of experimental measurement error and data scatter. Therefore one concludes that at this level of measurement precision no sense of underlying beam processes lay in the data. One does get information about the net charge which, when compared with other EBP data or LFC data, yields an estimate of electron charge as a fraction of ion charge. The RMS radii of the positive core and negative halo are also consistently determined by all three models.

Although there is no discernible difference between the distributions based upon the EBP experimental evidence, all the theoretical analysis will be done using models built from two Gaussian functions. The SFC provides a picture of the ion distribution of the ions alone that seems well fit by a Gaussian with an enhanced tail (Fig. 4.9). And, as will be discussed in Chapter 5, there are strong theoretical reasons to expect the actual electron distribution to more closely resemble a Gaussian than any other simply represented distribution. Using a Gaussian with a negative amplitude will allow for simple estimates of electron temperature and Debye length in an attempt to

construct a self-consistent picture of the partially neutralized ion beam.

The First Experimental Configuration

The final scan complementing those done on 6-1-82 and 6-2-82 is from 6-14-82. In this case the bias cylinder was biased at +12 1/2 KV. Figures 4.10A and 4.10B display data and computer fit, and the derived radial charge distribution respectively. Examination of all these data sets shows that while the radial charge distribution for 6-2-82 (-10 KV on the bias cylinder) shows no explicit negative charge a small amount remained that was revealed only at the higher +12 1/2 KV bias cylinder potential. Table 4.1 gives the net line charge and corresponding current as well as measured beam displacement for all the data sets to be discussed. This table shows 6-2-82 data yields an equivalent current of only 118 mA due to the presence of trapped electrons , well below ~150 mA measured on the LFC, while 6-14-82 data yields 144 mA which is within ~5%.

The Second and Third Experimental Configurations

With the discovery of secondary electrons, determining their source, as well as possible effects neutralization might have upon the ion beam became a primary goal of this research. The second and third accelerator configurations were designed to facilitate the determination of both the electron source and, to a smaller extent, any effects on the ion beam. The two most likely sources of electrons are the third drift tube grid and the DT3 wall. Therefore, the experiments were designed to differentiate as much as possible these two

possibilities. In addition it was hoped that information about electron distribution and energy might provide additional clues.

The second set of experiments were performed with the original DT 3 grid replaced with a "thick" grid made up of 1/4" hexcel in the center with 1/4" wide bands (edge on to the beam) mounted on a template to obtain the desired curvature. Thus if electrons were coming from only the grid, neutralization could go up significantly with the modification. However, as Table 4.1 and Figs. 4.11 (9-1-82A data set) and 4.12 (9-2-82 data set) indicate, there is no apparent increase in neutralization. Comparison of the 9-1-82 data set and its derived charge distribution with 9-1-82A and 9-2-82 data and their derived distributions demonstrate the same behavior (an elimination of negative space charge with higher bias cylinder voltages) as the original three sets of data. Table 4.1 shows that the Voltage Cylinder at +10 kV (9-1-82A) allows a net current of 158 mA to be calculated in good agreement with the large Faraday cup measurement of ~150 mA. In addition to EBP data, a comparison of current drawn onto the Voltage Cylinder for positive bias for times before and after the grid charge (Figs. 4.13, 4.14) shows a slightly smaller average current drawn off after the change. One possibility is that while the grid itself produces more electrons the ion beam envelope is changed so that fewer secondary electrons are produced off the wall of the third drift tube. If electrons were produced in this manner in the original configuration, it may be that a reduction in this production overcompensates for increased secondary production of the grid.

The hypothesis was partially tested by the third set of experiments done. The original grid was replaced on DT 3. Additionally the

aperture of the end of DT 2 was reduced from 24" to 18" diameter by placing a 4" wide ring around the edge. Thus if an unusually large fraction of electron production is from the ions near the beam edge this should reduce beam neutralization substantially.

In this regard it is worth comparing the measurement of electron current on the Voltage Cylinder (Fig. 4.5) after the accelerator was modified to the third experimental configuration, to the previous measurements (4.13, 4.14). A large decrease is immediately apparent. Electron current has dropped to roughly half previous levels. At the same time ion beam current measured on the LFC remains the same as before. The aperture reduction from 24" to 18" is a reduction in area of ~44%. The ion beam envelope is 20" in diameter at the end of the second drift tube corresponding to ~20% reduction. Thus the reduced area of the beam does not completely account for fewer electrons. So between ~20% and ~40% of the neutralizing electrons apparently come from the third drift tube itself.

Let us return for a moment to the question of less electron production from the thicker grid. Although not conclusive, the knowlege that 20%-40% of electrons come from the drift tube wall does mean that the proposed explanation for reduced neutralization is plausible. A different grid might substantially affect the small numbers of large radii ions. The number of secondary electrons would in turn be affected by any change in the flux of ion hitting the DT3 wall. However it is still inconclusive evidence and other unthought of mechanisms may very well play a part.

In an attempt to determine more precisely the origin of the neutralizing electrons, the azimuthal electron beam deflection vs. bias

cylinder voltage was observed. This was done in all three experimental configurations using the two different DT 3 grids and the aperture plate. Selected angles for the electron gun were used to attempt observation of electrons at small radii as well as at large radii. Figures 4.4, 4.15 and 4.16 show typical results at small ($< 20^{\circ}$) medium ($\sim 20^{\circ}$), and large ($> 35^{\circ}$) electron gun angles.

As Fig. 4.4 shows, at small angles the azimuthal deflection measured is independent of voltage applied to the Voltage Cylinder. This is true for all three configurations examined. Therefore this experiment did not distinguish between any possible differences of electron distributions at small radii. The dependence of azimuthal deflection vs. Voltage Cylinder bias at larger electron-gun angles is supporting evidence for the already easily observed electron space charge at larger radii.

Two possible explanations for the absence of azimuthal deflection variation with voltage present themselves. First, that the probe is simply insensitive to the number of electrons present at smaller radii. Second, that no electrons existed at small radii because of some effect of dynamics. This will be discussed in Ch. 5 which includes the theory of electron distribution as the major topic.

Neutralization Experiment

A simple neutralization experiment was carried out on the cesium ion beam (configuration IV, Tables 4.1, 4.2). Replacing the bias cylinder mounted at the gate valve upstream of the diagnostic tank with a biasable hexcel grid (1/4" thick) instead, the ion beam could be flooded with secondary electrons. The data from 6-30-82 show a series

of scans with no bias, -1 kV, -5 kV, and +5 kV bias on the grid (Fig. 4.17-4.20) and the best fit charge distribution. The data from the 0 kV case when compared with data from 6-14-82 and the Faraday cup (Table 4.2) show that the ion beam is ~80% neutralized. In this case the electrons are distributed through the beam with no great evidence of existing as a negative charge density at large radii. However, the data for the -1 kV case shows an ion beam nearly completely neutralized at large radii with a positive core. This could be compatible with a hot electron gas model of the neutralizing secondaries, 1 KeV being the "temperature" of the injected electrons of the hexcel grid. In the 0 kV case the electrons picked up off the grid are cold, having at most ~10 eV kinetic energy. Because the ion beam is "flooded" the space charge potential is much smaller as well, so that in the absence of an applied potential to the grid the electrons stay cold.

The data from 6-30-82B,C (Fig. 4.19 and 4.20) serve to show the hexcel grid approaching operation similar to the Voltage Cylinder. At +5 kV the grid, as the cylinder, simply sucks in electrons while retaining any that might have been knocked off its surface. On the other hand very few 5 KeV electrons would be retained by the cesium beam in the -5 kV bias case.

Time Resolved Electron Beam Probe Data

Figure 4.21 displays a comparison of a time resolved vs. an unresolved EBP trace. The initial rapid deflection, 220 ns-500 ns, agrees well with expectations of a longitudinal electric field exsiting only over a few centimeters near the head of the ion beam. This is due to three factors: 1) The geometry of the ion beam, ~3 m long with

~5 cm radius; 2) the geometry of the diagnostic tank, 3 m long and 30 cm radius; 3) the presence of electrons in, and surrounding, the ion beam. The electrons not only suppress the overall magnitude of the electric field but also smooth out the field by adjusting their distribution.

From 550 to 1650 ns the ion beam is being neutralized slowly. The cause of this is not understood. From 1650 ns to the end of the pulse the neutralization is more rapid. This is due to the head of the ion beam hitting the end of the diagnostic tank. Because the deflection is already seen at 110 ns, meaning the head of the beam has entered the tank, 1650 ns is taken as the time of flight through the diagnostic tank. A 1 MeV Cs^+ beam moves with a velocity of 1-2 m/μs, thus

$$D = vt = 1650 \text{ ns} \times 1.2 \text{ mm/ns} = 1980 \text{ mm}$$

$$D = \text{drift distance}$$

1980 mm is in good agreement with the 2 m length of the diagnostic tank (before the additional 1 m section was added on).

If this neutralization could be eliminated then the EBP could be used to analyze the longitudinal, as well as the radial, charge distribution. The observation of the time dependence of the neutralization does provide another method of measuring the beam time of flight and its location within the diagnostic tank. Modulating the gating pulse as shown in Fig. 4.21 was achieved with the HP214B pulse generator set to produce 30 pulses in a train each ~30 ns wide and 110 ns between pulses.

Summary

The cesium ion beam radial charge distributions have been fit using two Gaussian functions to build the preferred model distribution. These fits have RMS deviations from the data generally on the order of the experimental error, 3 mm. Negative space charge composed of trapped secondary electrons were found to exist, their source being in part the grid of DT 3 and in part the inner wall of DT 3. These electrons appear "hot" in the sense that they are similar to the 1 KeV injected electrons seen in the hexcel beam neutralization experiment. However, other mechanisms, to be discussed in the next chapter (Ch. 5), cannot be ruled out *a priori* as causes of the derived charge distributions general form: A relatively high density positive core with a low density "halo" of negative charge extending beyond. Although details from one set of data to another vary, this general form remains valid and provides excellent agreement with experiment for the case 0 V bias on the Voltage Cylinder.

The ion beam, when stripped of nearly all neutralizing electrons, is well described by a Gaussian radial charge distribution with an enhanced tail at large radii. This agrees well with small Faraday cup measurement of ion distribution. Also, the total current calculated from the derived distributions agrees to within 5% of the large Faraday cup measurement of ~150 mA ion current.

Chapter 5 - THEORY OF THE ELECTRON DISTRIBUTION

The development of a self-consistent picture of the electron halo and the cesium ion beam is the aim of this chapter. The picture that is argued for was presented in Ch. 1. It is recapitulated now: Through a time dependent process the Cs^+ neutralizes roughly 80-90%; of its charge as it passes through the third drift tube grid. The electrons can be viewed as a two dimensional gas with a temperature corresponding to a mean thermal energy approximately half the residual space charge potential, $T_e \sim 240$-480 eV. The Debye length, $\lambda_D^2 = kT_e/4\pi n_e e^2$, can then be calculated to be ~ 10 cm. We apply the theory developed by Lemons and Thode (Ref. 5.1), according to which the Debye length is an adiabatic invariant when the ion beam contracts as it drifts, heating the electrons. Further, when the beam radius becomes less than the Debye length electrons no longer contract. Thus if the ion beam contracts to sufficiently less than the Debye length a high density core of ions develops inside a halo of low density electrons. Qualitatively this agrees with the EBP derived charge distribution. The rest of this chapter addresses beam neutralization, electron equilibrium, and the effect on the ion beam envelope in detail to discover if the theory and the experiment are in agreement.

Cesium Beam Neutralization

In Chapter 4 evidence was presented supporting a uniform energy distribution of electrons. Although no direct measurements were made of the neutralization process the data available do allow inferences as to what occurs. Recall that the ion beam, ~ 26 cm radius, passes

through the curved DT3 grid from the acceleration gap into the drift tube where the accelerating gradient drops off rapidly to zero. Electrons are produced from both the grid and the tube surfaces. These electrons, in the absence of space charge fields, would move into the acceleration gap due to the residual electric field leaking through. However when a potential inside the drift tube due to the space charge becomes sufficiently large, electrons begin streaming into the ion beam as well (Fig. 5.1). Experimentally it is found the beam traps ~ 80-90% of its charge in electrons. Because the full potential of the ion beam is 4800 V (for 150 mA), this indicates that the potential developed to get significant streaming is ~ 480-960 V If the electrons come in uniformly from different grounded surfaces, all starting out with a few tens of electron volts kinetic energy, then when they end up in the beam it might be expected that a uniform energy distribution from tens of eV's up to the residual space charge potential energy of 480-960 V would form. This is because, if the electrons flow in steadily, the first ones pick up extra kinetic energy equal to the space charge potential energy, while later ones pick up less as the potential is reduced. This continues until the beam charge is suppressed sufficiently by the electrons at which point net electron flow effectively stops. As this process occurs, high energy electrons are lost while lower energy ones are trapped but, at the end, electrons with kinetic energies as great as the residual space charge potential energy remain. Because of the symmetry of the beam and the drift tube, there is no mechanism by which the electrons can gain a large azimuthal velocity, hence they form a two dimensional gas.

As the electrons come in they start bouncing around in the potential well (Fig. 5.2). Because the potential is changing as the ion beam continues to drift into the drift tube and because the electron orbits, confined mainly in radial and axial planes, are irregular to begin with, the electrons rapidly isotropize in radial-axial velocity space and become uniformly distributed in configuration space. Even a relatively slow 100 eV electron travels the ion beam length of 3 meters in less than 500 ns and bounces through the beam radially in under 100 ns. Therefore in the 3 μs it takes the ion beam to pass through the grid the electrons have bounced around many times. This is very similar to the process which occurs in a so-called racetrack potential (Ref. 5.2). Consider a particle in a circular two dimensional water bag potential. The symmetry of the potential if the particle is confined within a radius R keeps the particle on a closed orbit (Fig. 5.3a, Ref. 5.3). However if the potential symmetry is broken by turning it into a "stadium" (Fig. 5.3b, Ref. 5.3) all memory of the particle's initial conditions are lost as the orbit starts to wander through the volume.

A characterization of the electrons trapped in the well is possible in one of two related ways. The electron temperature, T_e, and the electron Debye length λ_D can be defined. The electron temperature for 2-D gas is:

$$kT_e = \frac{1}{2} \text{ maximum kinetic energy} = \text{average kinetic energy} .$$

$$= 240\text{-}480 \text{ eV}$$

This is derived defining $kT_e \equiv 1/2\ mv^2$ true for an ideal two dimensional gas and assuming that the electron energy distribution is rectangular. The Debye length is then:

$$\lambda_D^2 = kT_e/4\pi n_e e^2 \ . \tag{1}$$

where n_e is determined by knowing the fraction of electrons in the beam and assuming uniform density at the grid and a radius < 30 cm for the beam.

The Invariance of the Debye Length

It has just been argued that the electron distribution should be nearly uniform below a maximum energy, E_m. The extremely useful results that the Debye length is an invariant, can be obtained by making use of the properties of such a distribution. Consider a two dimensional gas (no azimuthal motion) with such an energy distribution. Assuming uniform spatial distribution the density is given by:

$$n_e = \int_0^\infty d^2\vec{v}\ f_e(\vec{v}) \tag{2}$$

with $f_e(\vec{v}) = \text{const} \times H(v_m - v)$. v_m = maximum velocity, $H(x)$ is the Heaviside function, equal to 0 for $x < 0$ and 1 for $x > 0$. Because motion is in the plane d^2v can be taken as $dv_z\ dv_x$ without loss of generality. With $\theta = \tan^{-1} v_x/v_z$ and $d^2v = v\ dv\ d\theta$, the integral for n becomes:

$$n_e \propto \int_0^\infty dv\ v\ H(v_m - v) \propto v_m^2 \tag{3}$$

Now, using the same method, the pressure is found by taking the second moment of n_e:

$$P_e \propto \int_0^\infty dv\ v\ v^2 H(v_m - v) \propto v_m^4 \tag{4}$$

Thus the general result follows:

$$\frac{P_e}{n_e^2} = \text{constant} \tag{5}$$

This constant can be related to the Debye length in a manner consistent with Eq. (1):

$$\frac{P_e}{n_e^2} = 4\pi e^2 \lambda_D^2 \tag{6}$$

Hence the Debye length is seen to be an invariant for a two-dimensional gas with a rectangular energy distribution. This result will be used extensively in the remaining discussion, much of which closely follows the development of Lemons and Thode. It must be pointed out, however, that this result is certainly not strictly applicable to the Cesium ion beam being studied. This is primarily because,

although the electrons are essentially confined to two-dimensional motion, the geometry is radial which modifies the equations, e.g.:

$$2\pi\, r\, n_e = \int_0^\infty d^2\, v\, f_e(v) \qquad (2')$$

Nevertheless the utility of having an invariant is so great that the Debye length will be taken as such. Two considerations which ameliorate this inconsistency are that:

1) The electrons spend most of the time at larger radii where the geometry approaches a Cartesian geometry for which λ_D is invariant.

2) At small radii the angular momentum, ignored in this analysis, plays a significant role in reducing the density from what it would be if all the electrons actually had exactly zero angular momentum.

Thus one might expect the electron distribution to be insensitive to geometry (particularly where the electron distribution has been measured with the EBP) and λ_D still approximately constant.

Basic Equations for Electron Equilibria

A convenient model to use to find the electron equilibrium is presented by Lemons and Thode (Ref. 5.1) in discussing the focusing of intense ion beams. Because it has a certain amount of relevance to the

present problem and because it is simple enough to solve analytically the problem they discuss is presented here.

Consider a uniform hard edge ion beam. Electrons that are comoving neutralize the beam but have a "temperature" T. The radial electron distribution can then be solved for self-consistently. The solution requires the definition of electron temperature given in the previous section assuming the uniform electron energy distribution, rather than a Boltzmann distribution

Assuming azimuthal symmetry, only $n_i(r)$ the radial ion, and $n_e(r)$ the radial electron density profiles, and $E_r(r)$ the radial electric field play a part in the non-relativistic treatment. The electrostatic field is determined by Poisson's equation (in Gaussian units):

$$\frac{1}{r}\frac{d}{dr}(r\,E_r) = 4\pi e(n_i - n_e) \tag{7}$$

The ions are uniform to the beam edge $r = a$ then vanish so that

$$n_i(r) = n_{io}\,H(a-r)\ . \tag{8}$$

The electron distribution is determined by radial force balance.

$$\frac{dP_e}{dr} = -\,n_e\,eE_r \tag{9}$$

Pressure and density are related using Eq. (6) restated here:

$$P_e/n_e^2 = \text{constant} = 4\pi e^2 \lambda_D^2 \tag{10}$$

It is important to note that Eqs. (9) and (10) are consistent with each other. Although Eq. (10) was derived under the assumption of a uniform distribution, both P_e and n_e are local variables related to each other through a global invariant the Debye length. Therefore, once the Debye length for the electrons has been established at the grid, where the beam is assumed to be uniformly partially neutralized by an electron distribution uniform in velocity space as well, from then on the Debye length (as is the emittance) is a global invariant independent of the beam evolution. A different viewpoint is that Eq. (10) becomes the definition of the Debye length while Eq. (9) provides the additional relation needed to determine $P_e(r)$, and $n_e(r)$. For overall charge neutrality to hold of one additional constraint is applied:

$$\int_0^\infty dr\, r(n_i - n_e) = 0 \tag{11}$$

Equations (7-11) can be solved for n_e, P_e, and E_r in terms of modified Bessel functions of the first and second kinds, I_n and K_n. In particular the solution for n_e is given by:

$$n_e(r) = n_{io}\left[1 - \frac{a}{\sqrt{2}\,\lambda_D} K_1\left(\frac{a}{\sqrt{2}\,\lambda_D}\right) I_o\left(\frac{r}{\sqrt{2}\,\lambda_D}\right)\right],$$

$$\text{for} \quad r \leqslant a \ ; \tag{12}$$

$$n_e(r) = \frac{n_{io}\,a}{\sqrt{2}\,\lambda_D} I_1\left(\frac{a}{\sqrt{2}\,\lambda_D}\right) K_o\left(\frac{r}{\sqrt{2}\,\lambda_D}\right),$$

$$\text{for} \quad r > a \ ;$$

Defining $R \equiv a/\sqrt{2}$ the rms ion beam radius it is apparent that R/λ_D describes local beam neutralization; when $R/\lambda_D \gg 1$ local neutralization is good, when $R/\lambda_D \lesssim 1$ it is poor. Figures 5.4A and 5.4B (Ref. 5.1) illustrate this result.

The average temperature of the electrons can be evaluated in terms of the constant $P_e/n_e{}^2 = 4\pi e^2 \lambda_D{}^2$ and modified Bessel functions:

$$T_e = 4\pi e^2 \lambda_D{}^2 \int_0^\infty dr\ r\ n_e{}^2 \Big/ \int_0^\infty dr\ r\ n_e$$

$$= 8\pi e^2 n_{io} R\ K_1(R/\lambda_D)\ I_2(R/\lambda_D)$$

In the event that ion beam focusing is gradual the electrons are heated and the equation for the temperature can be evaluated to find out by how much.

Applicability to the Cesium Ion Beam

The Cs^+ beam has a profile assumed uniform at the DT3 grid which evolves to approximately Gaussian (modified by a non-Gaussian tail) as determined by the SFC scan in the diagnostic tank. The details of the model therefore are not directly applicable. Yet the model, especially the idea of Debye length invariance, enables a self-consistent analysis of the available data. Of greatest interest is determining, if possible, electron evolution to the observed distribution, including a determination of the electron distribution in the core of the ion beam.

Assume for a moment that the electrons are produced uniformly from the third drift tube grid, and that the beam is therefore fairly uniformly neutralized by electrons with a Debye length roughly equal to the beam radius. Assume the electron distribution will not contract with the ion beam. Therefore the electron temperature goes up instead, while only details of the electron distribution change. Meanwhile the ion beam contracts to somewhat more than one eighth its original radius, the ion density rising by about sixty-four times. Thus if the electron density was originally equal to the ion density, after contraction the electron density is ~ 1.6% ion density. This agrees qualitatively quite well with the observed cesium and electron distributions. A comparison of maximum negative charge density (ρ (r=0)) with the core density (unbiased bias cylinder) give percentages of: ~ 3.5% (6-1-82), ~ 2.7% (9-1-82), ~ 3.3% (10-22-82α) in fair agreement with the figure of 1.6% estimated above.

We note that the empirically derived electron densities are roughly a factor of two greater than the estimate which assumed the

electrons do not contract at all. Thus, empirically, the evidence is that the electrons contracted to about half the original volume. Because the beam length is invariant this implies radial contraction by a factor of $\sqrt{2}$ assuming the electrons stay uniform in distribution. For a hard edge model this means electrons contract from 30 cm radius to 21 cm in, surprisingly good agreement with the empirical charge distributions given in Ch. 4. However the gate valve is also 20 cm radius so it could be that electrons at larger radii are scraped off.

Another way to check to see if the model of Lemons and Thode agrees quantitatively with the data is by calculating the Debye length of the electrons and comparing with an empirical estimate of λ_D derived from the EBEAM determined radial charge distribution. At the grid where the electron and ion distributions are assumed nearly uniform the electron density and temperature can be estimated given the electron charge, which is about 80%-90% of the ion charge, thus allowing λ_D to be calculated. Table 5.1 gives initial electron charge density, temperature, and Debye length calculated using data from Table 4.1. It also shows the estimated Debye lengths from the empirical distributions obtained by simply equating Debye length to the width of the negative Gaussian function. Again agreement is quite striking.

The calculated and empirical Debye lengths compare very well (see Table 5.1). In fact for configurations II and III agreement is better than 8%, really excellent considering the crudeness of equating the electron distribution to the negative Gaussian function. These results are strong justification for accepting the theory presented as essentially correct, in particular the invariance of the Debye length, and

the two-dimensionality of the electron gas upon which the T_e estimates rest as well.

Table 5.1

Electron Gas Parameters

Electron Density N_{eo}*	Electron Temperature T_{eo}**	Debye Length (calculated)	Debye Length (empirical)
	CONFIGURATION I		
2.5×10^6 cm^{-3}	323 eV	8.4 cm	9.9 cm
	CONFIGURATION II		
2.5×10^6 cm^{-3}	354 eV	8.8 cm	9.5 cm
	CONFIGURATION III		
2.4×10^6 cm^{-3}	435 eV	10.0 cm	10.2 cm

*N_{eo} is estimated from fract. neut. data (Table 4.1)

**T_{eo} = 1/2 (remanant beam potential)

Still the possibility that the electron distribution is quite different, indeed that it might be hollow cannot be completely ignored. The next section takes up the question of finding a hollow beam equilibrium.

The Unlikelihood of a Hollow Electron Distribution

It is possible to examine the question of whether the electron halo is hollow or not by making use of the formalism developed by

Lemons and Thode, and expanding a bit upon it. Consider an ion beam of uniform density n_{io} and radius a. Instead of an electron gas equal in charge to the ion space charge, consider a rotating gas, rotation frequency, ω, a fraction of the ion charge. The equations used by Lemons and Thode are modified by altering Eqs. (3) and (5):

$$\frac{dP_e}{dr} = - n_e eE_r + n_e m\omega^2 r \tag{3'}$$

$$\int_0^R dr\, r(n_i - n_e) = (1-f)\frac{n_{io} a^2}{2} \qquad 0 \leqslant f \leqslant 1 \tag{5'}$$

where $n_e m\omega^2 r$ is the centrifugal force term due to uniform rotation, R is the diagnostic tank radius and f is the fractional neutralization of the ion beam. Again n_e, E_r, and P_e can be solved for in terms of the modified Bessel functions I_n, K_n. The radial electron density has the form:

$$n_e(r) = A_L\, I_o(\chi r) + n_{io} - m\omega^2/2\pi e^2$$

$$\text{for} \quad r \leqslant a \tag{12'}$$

$$n_e(r) = A_G\, I_o(\chi r) + B_G\, K_o(\chi r) - m\omega^2/2\pi e^2$$

$$\text{for} \quad r > a$$

With $$B_G = n_{io}\chi\, a\, I_1(\chi a)$$

$$A_G = \frac{B_G((2a/\chi))K_1(\chi a) - (R/\chi)K_1(\chi R)) + (m\omega^2R^2/4\pi e^2) - (1-f)n_{io}a^2/2}{(R(\chi)I_1(\chi R)}$$

$$A_L = A_G - B_G\, K_1(\chi a)/I_1(\chi a)$$

$$\chi \equiv \frac{1}{\sqrt{2}\,\lambda_D}$$

From examining the expression for n_e above it is clear that the rotational term has a large effect when $\omega^2 \sim \omega_p^2/2 = 2\pi\, n_{io}\, e^2/m$. For 150 mA Cs with ~ 40 cm radius $\omega_p/\sqrt{2} \sim 1.7\times10^8$ rad/sec. Figures 5.5 and 5.6 show $n_e(r)$ for the fractional neutralization $f = 0.9$; the former shows the distribution for $\omega << 2\pi n_{io}e^2/m_e$ the latter for $\omega \approx 2\pi n_{io}e^2/m_e$. The first case corresponds to an average energy of rotation of ~ 10 eV, the second to ~ 5 KeV rotational energy. Clearly a hollow radial distribution given any electron energy spectrum requires rotational energy far greater than any conceivable mechanism might provide. Therefore the conclusion that the electron distribution closely resembles the one given by Eq. (12) rather than (12') (with due modification for different ion distributions) is the one which best fits both experimental and theoretical evidence.

Effect of Partial Neutralization Upon the Ion Beam Envelope

Lemons and Thode derive an envelope equation for the RMS ion beam radius. They assume both a paraxial beam and one which evolves self

similarly with the RMS radius. They assume electron and ion total charges are equal. The equation obtained is:

$$\left(\frac{d\,R}{d\,\tilde{Z}}\right)^2 + \frac{2\,K}{\tilde{R}}\left[K_o(\tilde{R})\;I_1(\tilde{R}) + K_1(\tilde{R})\;I_o(\tilde{R})\right] + \frac{\epsilon_i}{\lambda_D^{\,2}\;V_z^{\,2}\;R^2} = \text{constant} \quad (13)$$

where $\tilde{R} = R/\lambda_D$,

$\tilde{Z} = Z/\lambda_D$,

$K = 2N_L\;Z_i^{\,2}\;e^2/M_i\;V_z^{\,2}$ is the ion beam perveance, as defined in Ref. 5.1.

Z_i = ion charge state and N_L is the line density of the beam.

The second term on the left hand side of the equation contains the effects of the partially neutralizing electrons. In the limit of an unneutralized beam $\lambda_D >> R$ they verify that the expression reduces to the well known result for that case. The case at hand corresponds to a small range of R, with $\lambda_D \simeq R$ always true. Fortunately the ion beam emittance is small enough ($\pi\epsilon_n = 2\text{x}10^{-6}\pi$ m-rad.) (Ref. 1.10) that use can be made of the curves calculated for the zero emittance case giving the final beam RMS radius (Fig. 5.7, Ref. 5.1). The curves are labeled by beam perveance and initial focusing angle which for the cesium ion beam is $\tan^2 \psi/K \cong 2$. The experimentally verified EGUN code (ref. 2.4) provides information on the envelope of the unneutralized ion beam, in particular that the RMS ion beam radii at the third drift tube grid, the beam waist and the EBP location are

18.2, 4.0, and 7.1 centimeters respectively. Making use of Fig. 5.7 and using $\lambda_D = 10$ cm the RMS ion beam waist in the presence of electrons is found to be ~1.3 cm. Thus the difference in the final radius for the two cases is a factor of three. No direct measurements of the ion beam waist were made, however the RMS radius of the beam at the EBP position as measured on 6-14-82, 9-1-82, and 10-22-82 are 4.0, 3.9, and 5.6 cm respectively (Table 4.2). The first two are about 1.8 times smaller than the 7.1 cm derived from EGUN, the last is ~1.3 times smaller. Given that there are not as many electrons as ions in the system in contrast to the assumptions made by Lemons and Thode, the smaller measured radii clearly indicate the effect of the trapped electrons upon the ion beam. This supports the theory although the comparison of beam radii is crude due to the inability to measure the ion beam waist.

Conclusion and Summary

The value of the EBP and the success of the computer code EBEAM in deriving empirical charge distributions is established. Even with the different distribution functions used the data inversion consistently gave empirical charge distributions with the same RMS ion beam radius, the same total current, and in very good agreement with the LFC. The EBP performed consistently and proved itself as a useful non-destructive diagnostic of beam space charge. Time resolution (~100 ns) of the data has been demonstrated and can provide information on the longitudinal space charge distribution, as well as information on beam neutralization.

This last chapter has attempted to present a theory which gives a self-consistent explanation of the data presented in Ch. 4. In particular the points addressed were:

1) The formation of an electron halo with an RMS radius of ~10 cm measured at the position of the EBP, and if the distribution is hollow.

2) The origin of the electrons in the halo.

3) The ion distribution with an RMS radius of ~4 cm as measured at the position of the EBP instead of an RMS radius of ~7 cm predicted by the EGUN code.

4) That the electronic charge, the ion beam trapped is ~80%-90% of the total ionic charge.

Using a model proposed by Lemons and Thode, particularly the idea of an invariant Debye length, it was shown that:

1) The electron distribution RMS radius was the electron Debye length as calculated from knowledge of electronic charge and assumptions as to mean electon energy and energy distribution and;

2) The ion beam RMS radius of ~4 cm is consistent with the calculation done by Lemons and Thode for a beam with the same characteristics except that they assume 100% charge neutralization in the model.

3) The calculated density of electron is at $r = 0$ for a Debye length of ~10 cm, 3.5% of ion density, agrees very well with the empirical results of 3.5% (6-1-82), 2.7% (9-1-82), and 3.3% (10-22-82α).

Therefore theory and experiment are in substantial agreement in the regime of the Cs beam studied, of one ampere and one megavolt, although the theory was originally addressed to kiloampere and mega-ampere ion beams with kinetic energies of ~10 MeV to 10 GeV.

REFERENCES

1.1 Goldan, P., Leavens, W. Phys. Fluids 13 (2), p. 433-39 (1970).

1.2 Swanson, D. A., Cherrington, B. E., Verdeyen, J. T. Phys. Fluids 16 (11), p. 1939-45 (1973).

1.3 Daooter, B. V., Kovrov, P. E., Morozkov, A. N., Pruskuw, M. A., Temckun, S. M. Diagnostics Plasmy 3 p. 295-302 (1973).

1.4 Dean, S. O. ed 1981. Prospects for Fusion Power, p. 3 Elmsford, N.Y.: Pergamon. 90 pp.

1.5 Emmett, J. L., Nuckolls, J., Wood, L. 1974. Sci. Am. 230 (6), p. 24-37.

1.6 Brueckner, K. A., Jorna, S. 1974. Rev. Mod. Phys. 46, p. 325-67.

1.7 Keefe, D. 1982. Ann. Rev. Nucl. Part. Sci. 32, p. 391-441.

1.8 Coleman, L. Krupke, W. Strack, J. eds. 1980. Laser Program Ann. Report vol. 2, p. 3-18, Lawrence Livermore Natl. Lab. Rep. UCRL-50021-80.

1.9 Maschke, A. W., Brookhaven Natl. Lab. Rep. BNL 19008. 6.pp. Maschke, A. W. 1975. IEEE Trans. Nucl. Sci. NS22, p. 1825-27. Martin, R. L., Arnold, R. C. 1976. Argonne Natl. Lab. Intern. Rep. RLM/RCA-I and U.S. Patent 4,069,457.

1.10 HIF Staff 1981. Law. Berk. Lab. Rep. LBL-12594. 38 pp.

1.11 HIF Staff 1983. Law. Berk. Lab. Rep. LBL-15926. 20 pp.

1.12 Keefe, D., Rosenblum, S. S. (1982). Gesellschaft fur Schwerionenforschung, Darmstadt, report: GSI-82-8, pp. 161-180.

2.1 Taylor, J. B., Langmuir, I. Phys. Rev. 44, p. 423 (1933).

2.2 Lampel, M., Tiefenback, M. Appl. Phys. Lett. 43, p. 57 (1983).

2.3 Keefe, D. 1977. Law. Berk. Lab. Rep. LBL-6796. 28 pp.

2.4 HIF Staff, 1981. Law. Berk. Lab. Rep. LBL-12594. 38 pp.

2.5 El-Kareh, A.B., El-Kareh, J.C.J. Chapter 6, p. 185-245, Electron Beams, Lenses and Optics, 1970. ACADEMIC PRESS, New York, London, p. 411.

3.1 Griem, H. 1964 Plasma Spectroscopy. McGraw-Hill.

3.2 Lorrain P., and Corson, D. (1970). Electromagnetic Fields and Waves 2'nd ed. Freeman, p. 687.

5.1 Lemons, D., Thode, L. Nucl. Fus. 21, p. 529 (1981).

5.2 See for instance, Arnold, V. and Avez, A. Ergodic Problems of Classical Mechanics, (1968). Benjamin. Ch. 3, pp. 53–56.

5.3 Littlejohn, R. (1983). Personal communication.

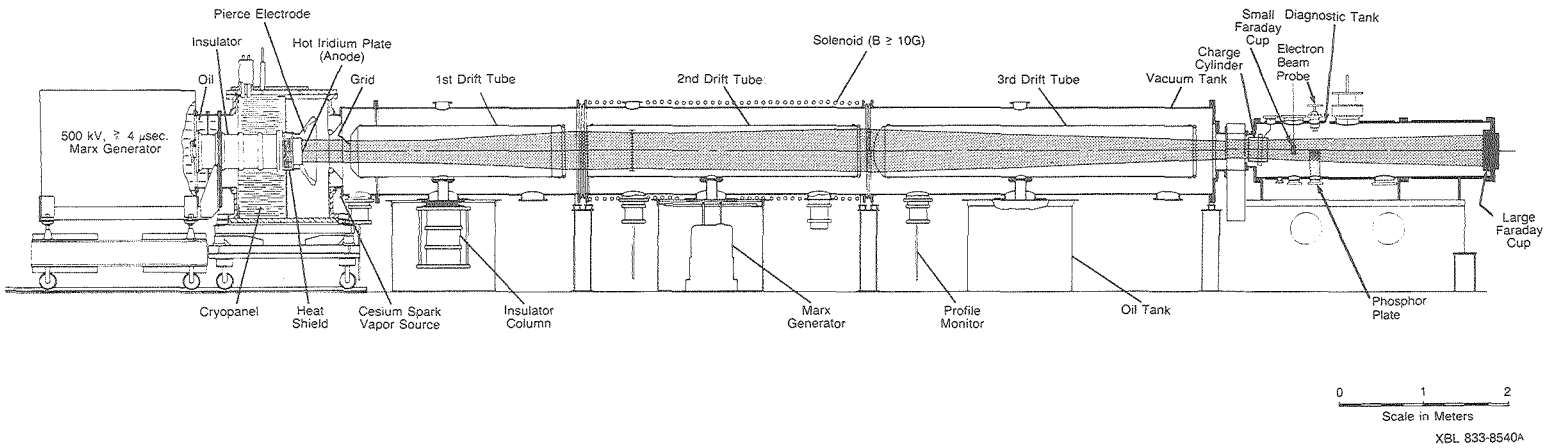

Figure 1.1 One Ampere Cesium Ion Source with EBP and SFC in the Diagnostic Tank

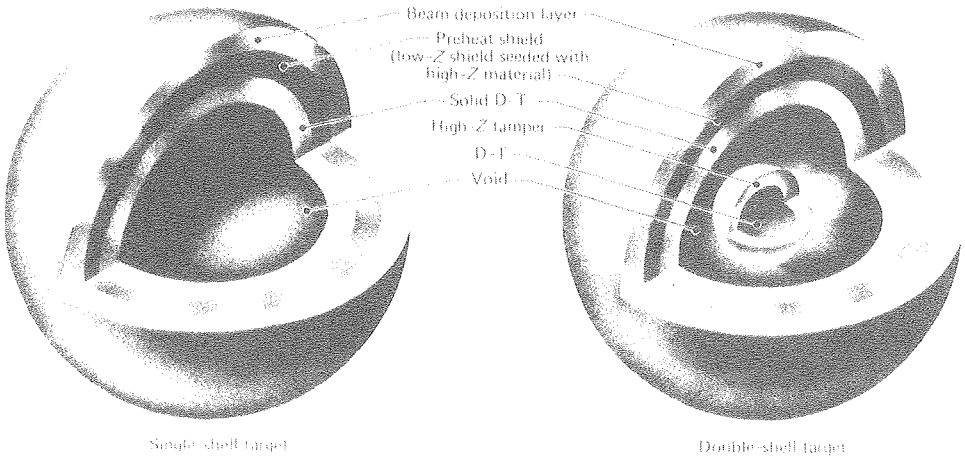

XBB 822-1494

Figure 1.2 D-T Targets: Crosssectional View

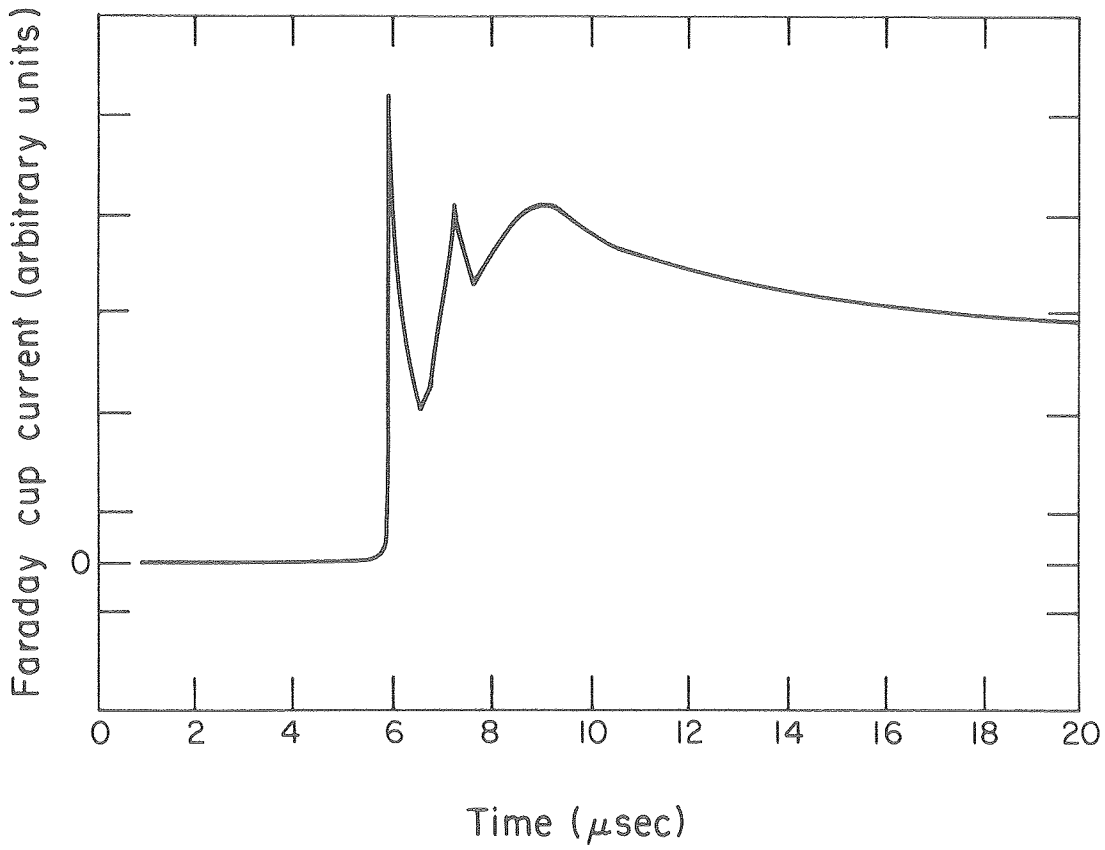

XBL 831 - 40

Figure 2.1 Transients in Cesium Current Pulse

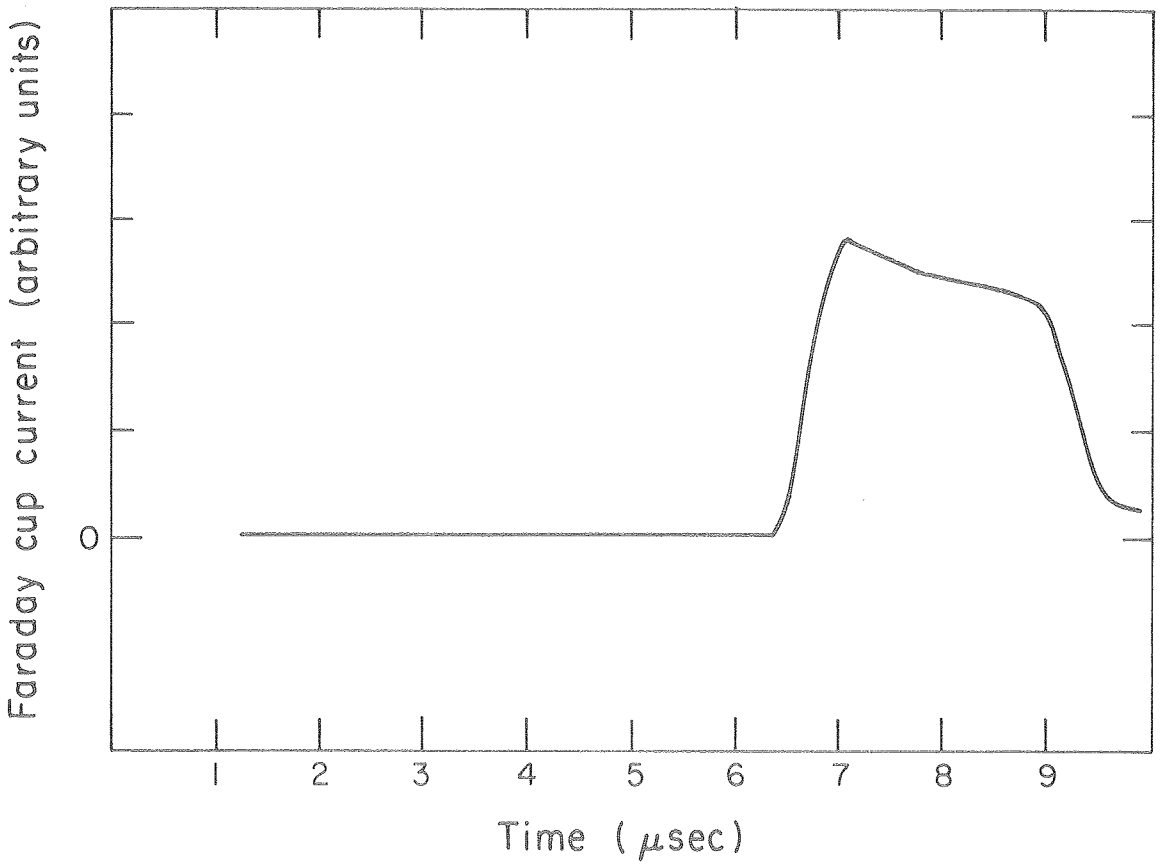

XBL 831 - 39

Figure 2.2 Cesium Current Pulse with Transients Eliminated

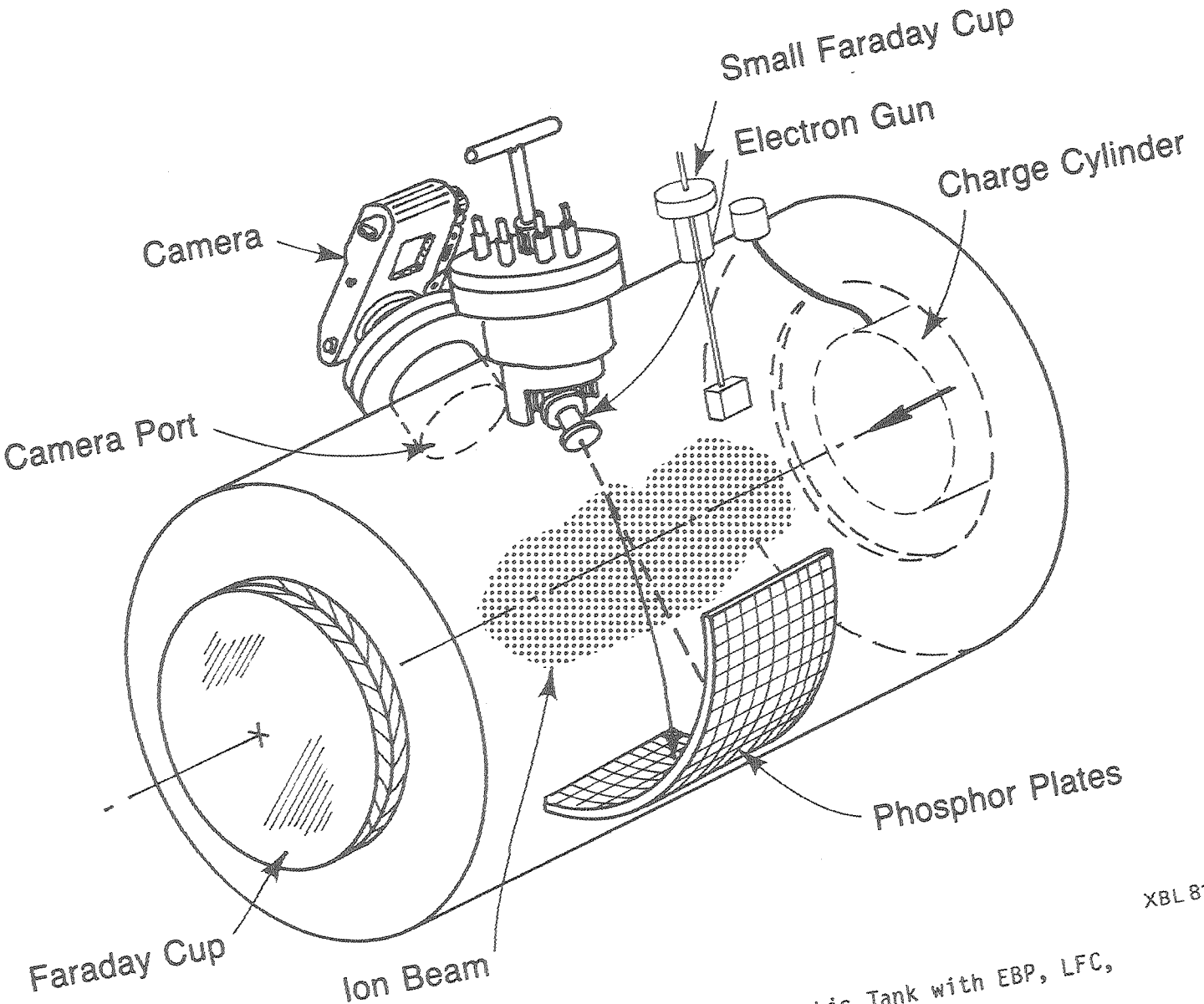

Figure 2.3 Three-Quarter View of the Diagnostic Tank with EBP, LFC, SFC, and Voltage Cylinder

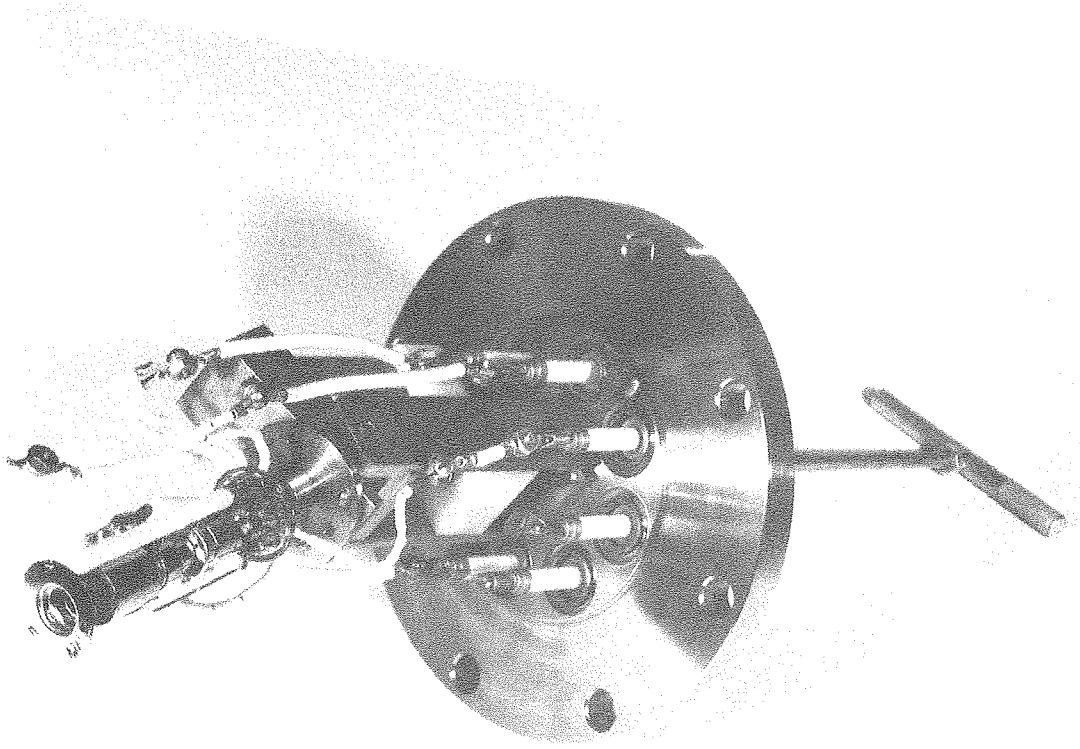

Figure 2.4 EBP Electron Gun

CBB 810-9691

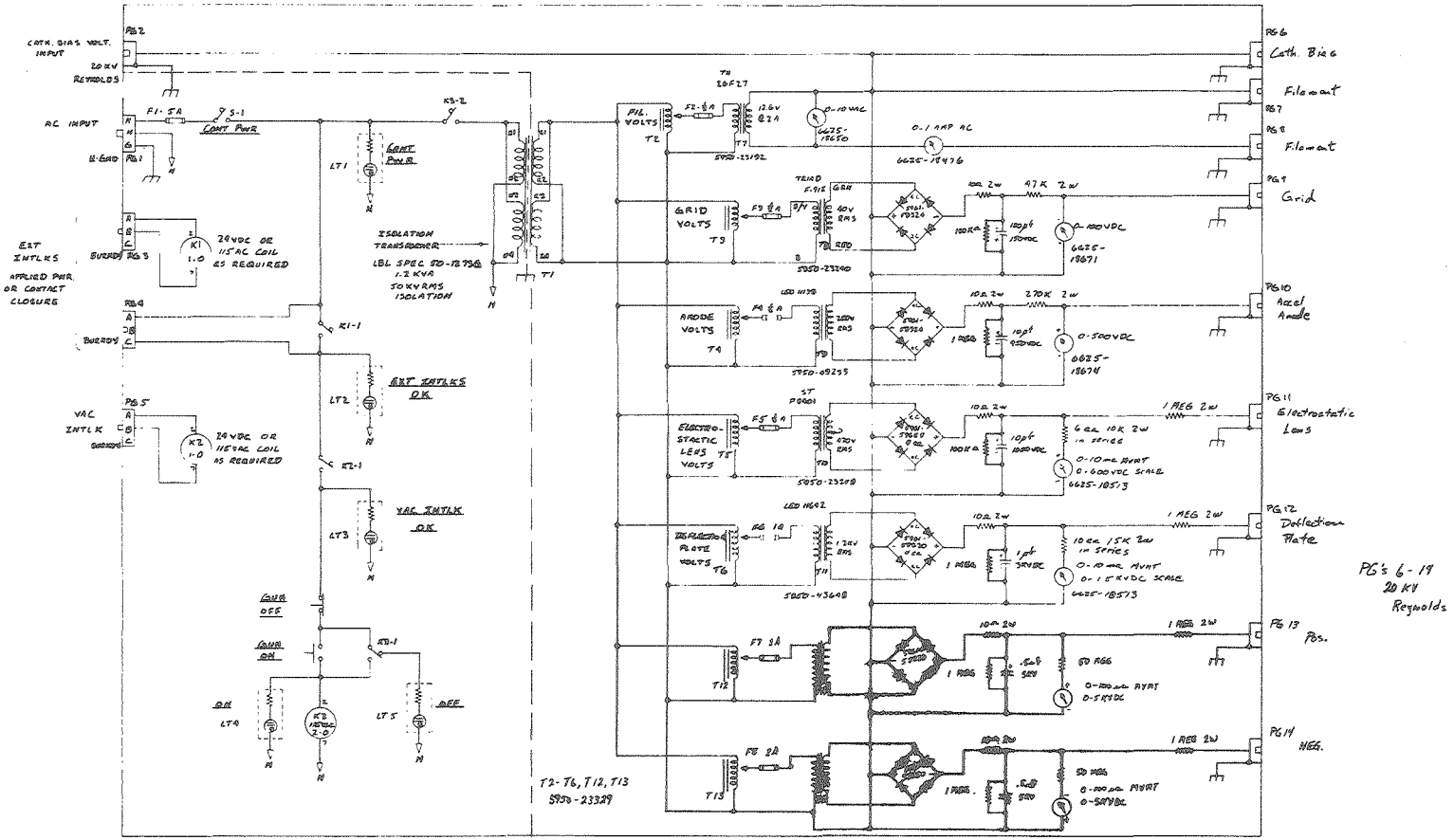

Figure 2.5 HIF EBP Electron Gun Power Supply Schematic

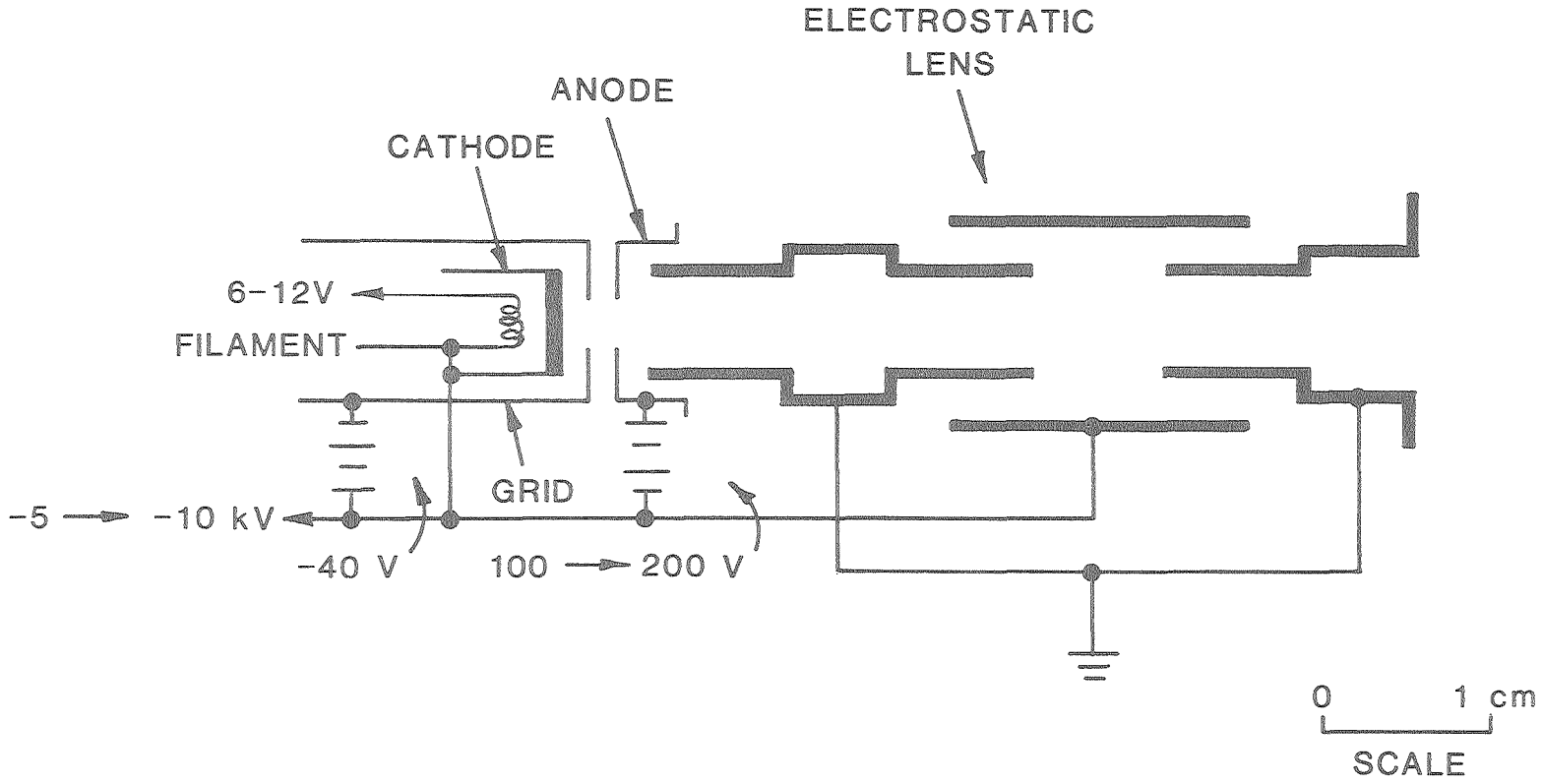

Figure 2.6 Electron Gun Wiring Schematic

XBL 828-10888

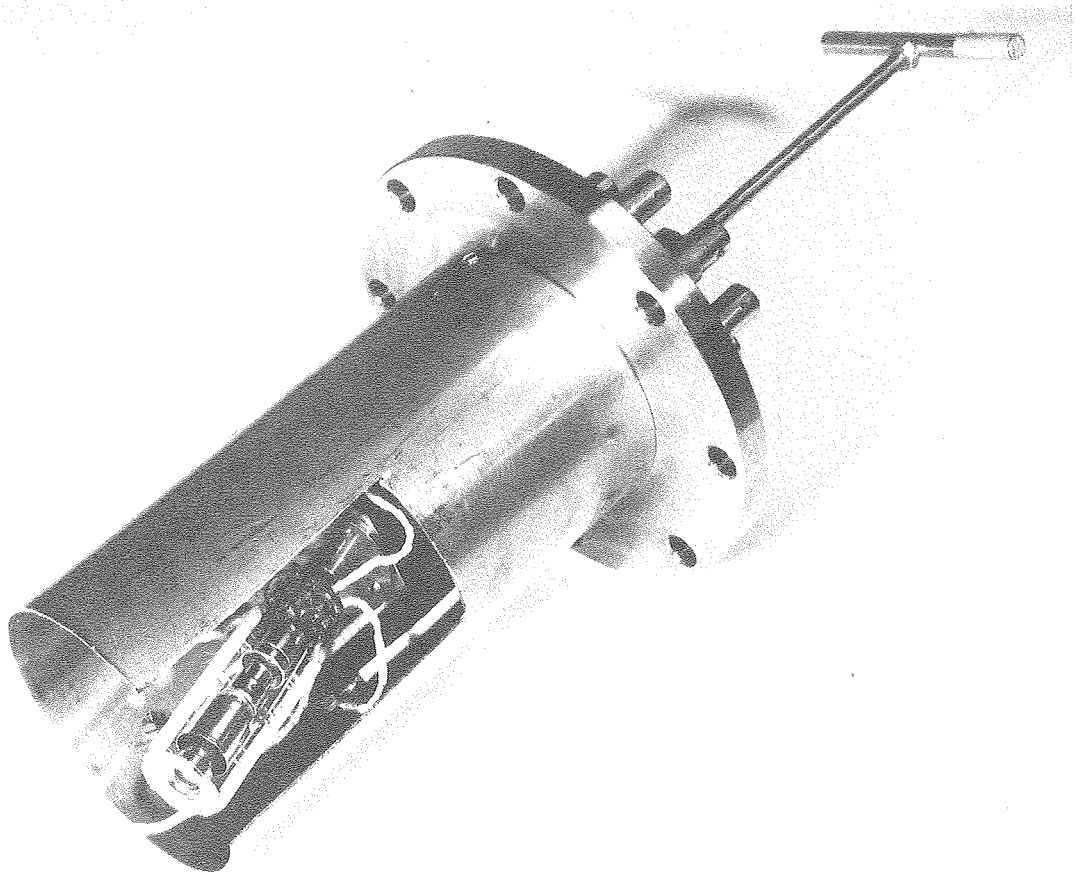

CBB 810-9693

Figure 2.7 EBP Electron Gun with Sleeve

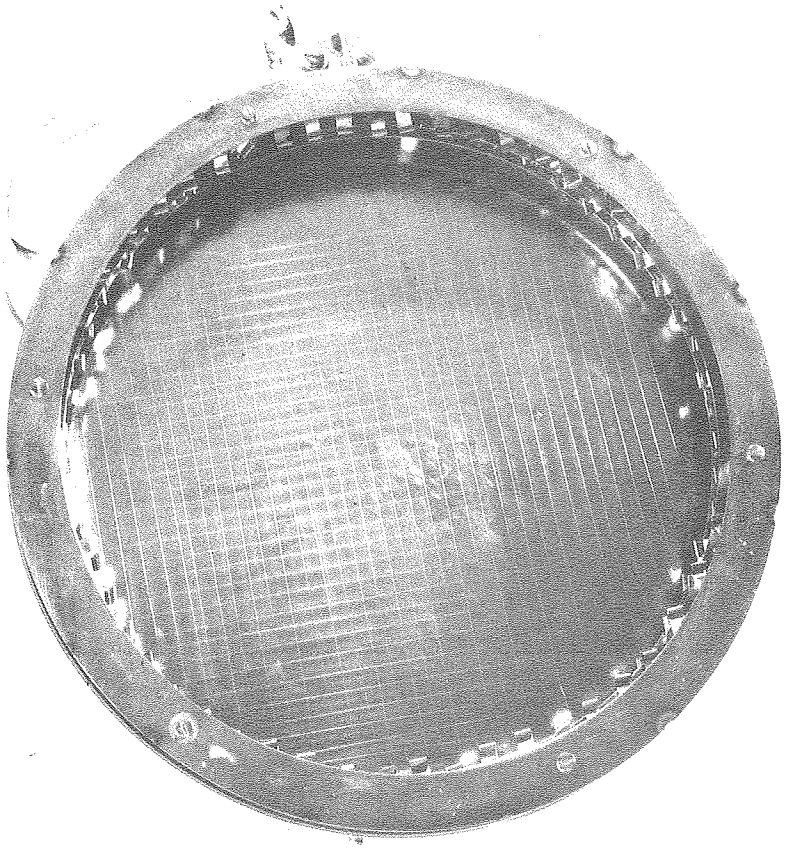

CBB 800-12565

Figure 2.8 The Large Faraday Cup (LFC)

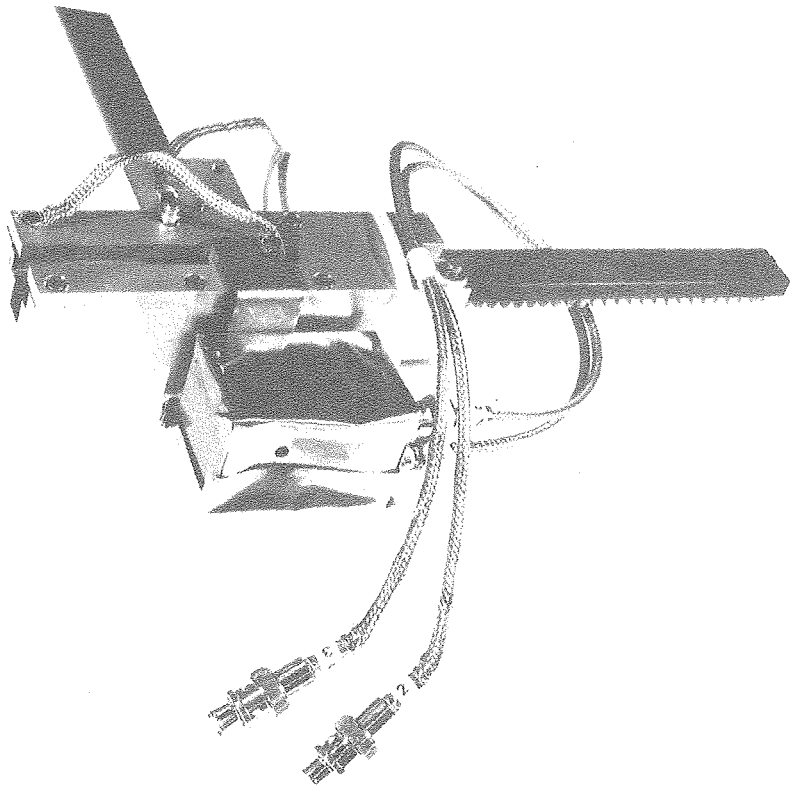

CBB 800-12559

Figure 2.9 The Small Faraday Cup (SFC)

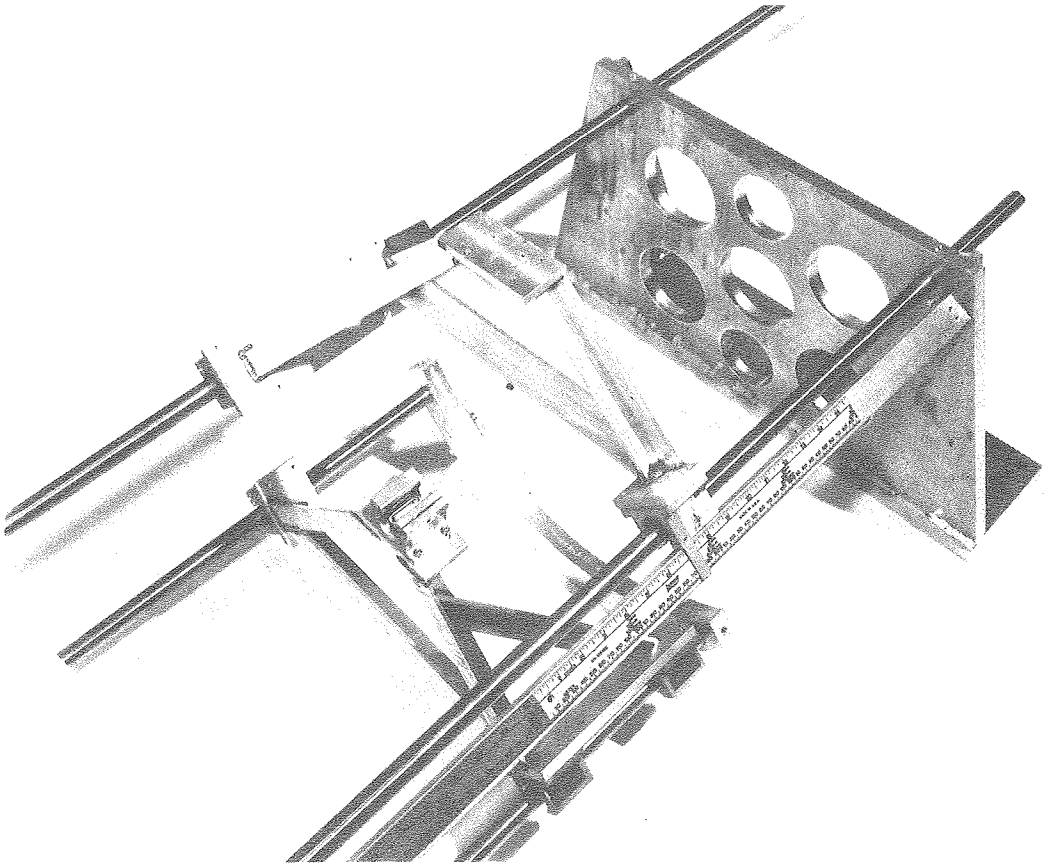

CBB 800-12557

Figure 2.10 R-Θ Probe Support Rails

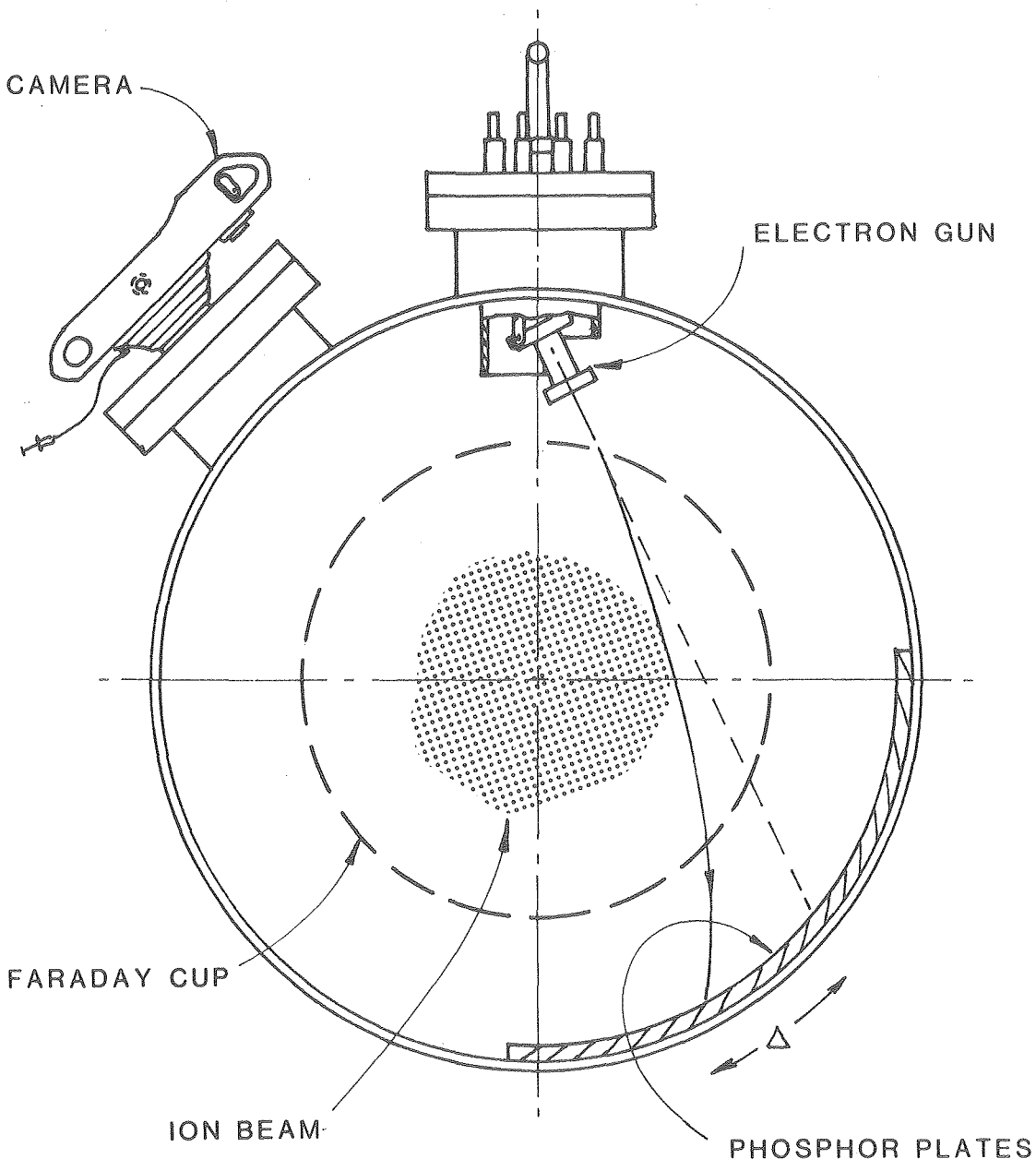

XBL 823-8740

Figure 3.1 End View of the Diagnostic Tank Showing EBP

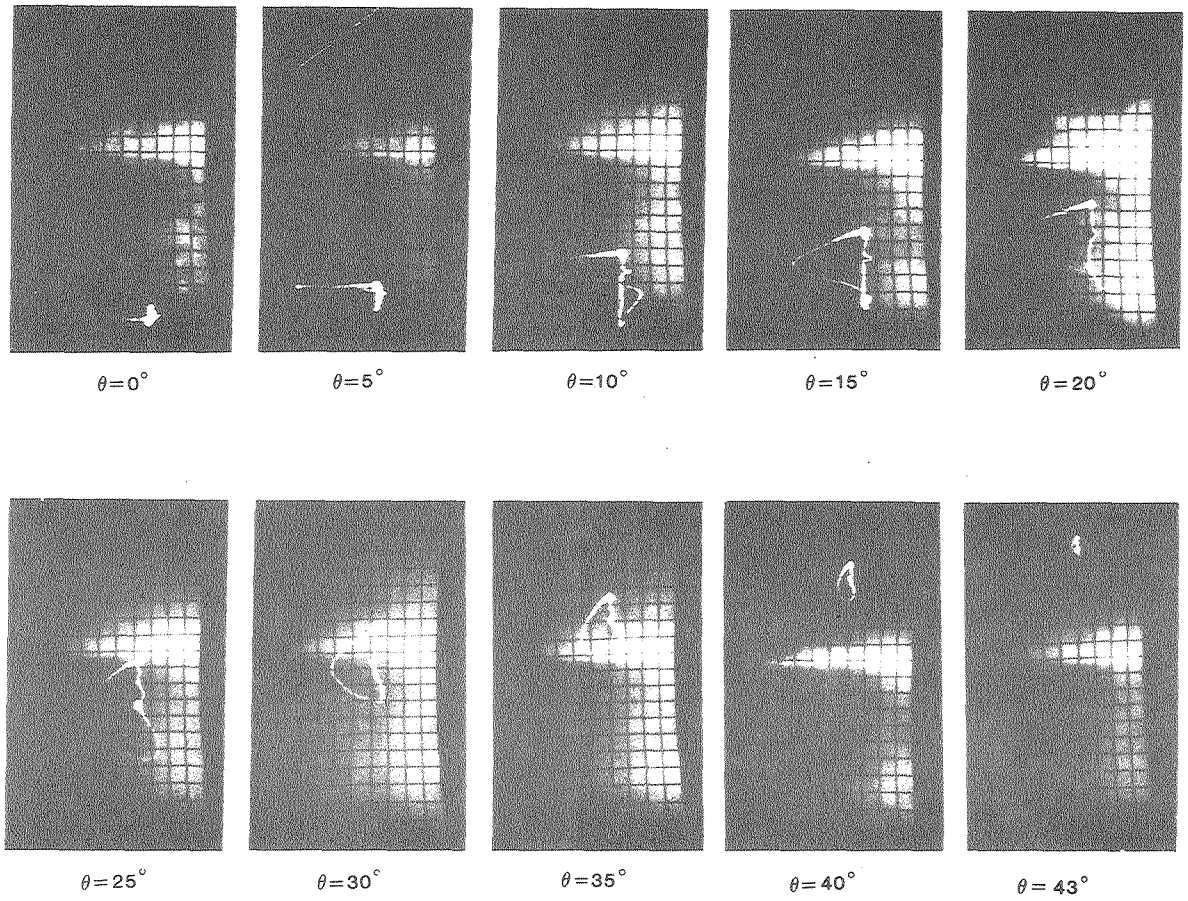

Figure 3.2 Example Data Set of EBP Traces

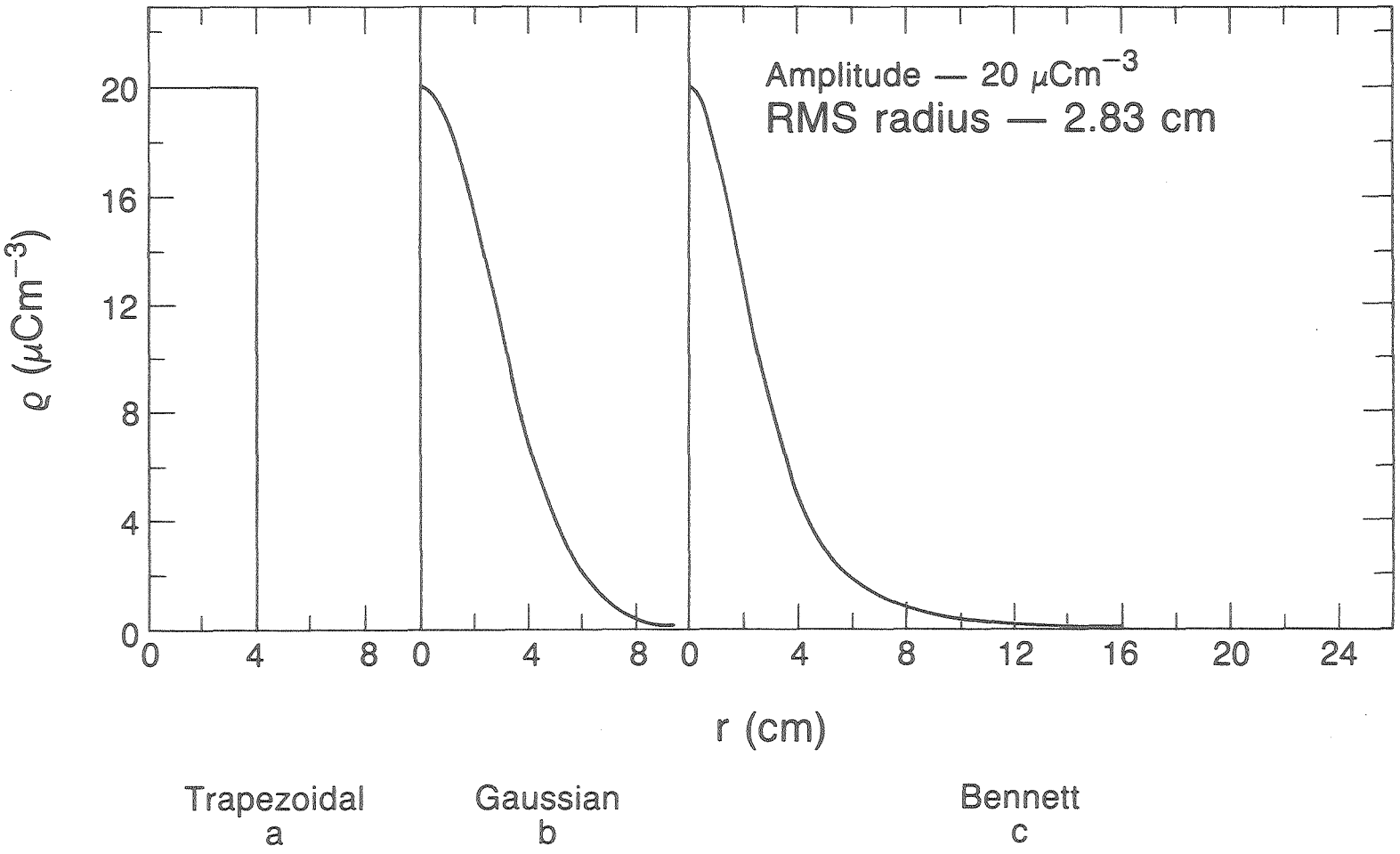

Figure 3.3 Rectangular, Gaussian, and Bennett Radial Distribution Functions

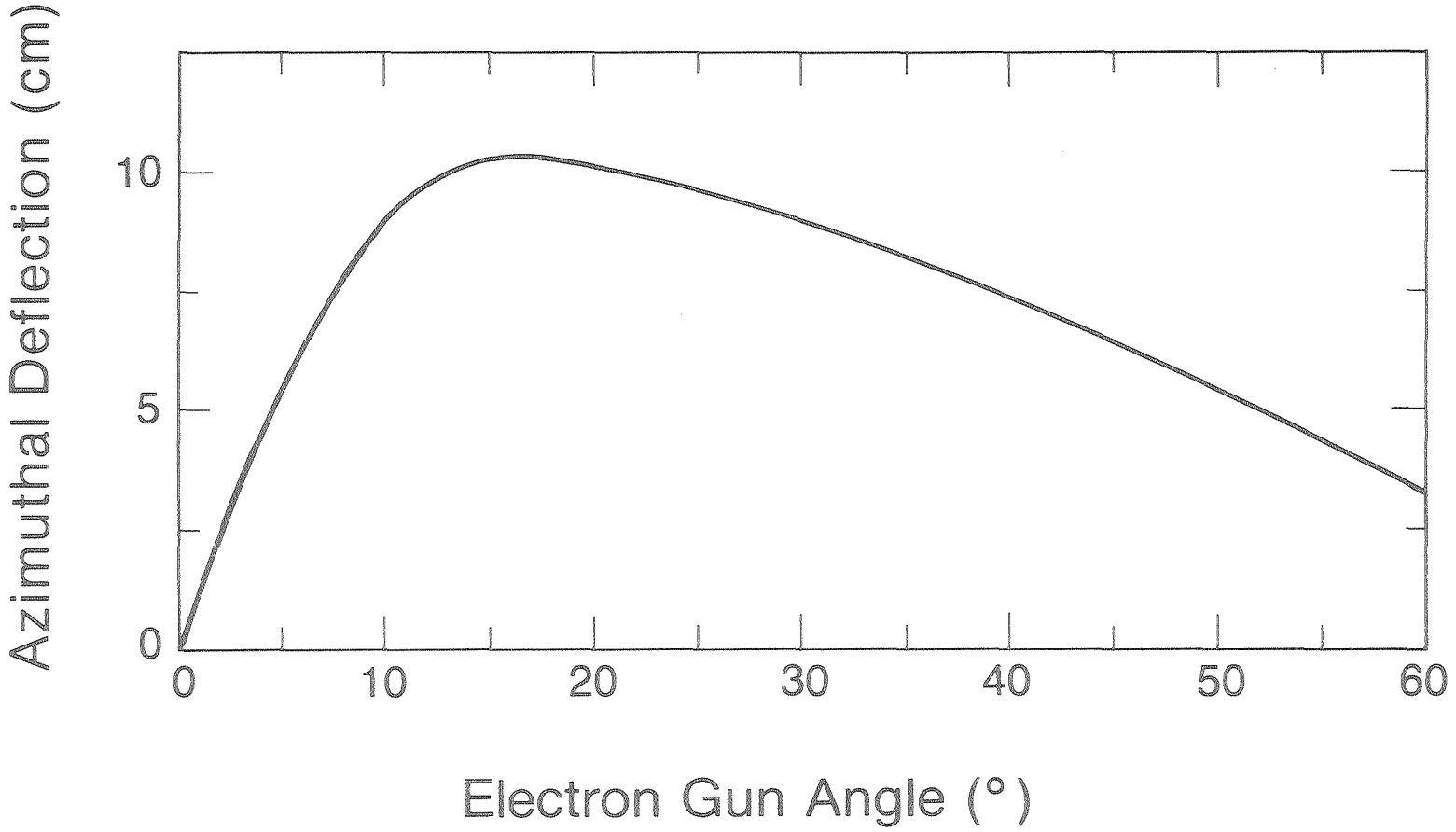

Figure 3.4 EBEAM Code Calculation of Azimuthal Deflection vs. Electron Gun Angle for the Gaussian Distribution

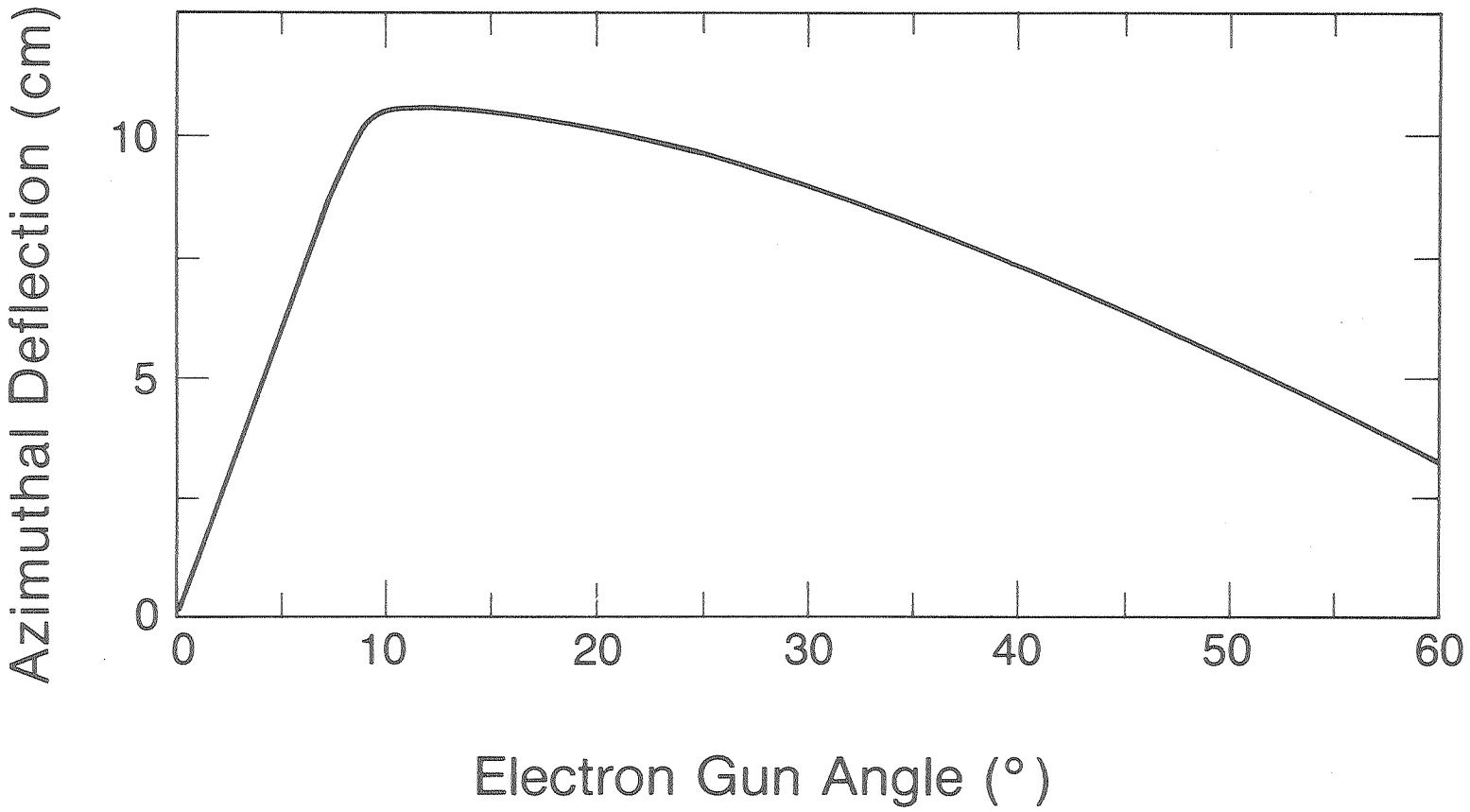

Figure 3.5 EBEAM Code Calculation of Azimuthal Deflection vs. Electron Gun Angle for the Rectangular Distribution

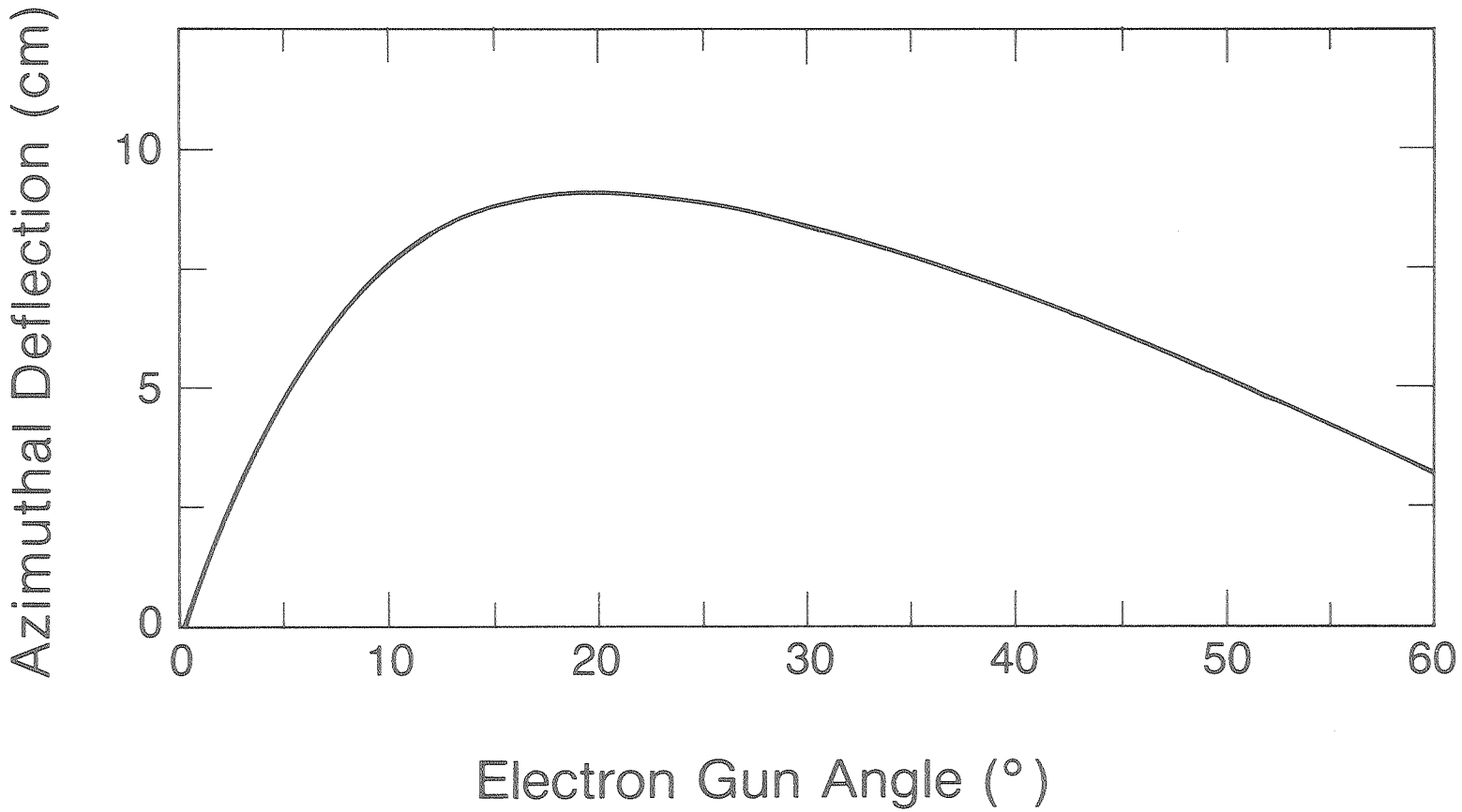

Figure 3.6 EBEAM Code Calculation of Azimuthal Deflection vs. Electron Gun Angle for the Bennett Distribution

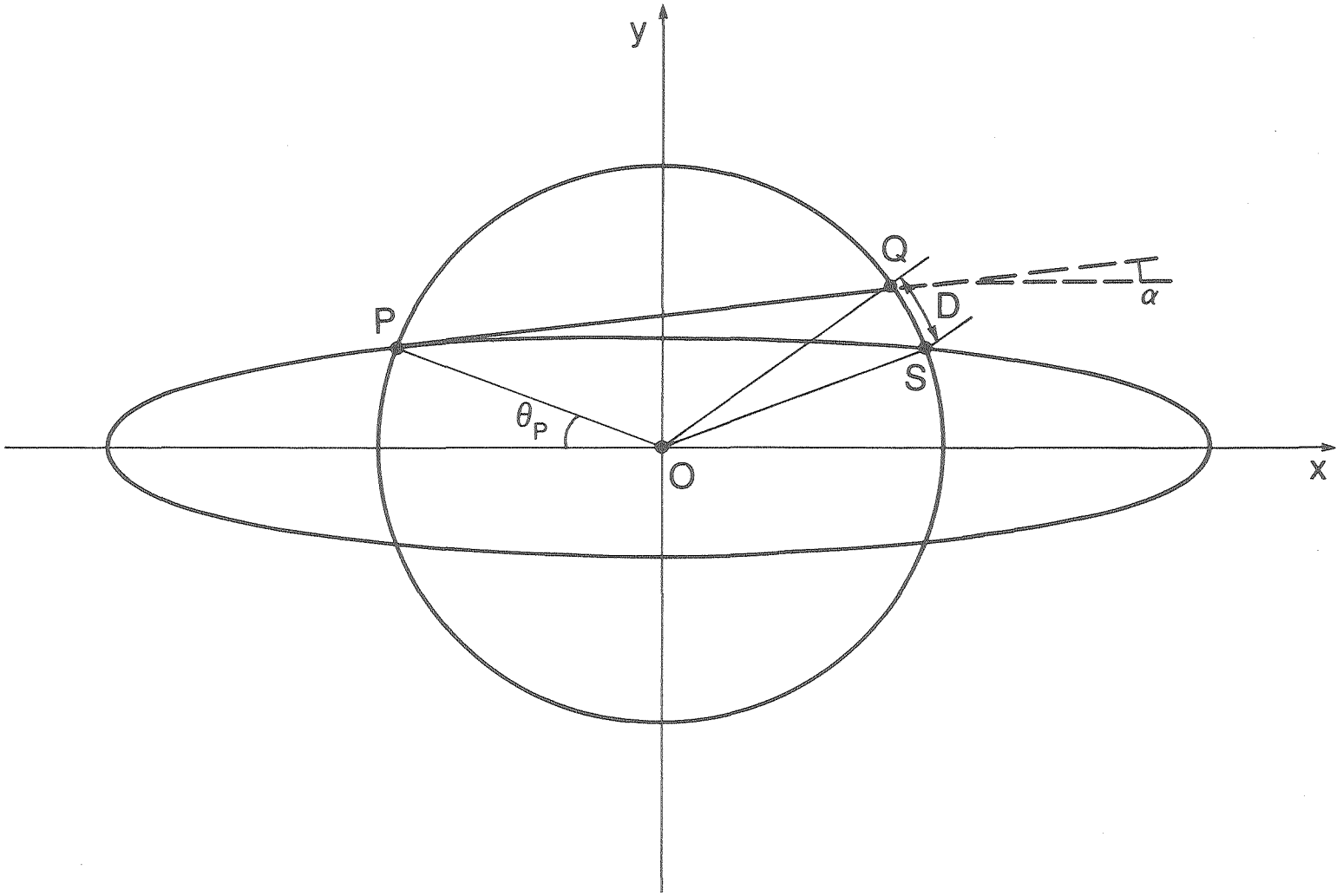

XBL 8311-7380

Figure 3.7 Geometry for the Analysis of Small Angle Deflections

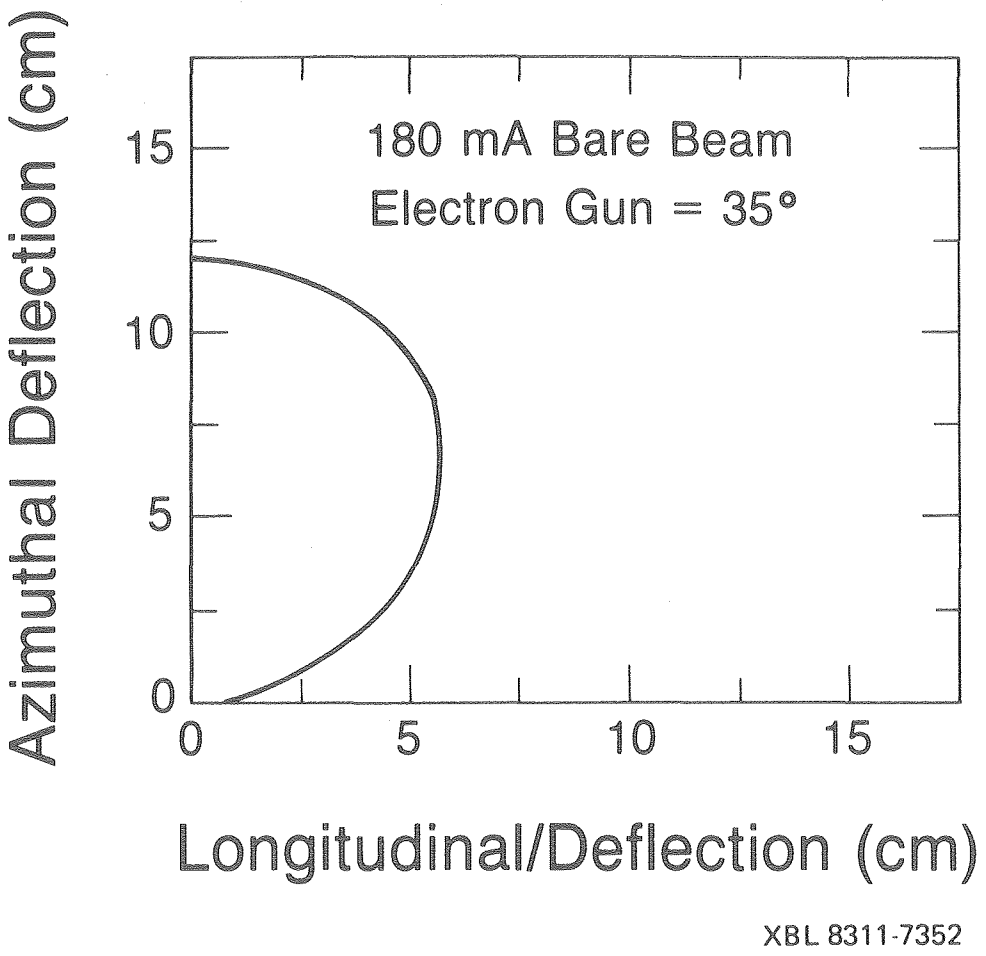

Figure 3.8 3-D EBEAM Code Calculation of Longitudinal and Azimuthal Deflection (a Trace) for an Electron Gun Angle of 35°

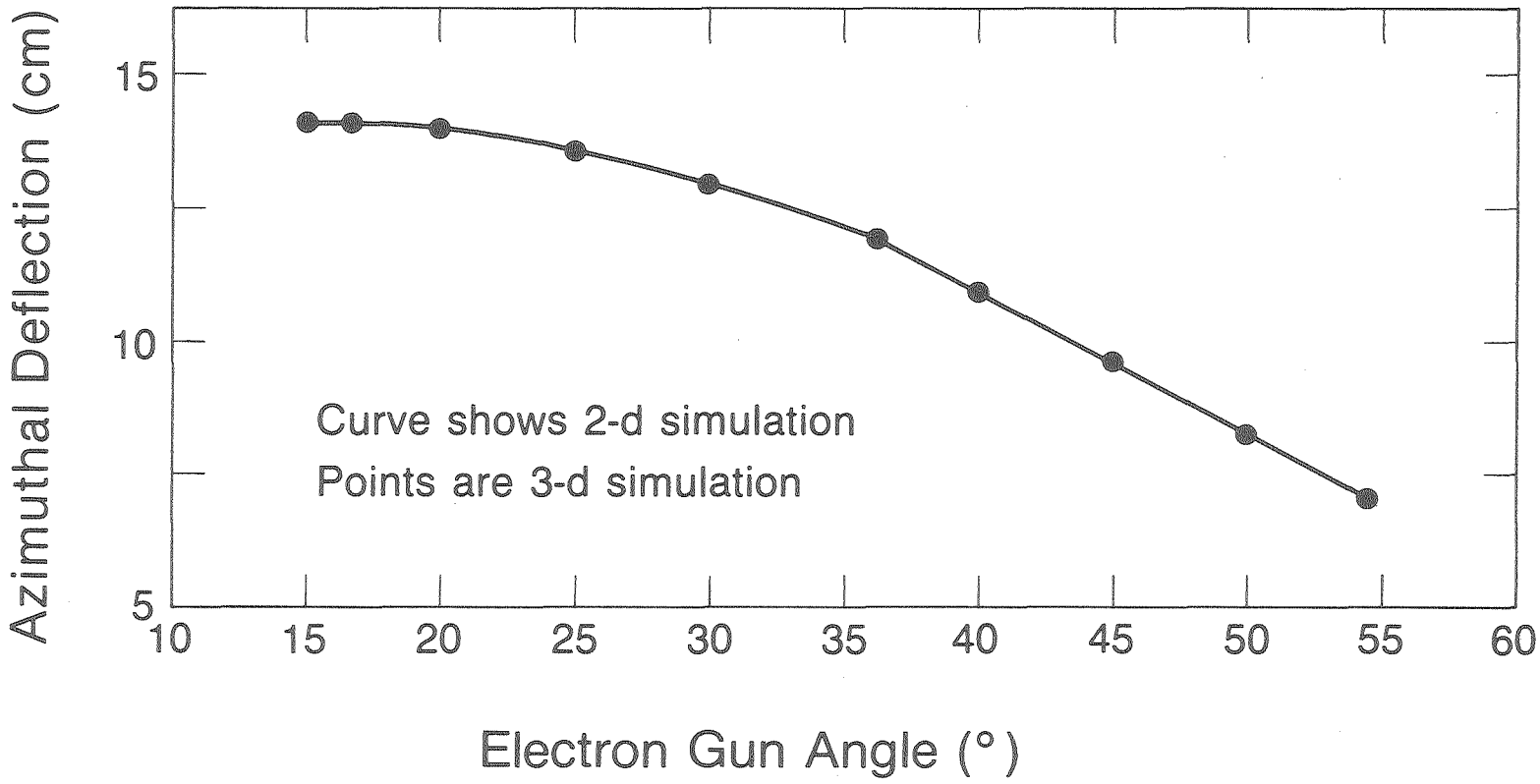

Figure 3.9 2-D and 3-D Azimuthal Deflections Calculated by EBEAM Compared

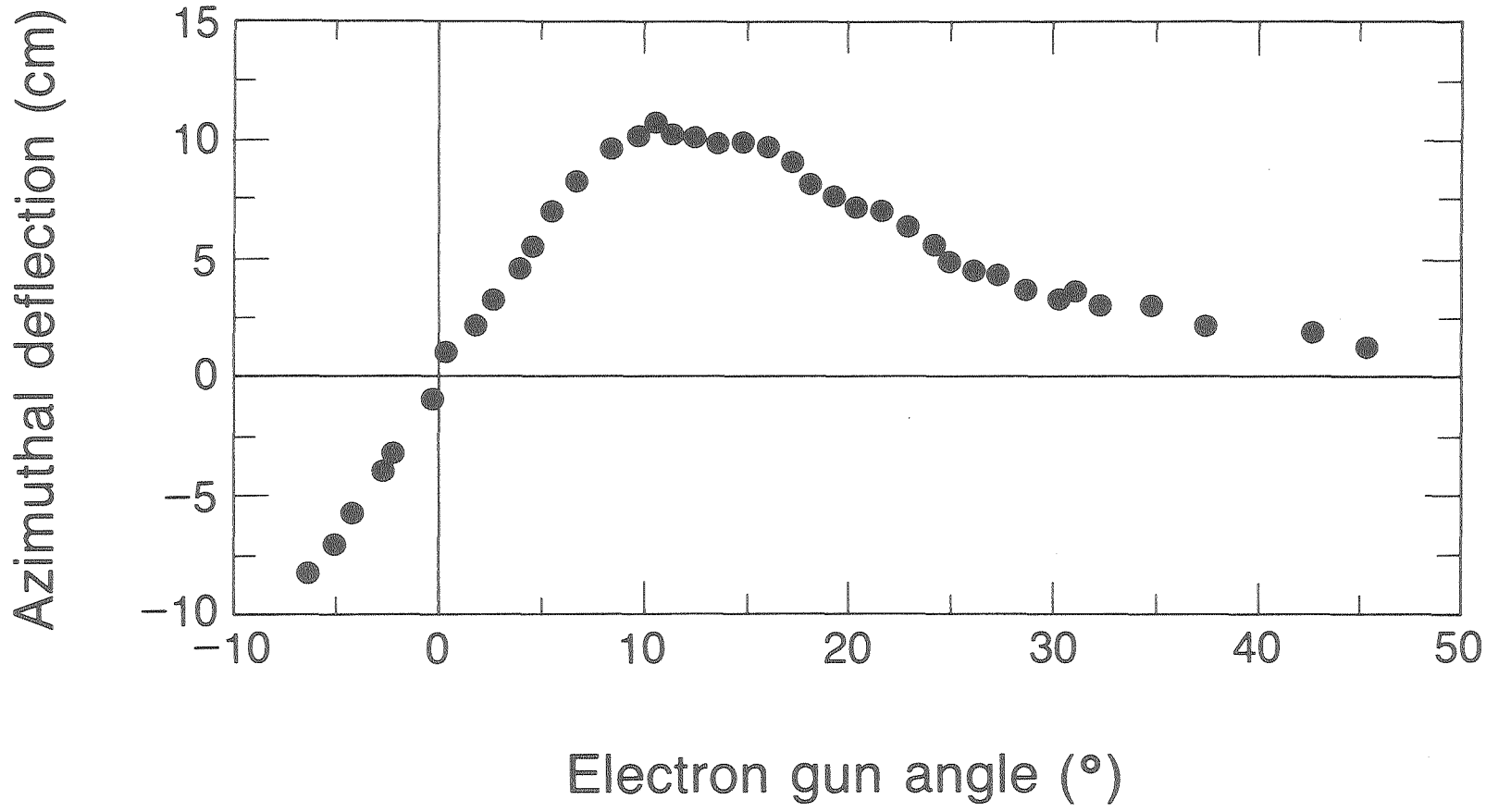

XBL 8311-7370

Figure 4.1 6-1-82 Data: Azimmuthal Deflection vs. Electron Gun Angle

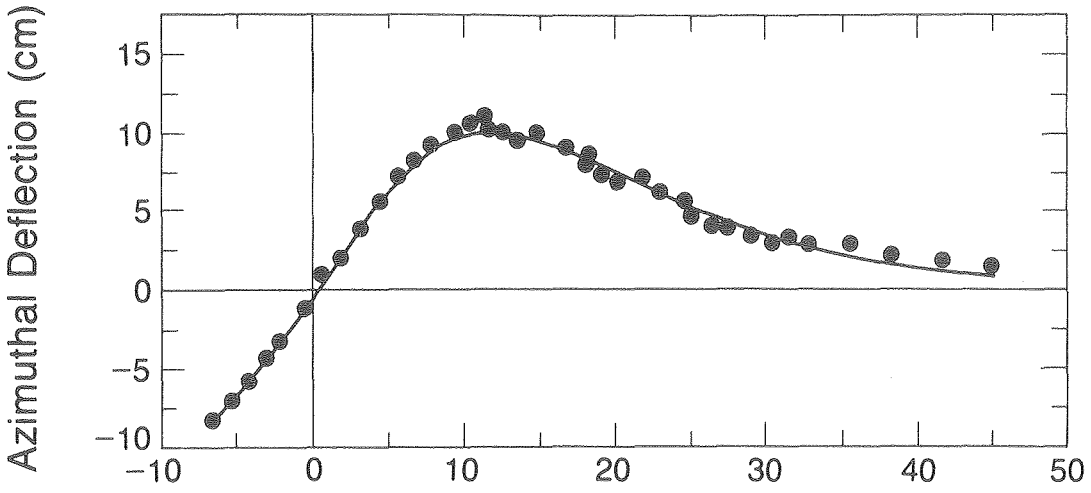

Figure 4.2A 6-1-82 Azimuthal Data and the Best Computer Fit

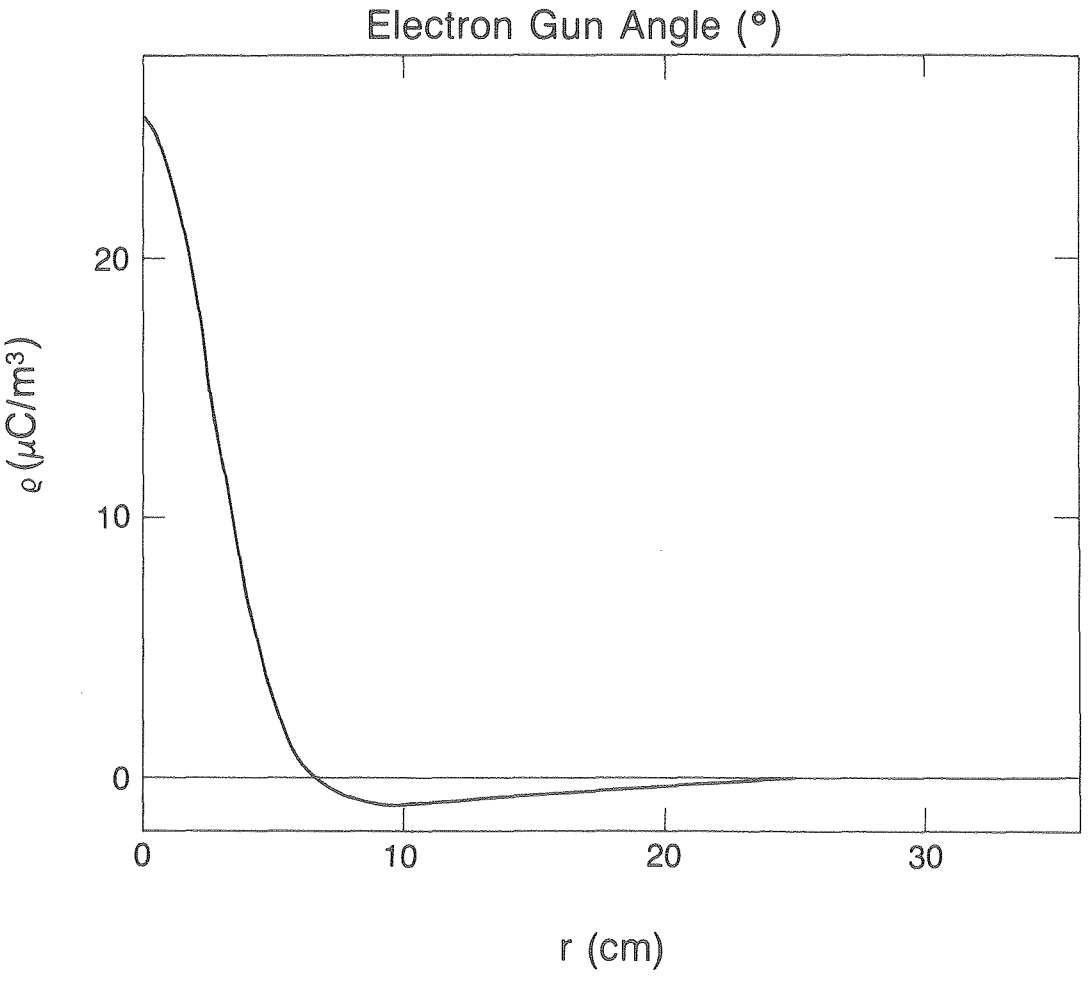

Figure 4.2B Model Charge Distribution Giving Best Fit to 6-1-82 Data

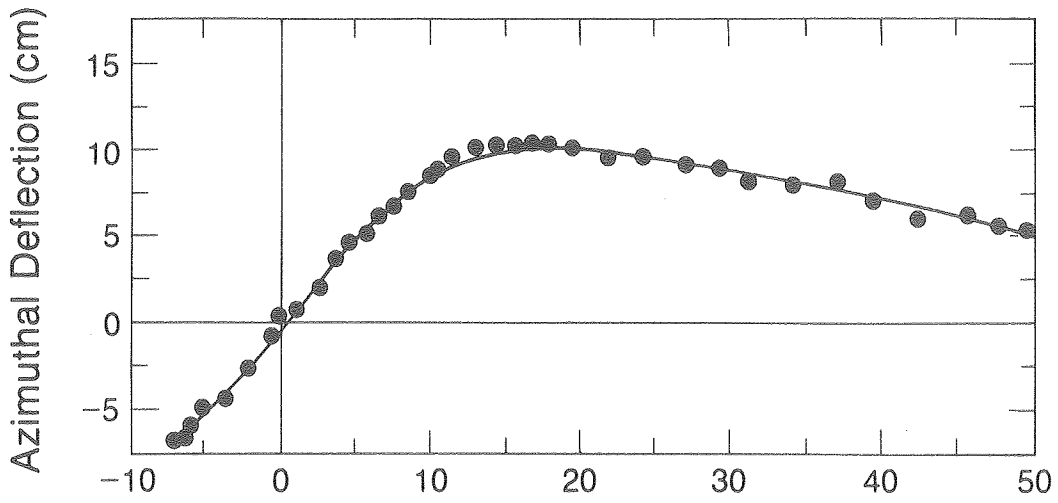

Figure 4.3A 6-2-82 Azimuthal Deflection Data and the Best Computer Fit

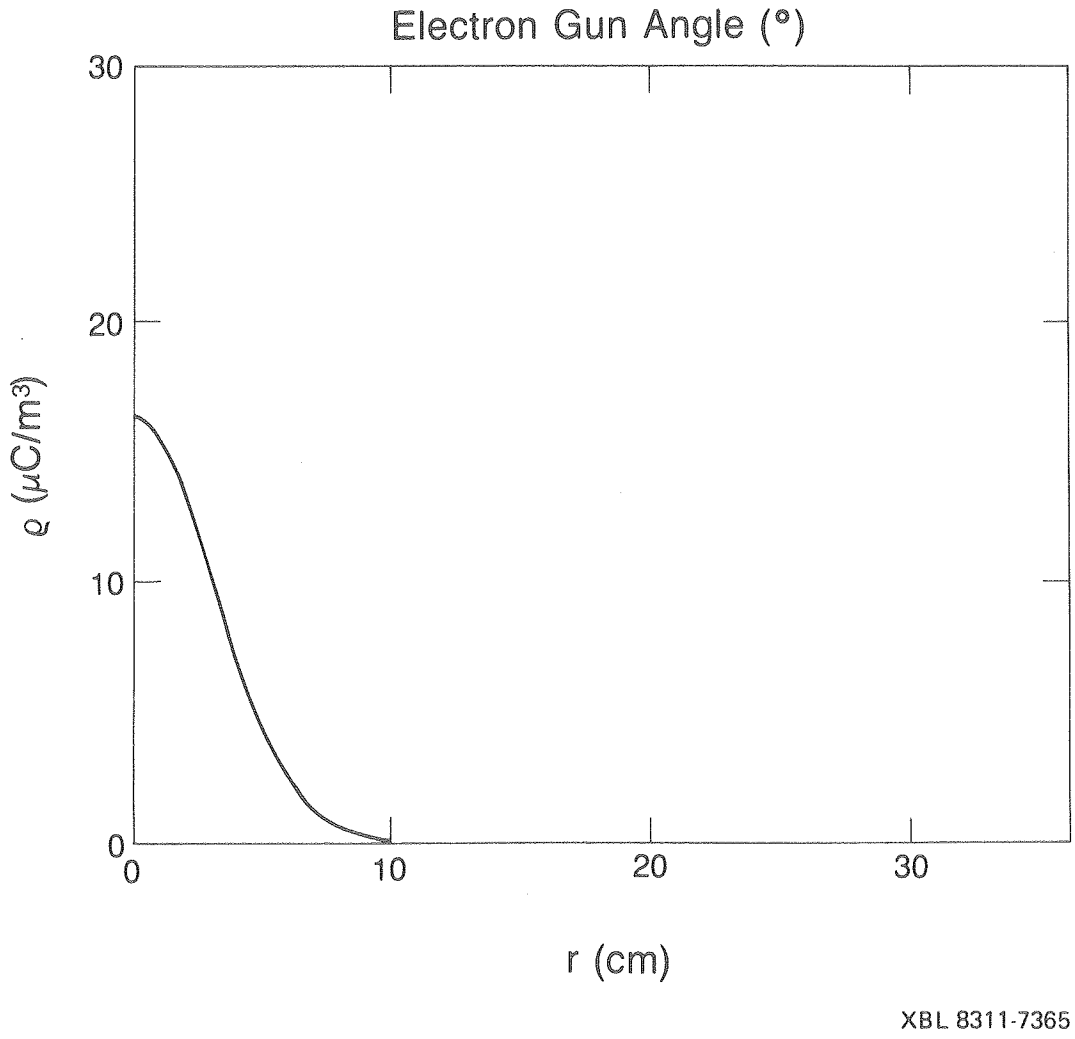

Figure 4.3B Model Charge Distribution Giving Best Fit to 6-2-82 Data

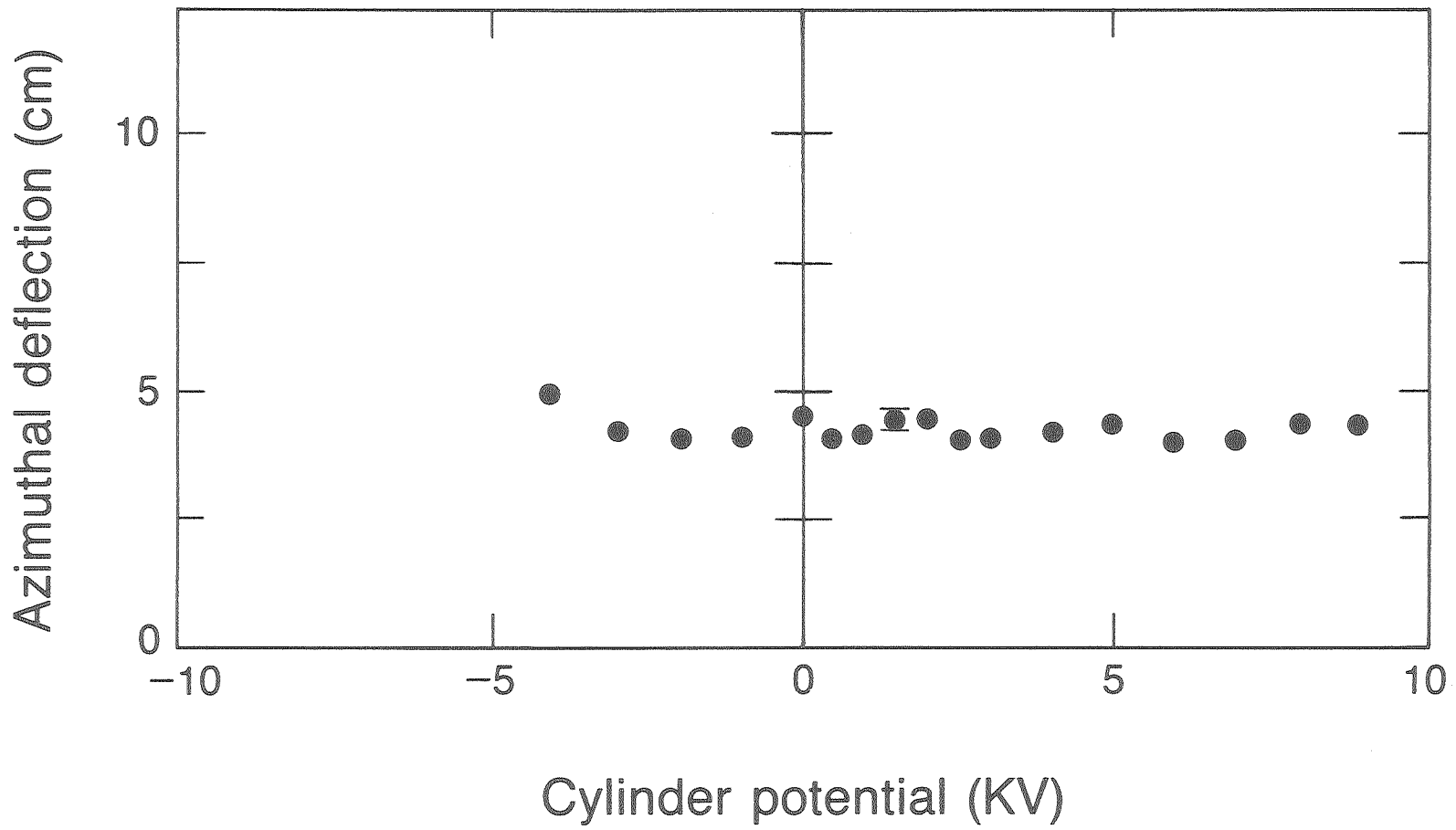

Figure 4.4 Azimuthal Deflection vs. Voltage Cylinder Bias at 4.9° E-Gun Angle

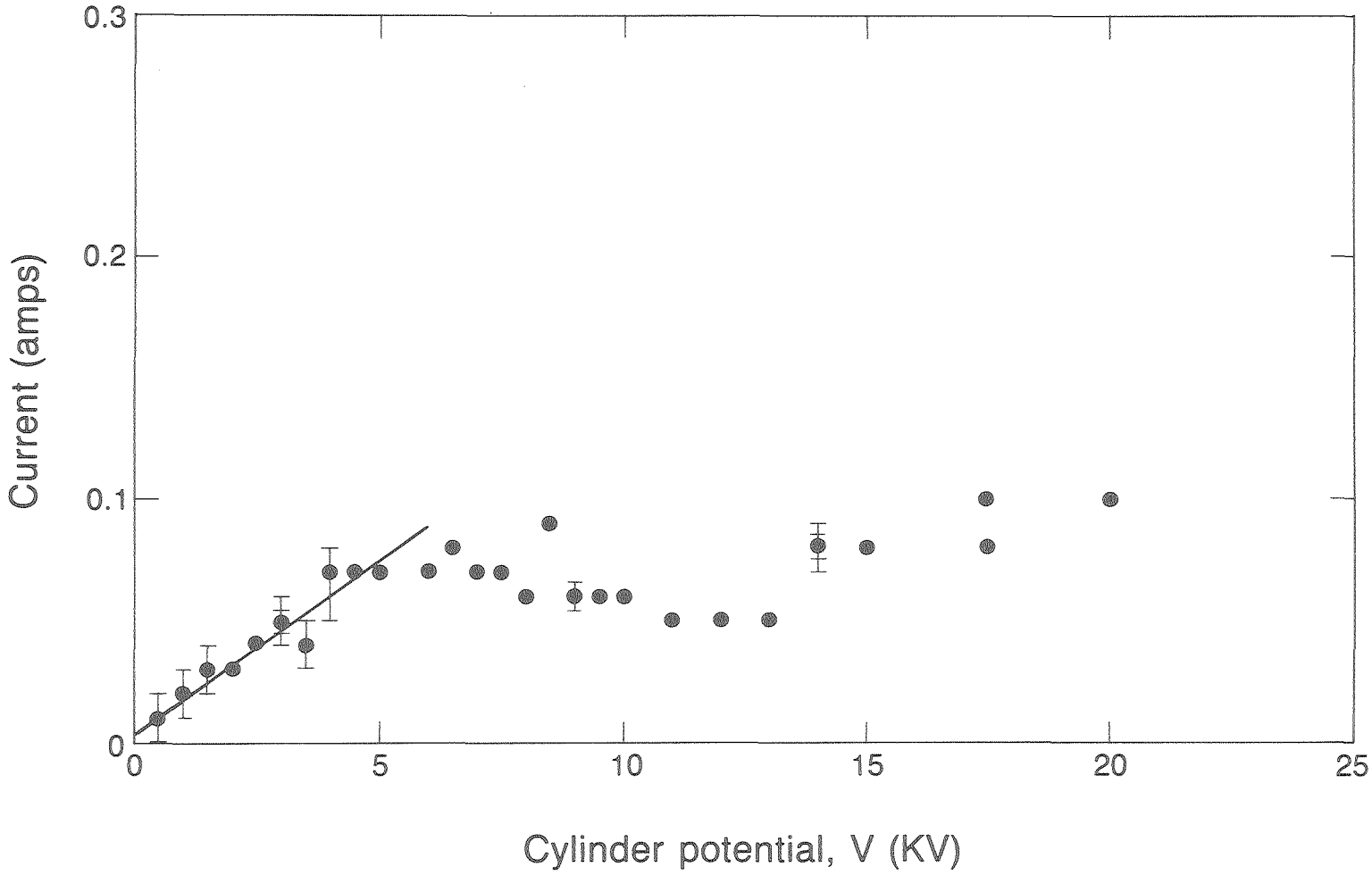

XBL 8311-7355

Figure 4.5 Pearson Probe Current Measuring Electron Energy Distribution for Configuration III

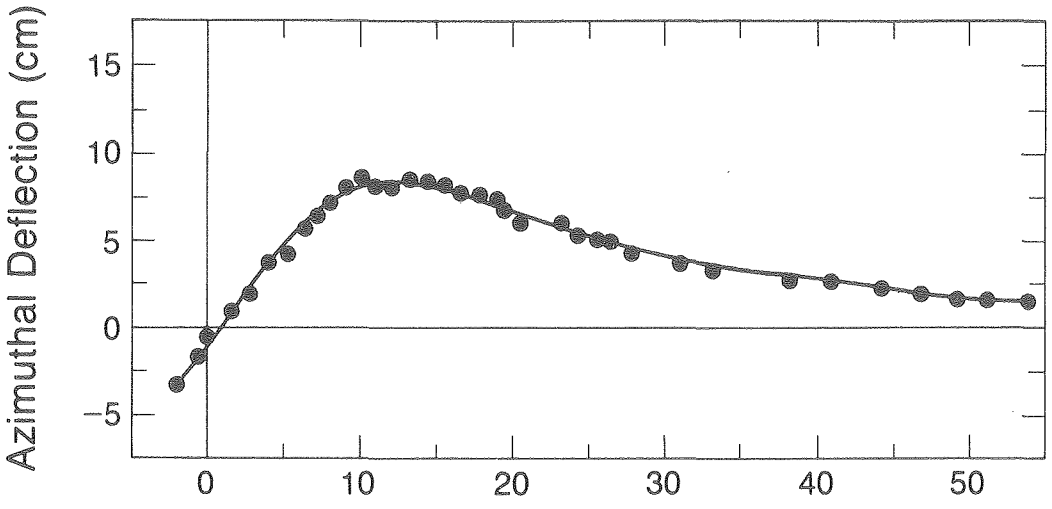

Figure 4.6A 9-1-82 Azimuthal Deflection Data and the Best Computer Fit Using Two Gaussian Distribution Functions

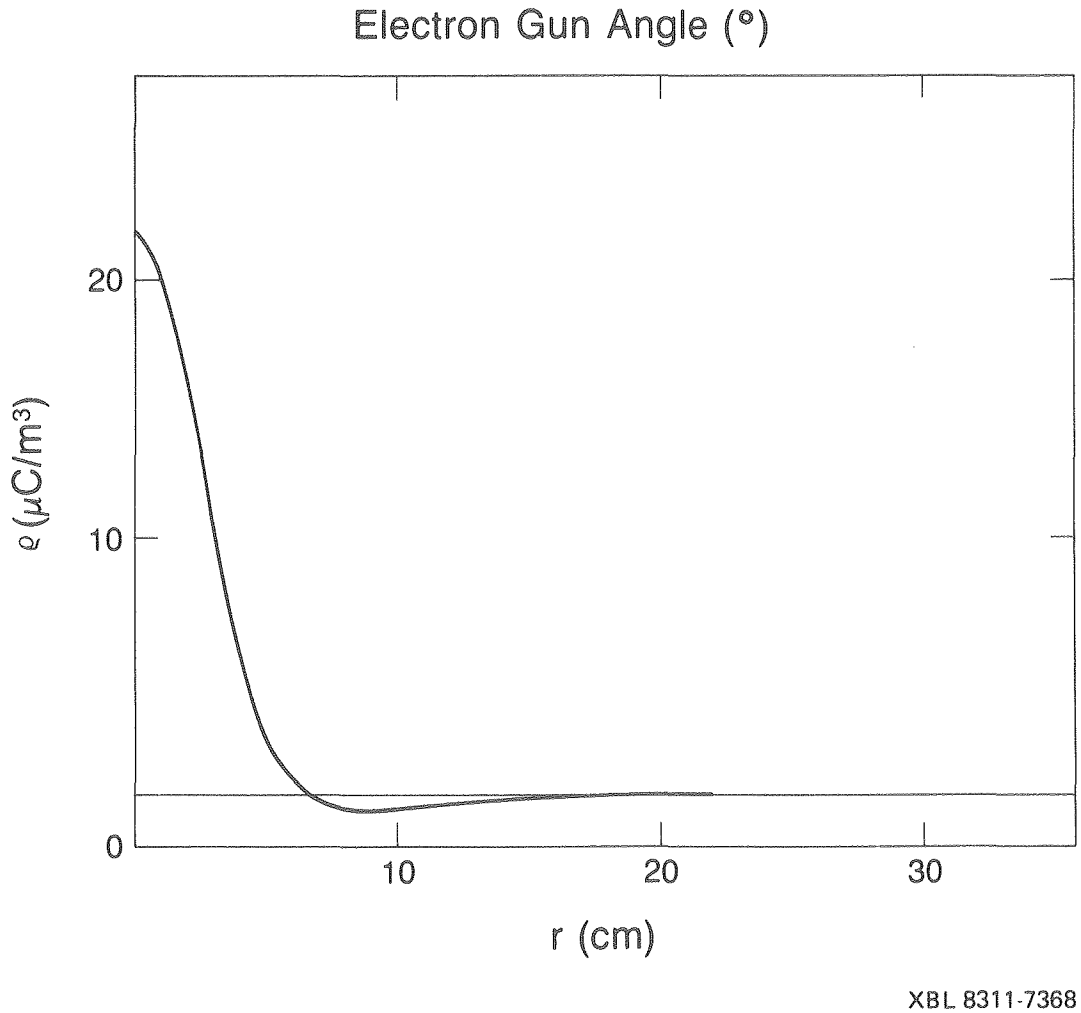

Figure 4.6B Two Gaussian Model Charge Distribution Giving the Best Fit to 9-1-82 Azimuthal Deflection Data

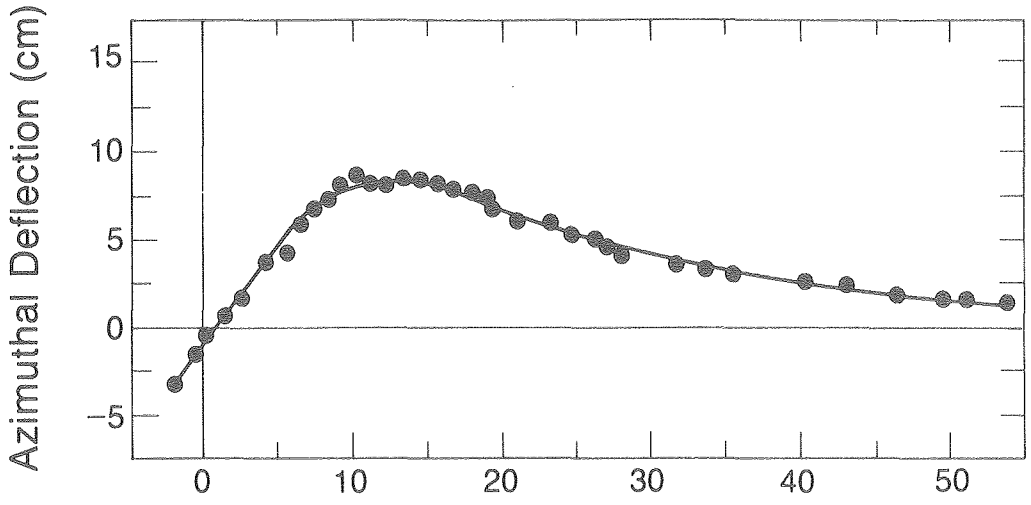

Figure 4.7A 9-1-82 Azimuthal Deflection Data and the Best Computer Fit Using a Gaussian and R^2 x Gaussian Distribution Functions

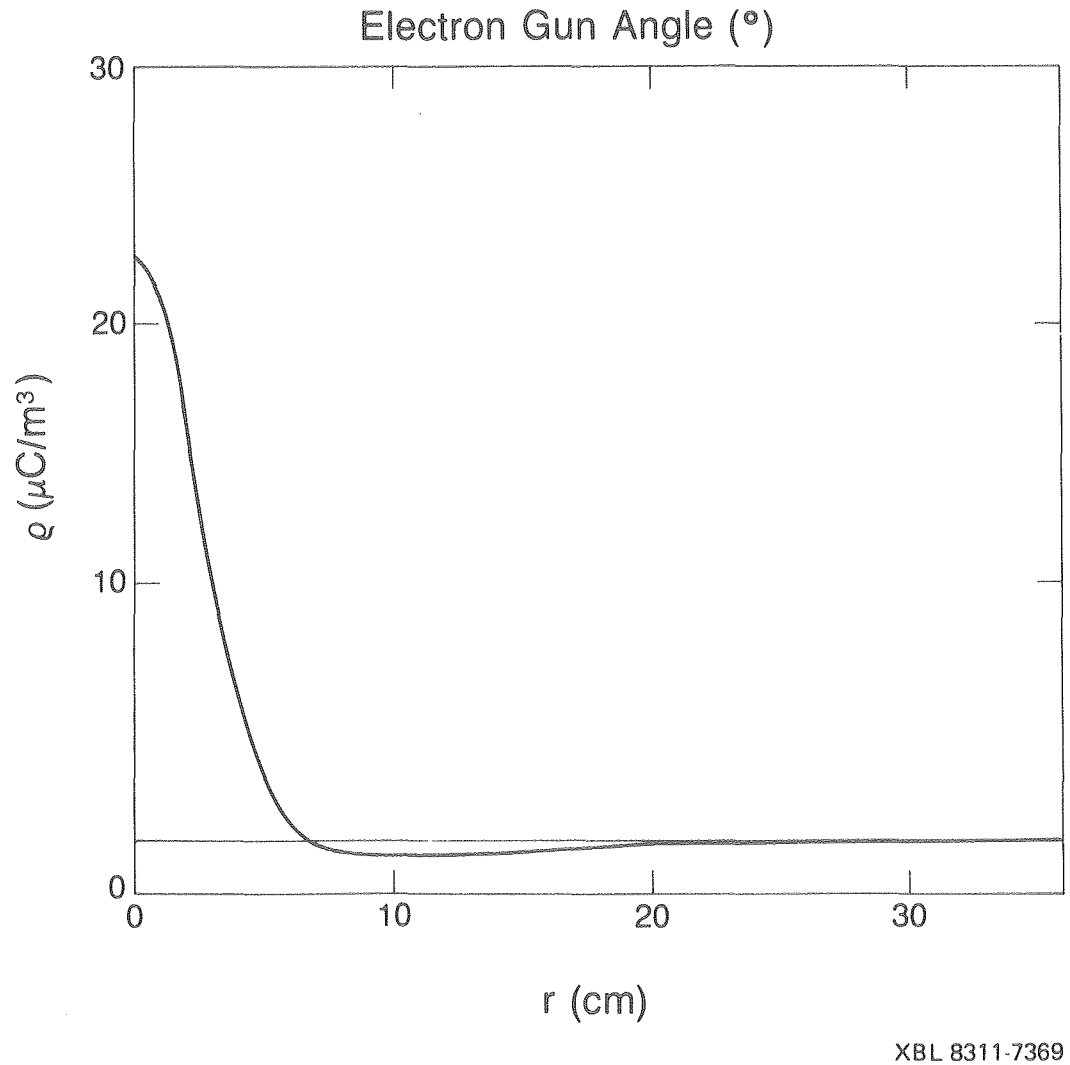

Figure 4.7B Gaussian + R^2 x Gaussian Model Charge Distribution Giving the Best Fit to 9-1-82 Azimuthal Deflection Data

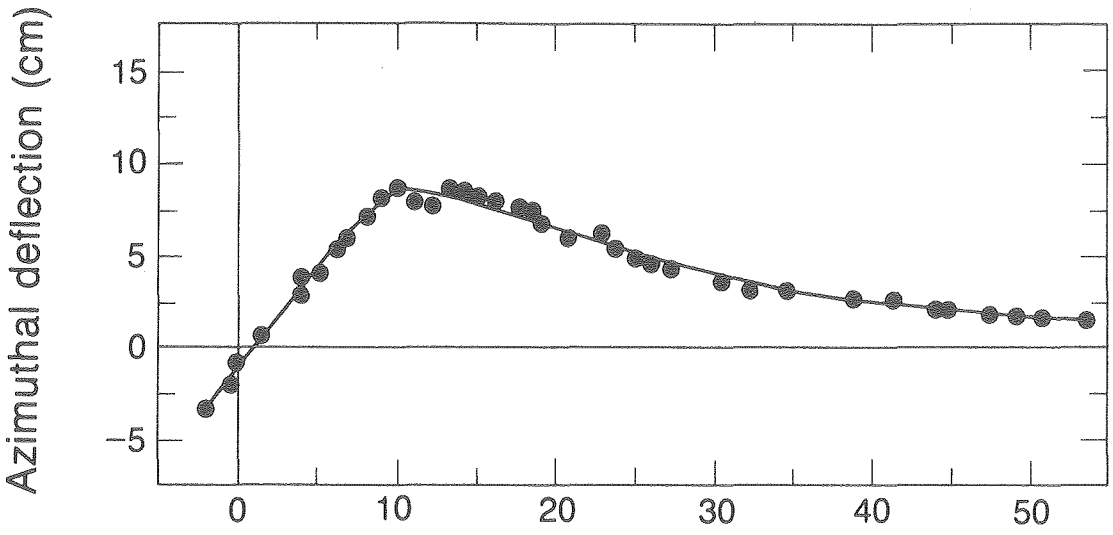

Figure 4.8A 9-1-82 Azimuthal Deflection Data and the Best Computer Fit Using a Trapezoidal and R^2 x Gaussian Distribution Functions

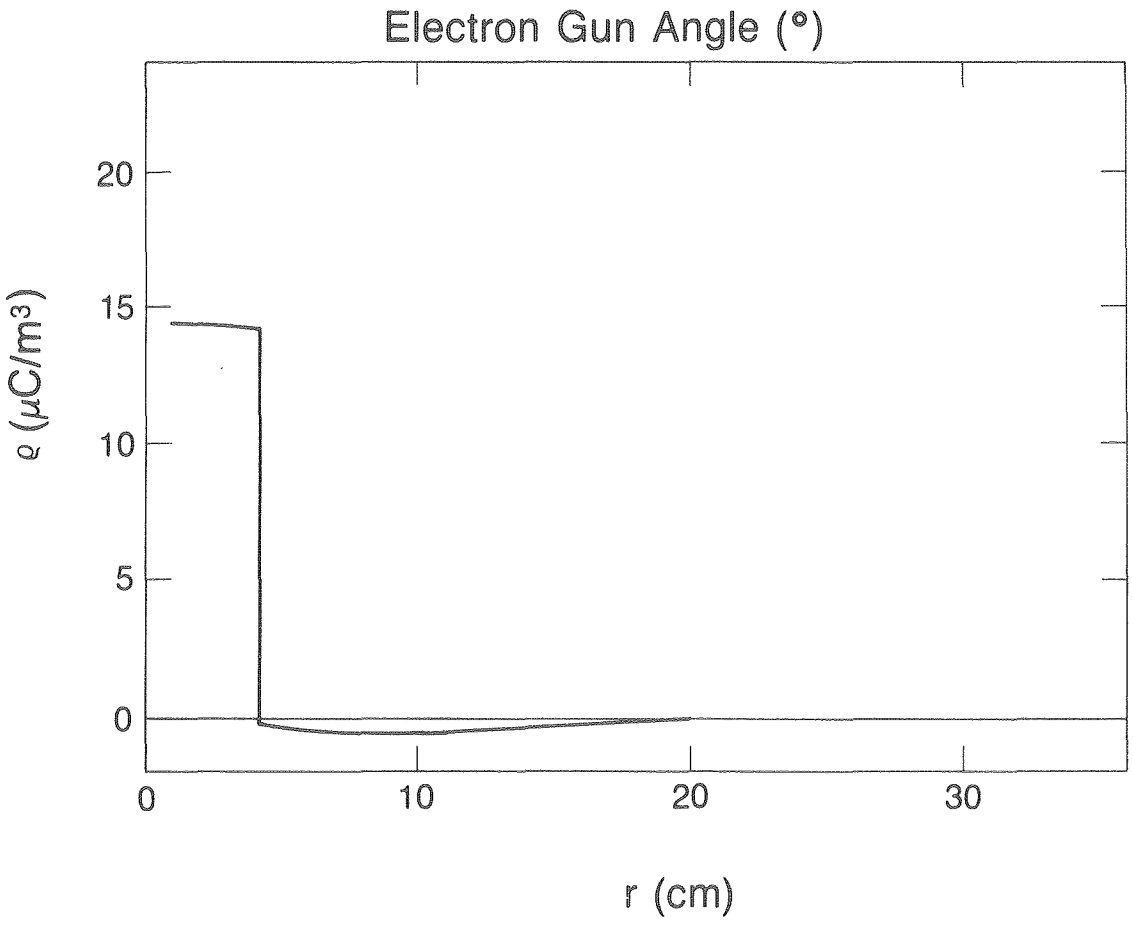

Figure 4.8B Trapezoidal + R^2 x Gaussian Model Charge Distribution Functions

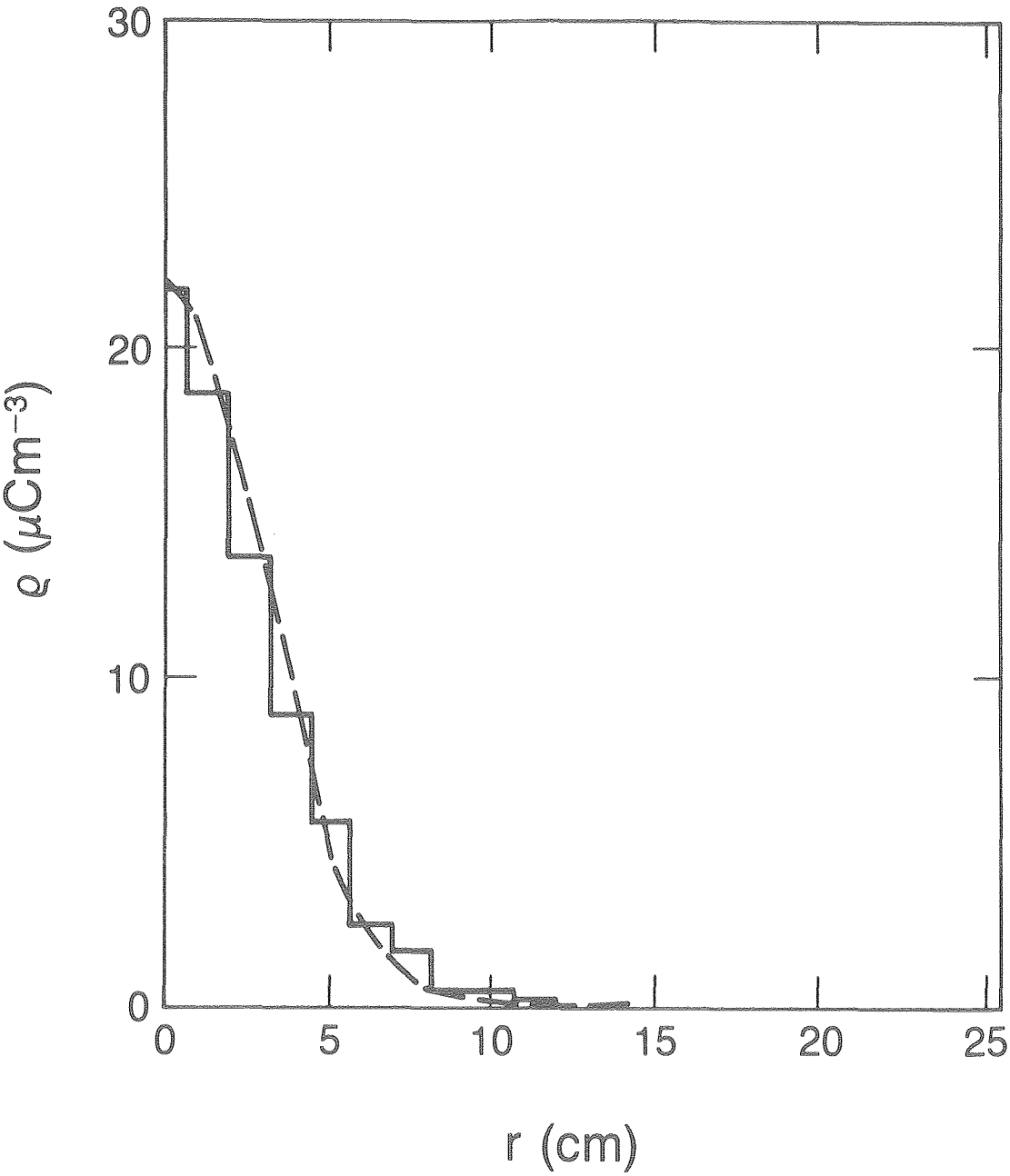

Figure 4.9 Gaussian Fit to SFC Measurements

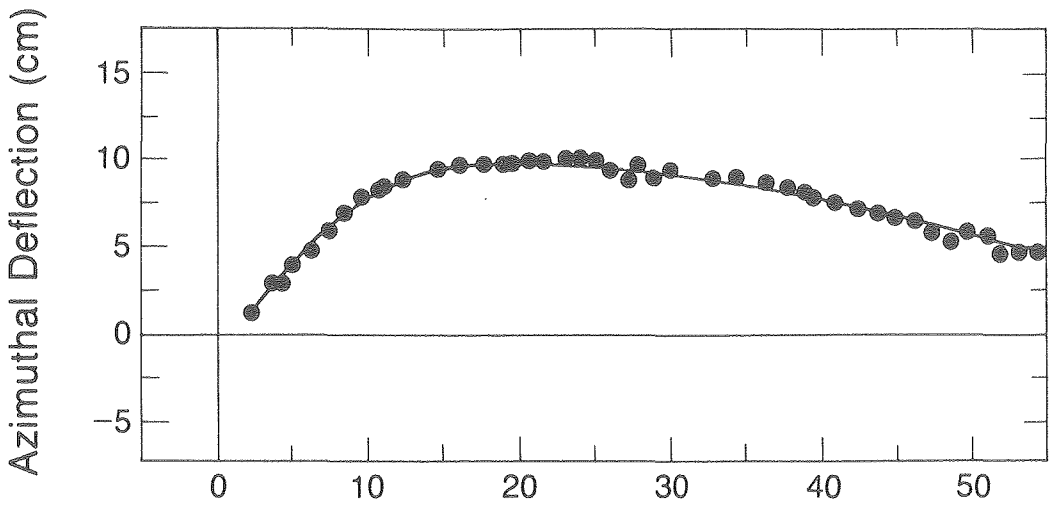

Figure 4.10A 6-14-82 Azimuthal Deflection Data and Best Computer Fit

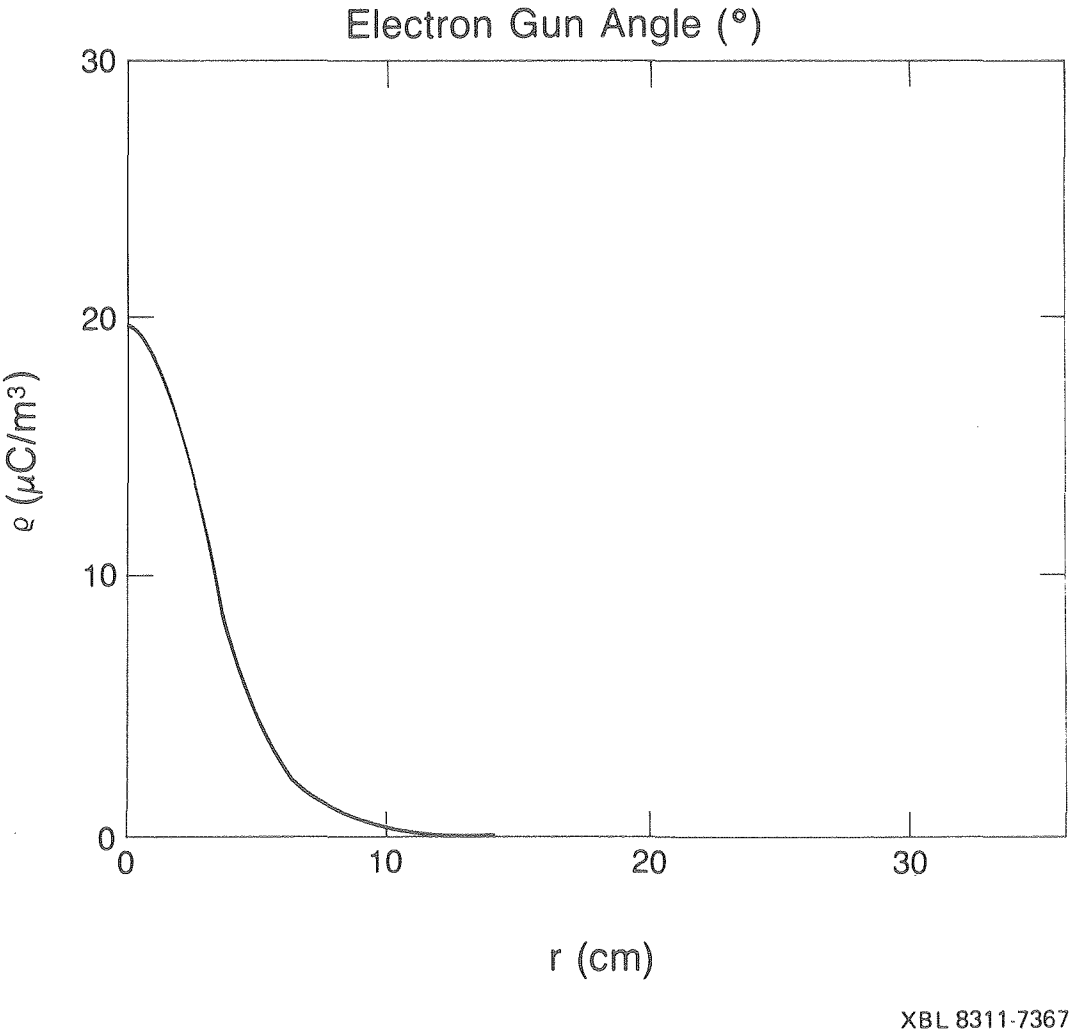

Figure 4.10B Model Charge Distribution Giving Best Fit to 9-1-82A Data

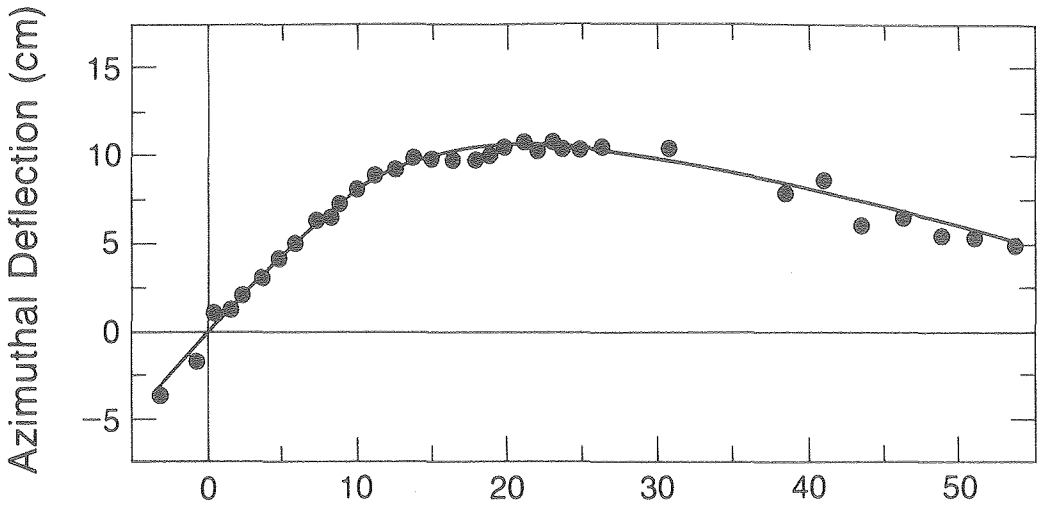

Figure 4.11A 9-1-82A Azimuthal Deflection Data and Best Computer Fit

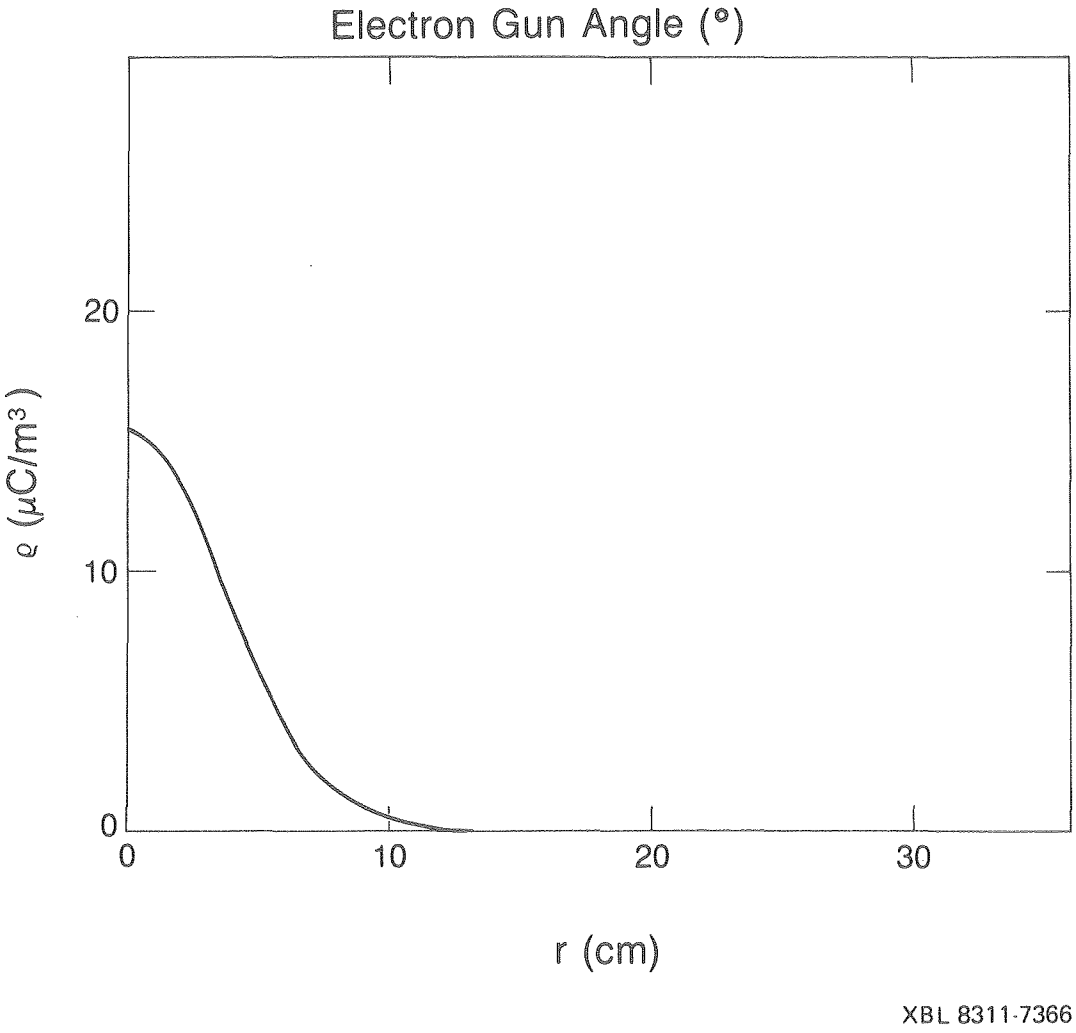

Figure 4.11B Model Charge Distribution Giving Best Fit to 9-1-82A Data

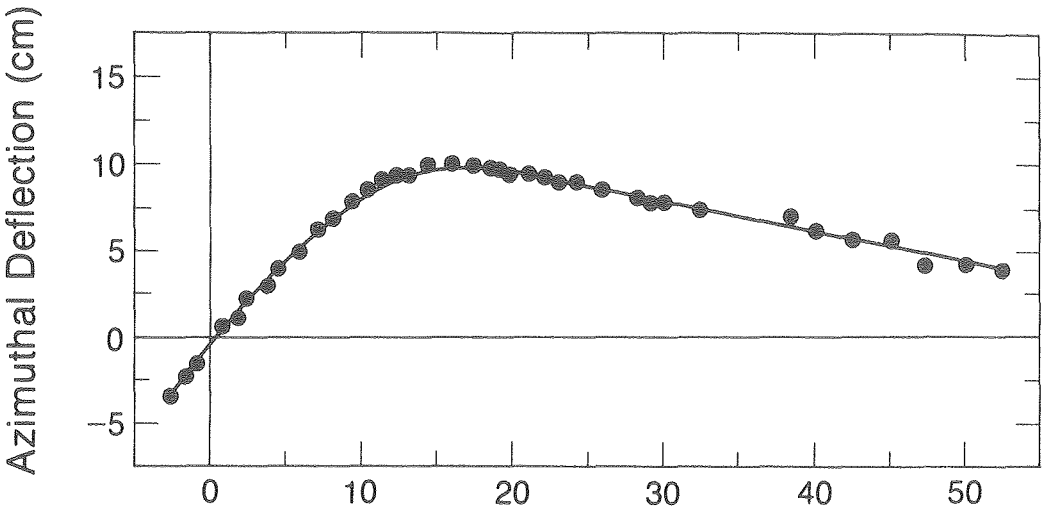

Figure 4.12A 9-2-82 Azimuthal Deflection Data and Best Computer Fit

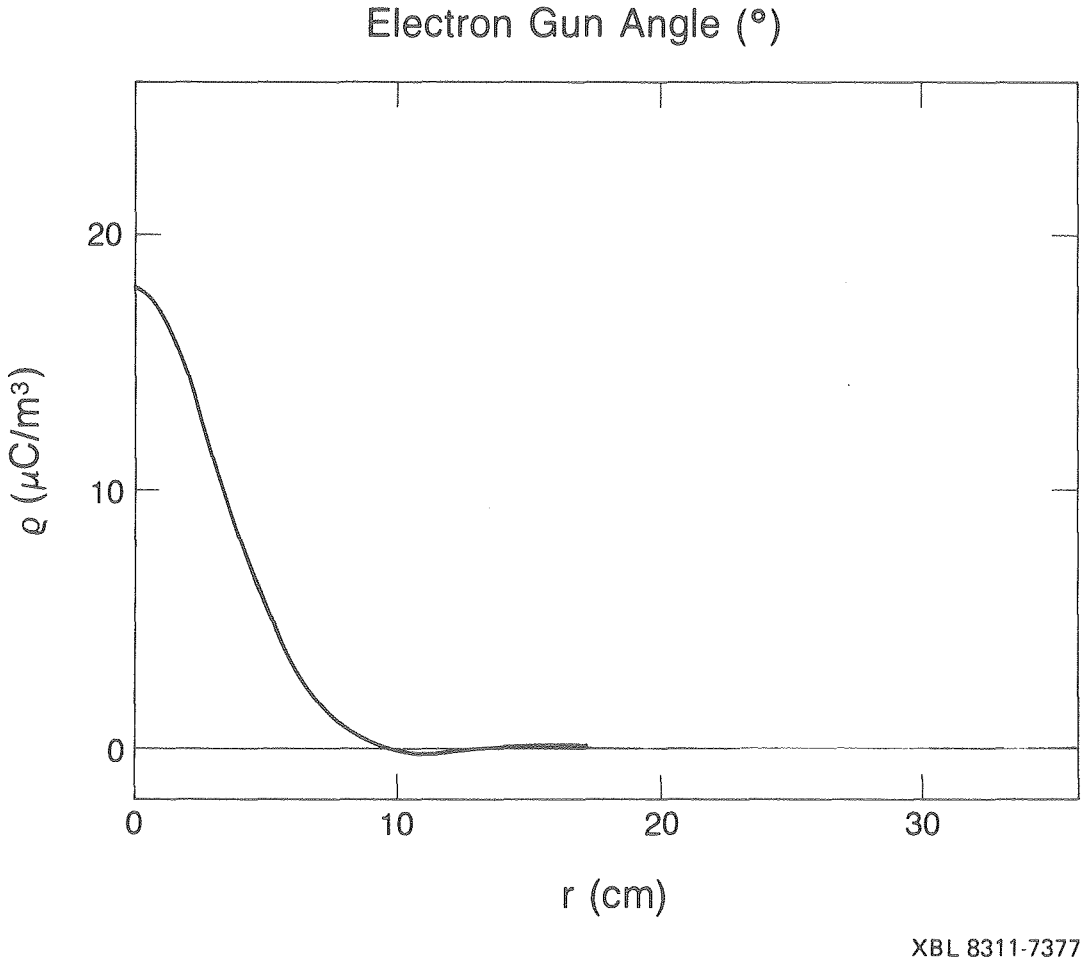

Figure 4.12B Model Charge Distribution Giving Best Fit to 9-2-82 Data

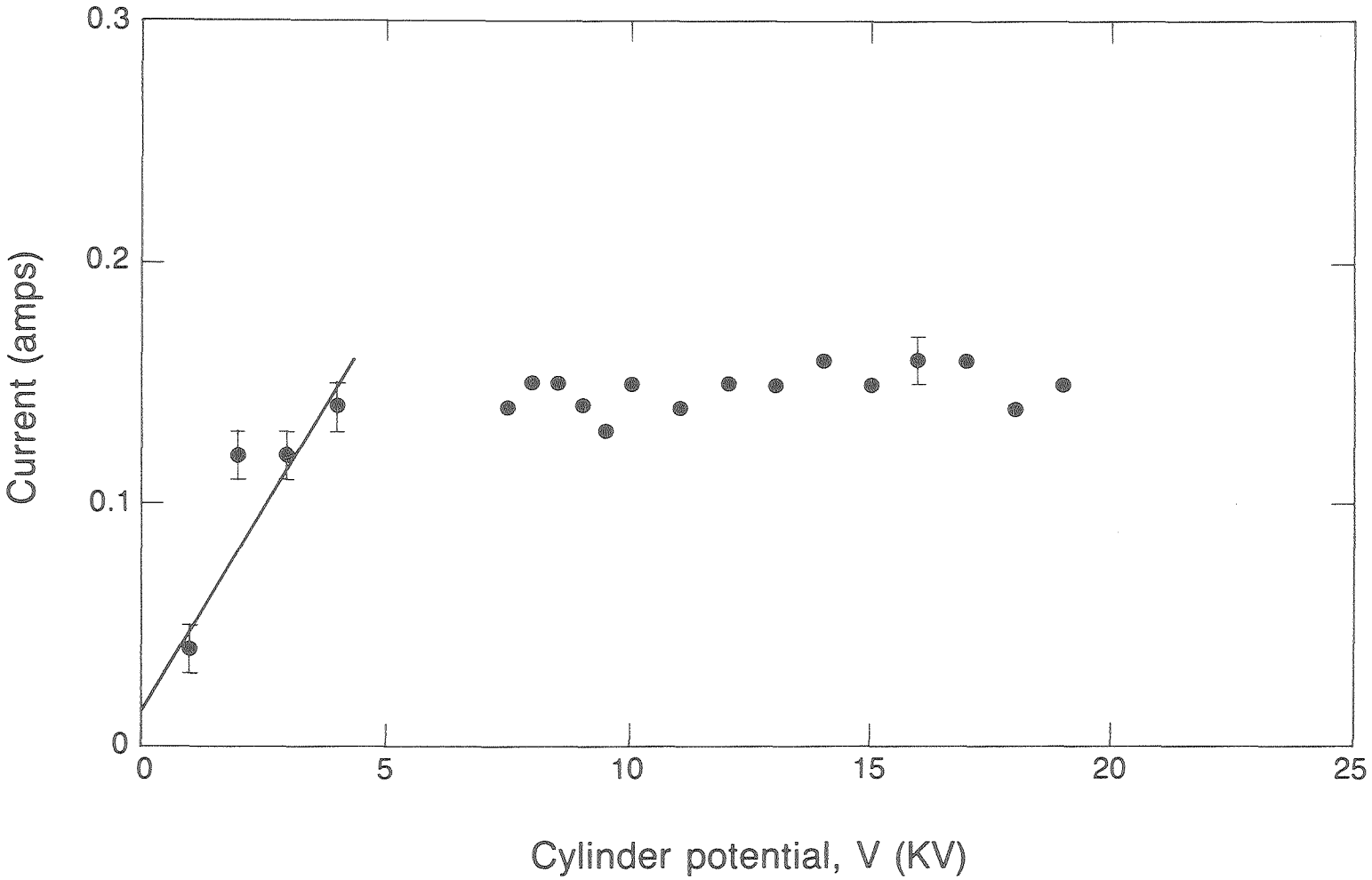

XBL 8311-7356

Figure 4.13 Configuration I: Pearson Probe Current Measuring Electron Energy Distribution

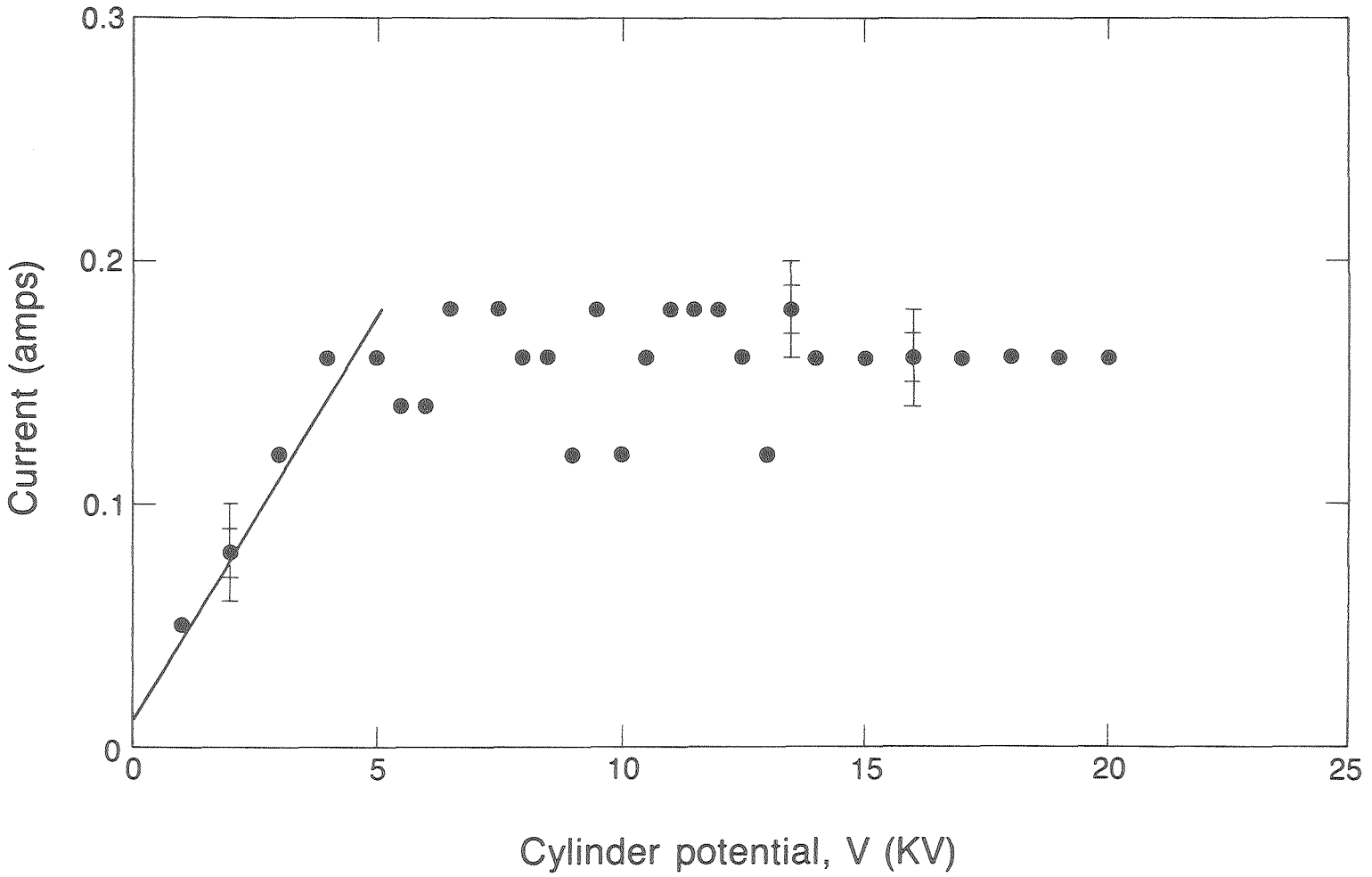

Figure 4.14 Configuration II: Pearson Probe Current Measuring Electron Energy Distribution

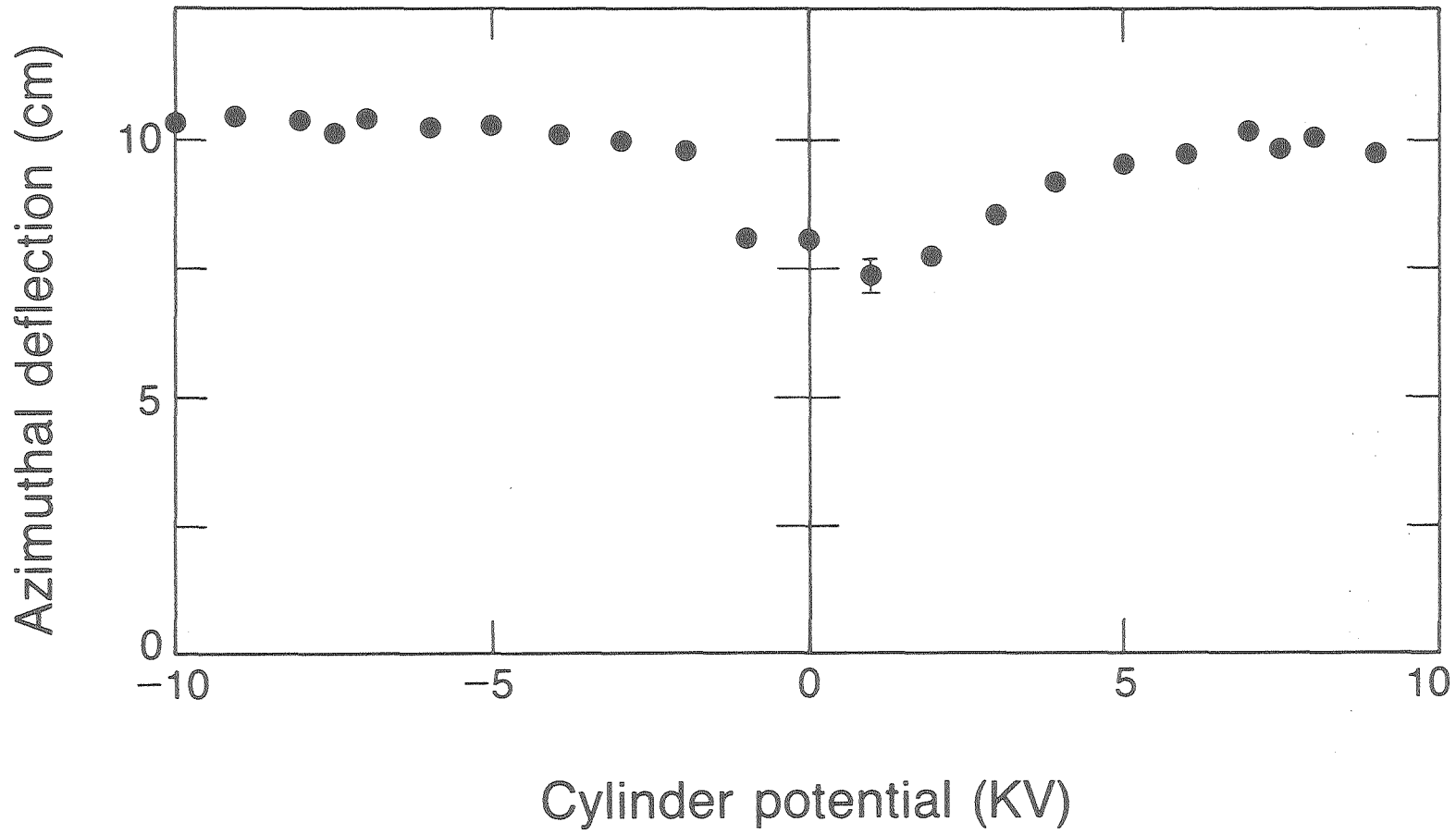

Figure 4.15 Azimuthal Deflection vs. Voltage Cylinder Bias at 16° E-Gun Angle

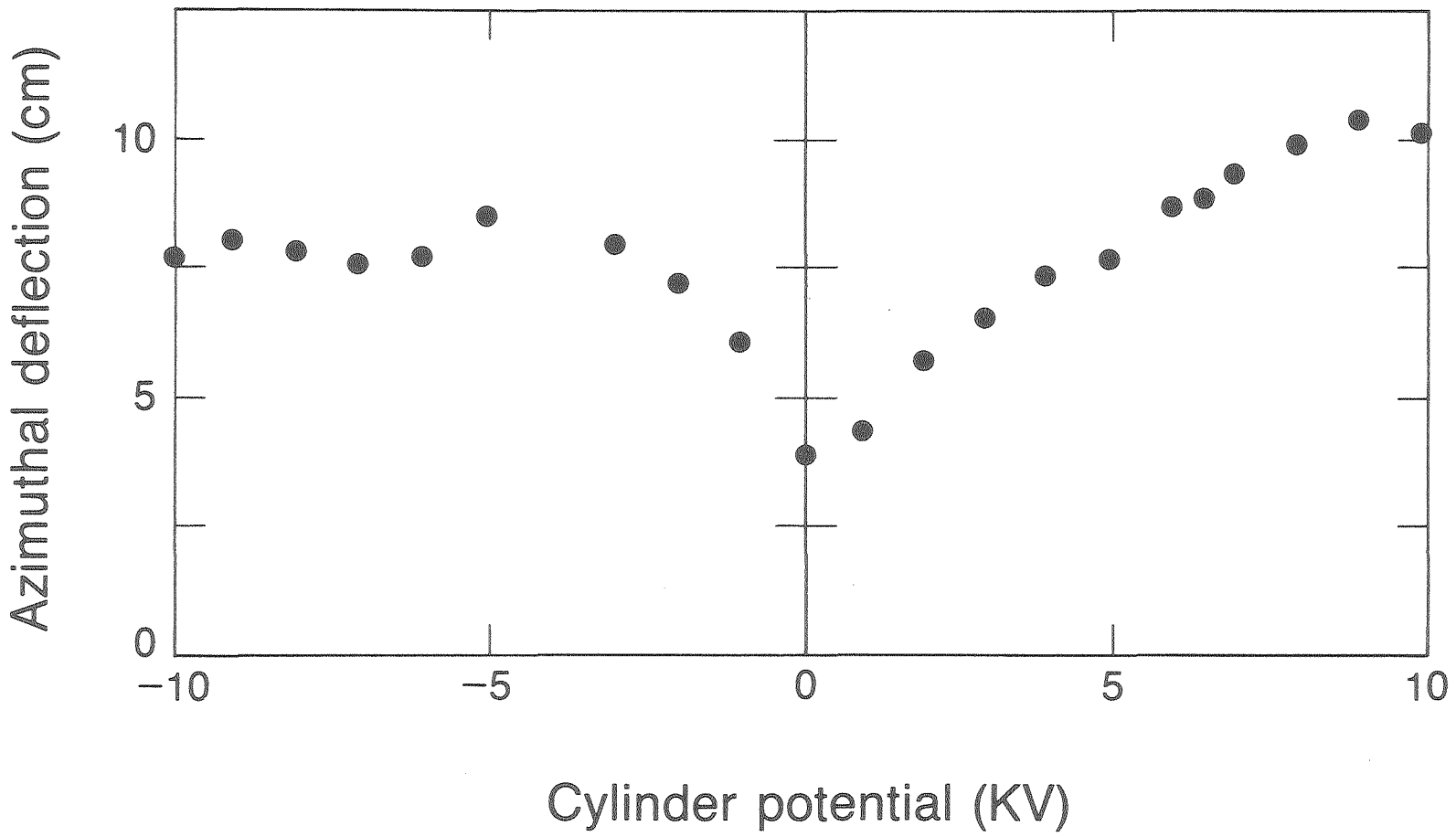

Figure 4.16 Azimuthal Deflection vs. Voltage Cylinder Bias at 32.5° E-Gun Angle

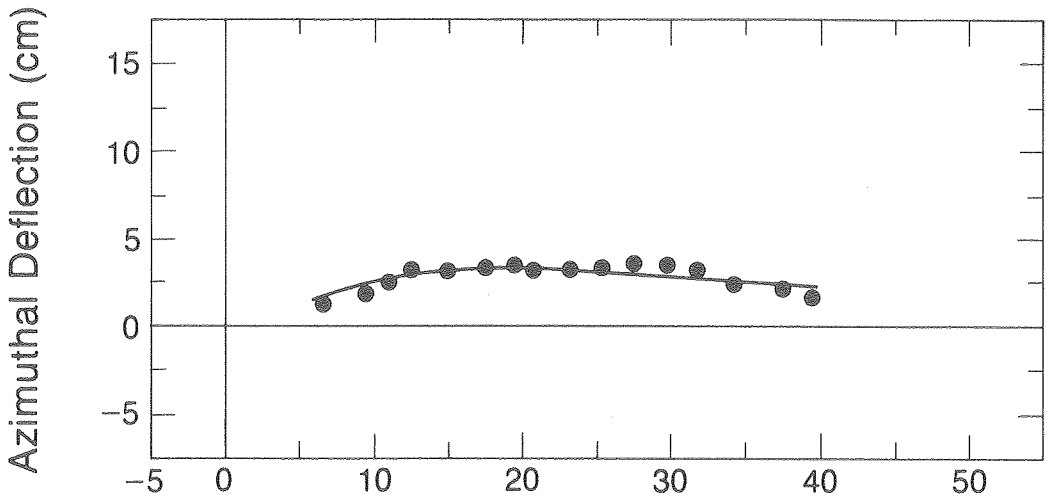

Figure 4.17A 6-30-82 Azimuthal Deflection Data and the Best Computer Fit

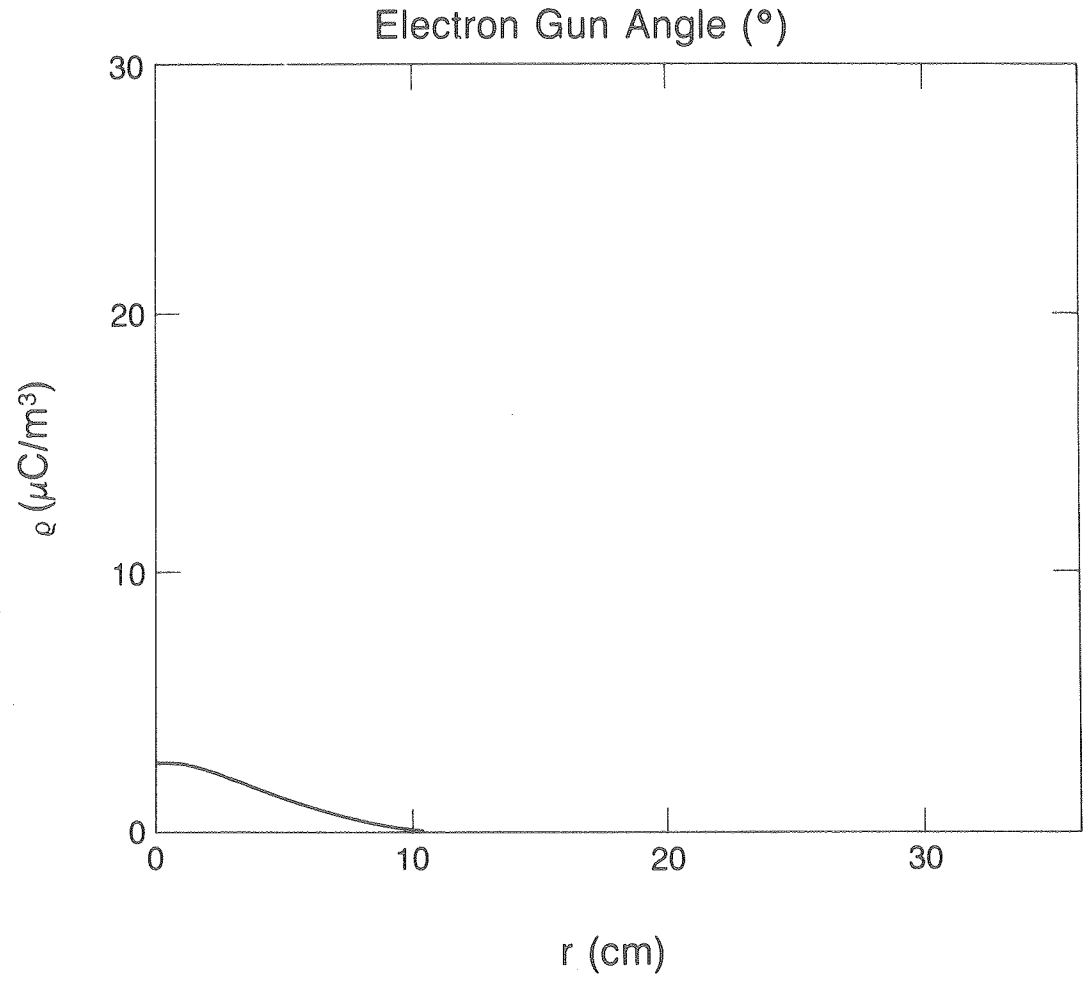

Figure 4.17B Model Charge Distribution Giving the Best Fit for 6-30-82 Data

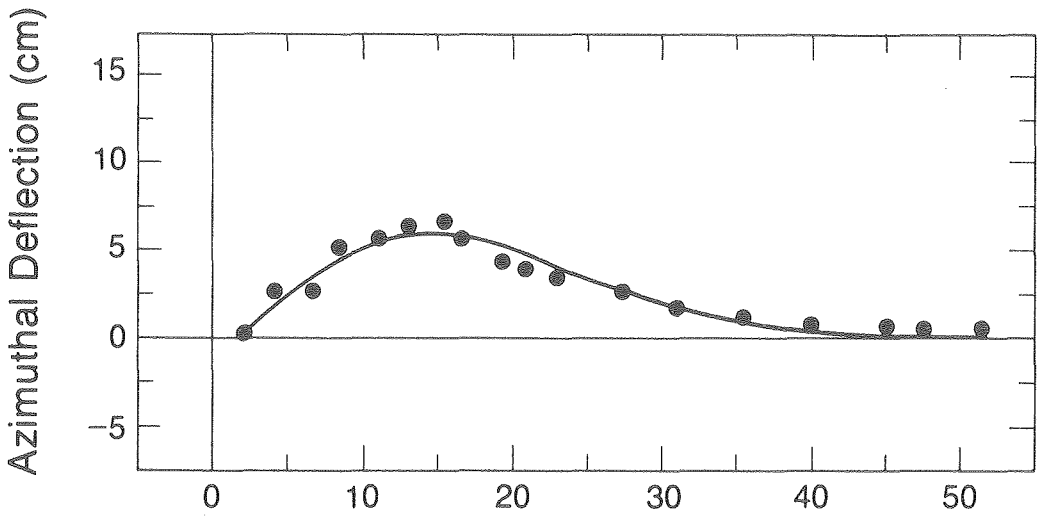

Figure 4.18A 6-30-82A Azimuthal Deflection Data and the Best Computer Fit

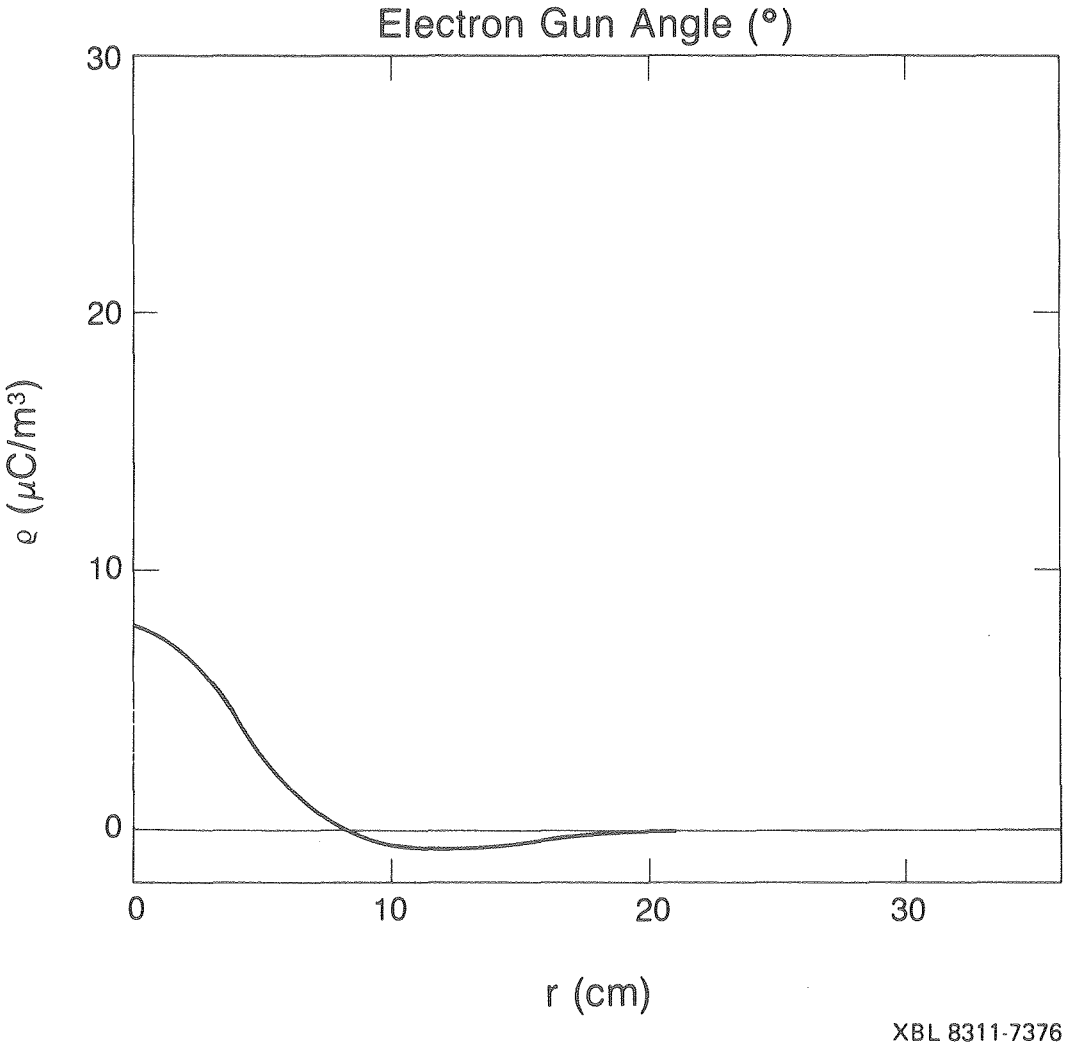

Figure 4.18B Model Charge Distribution Giving the Best Fit for 6-30-82A Data

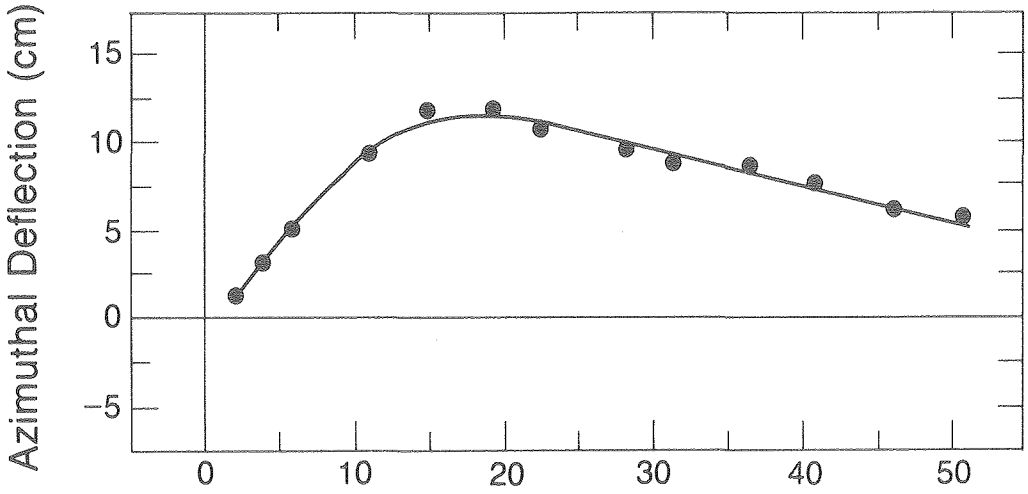

Figure 4.19A 6-30-82B Azimuthal Deflection Data and the Best Computer Fit

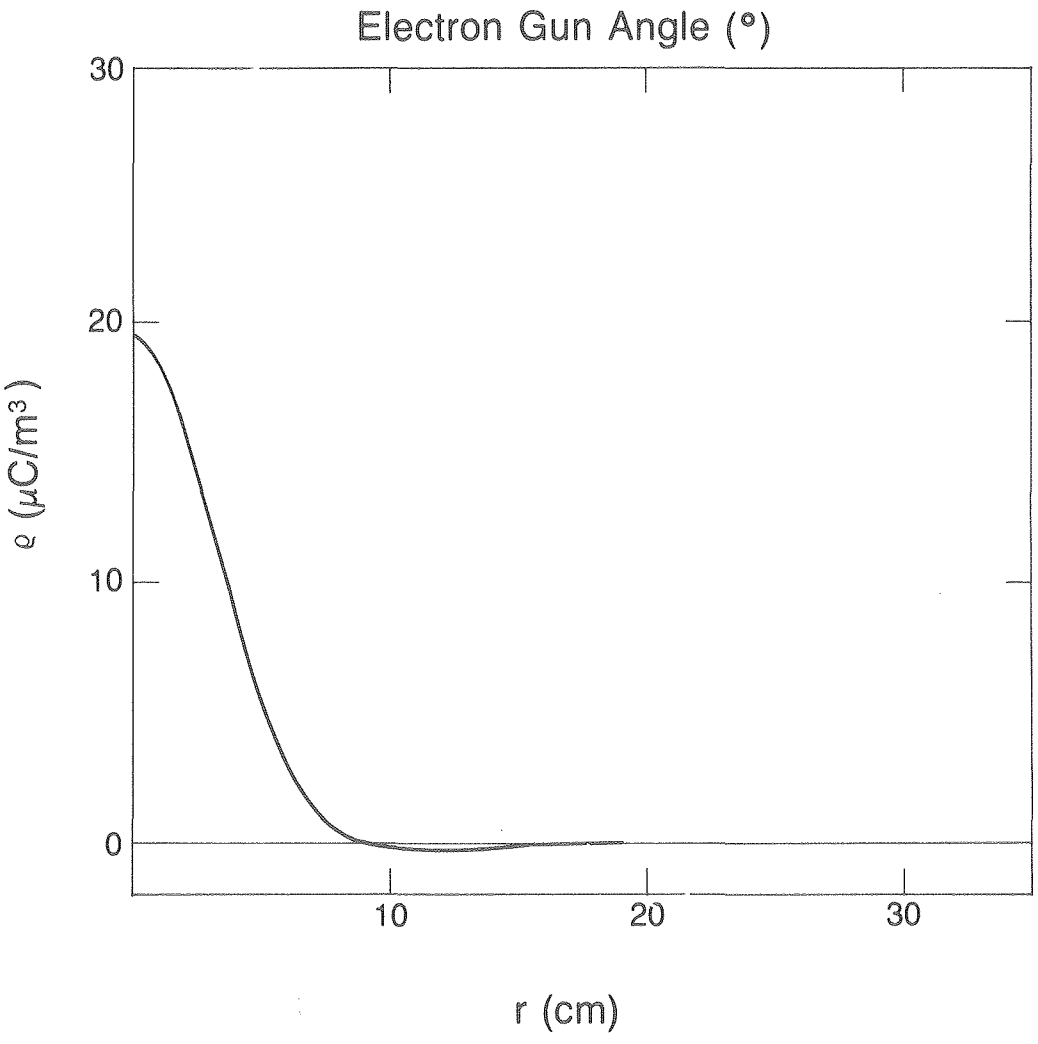

Figure 4.19B Model Charge Distribution Giving the Best Fit for 6-30-82B Data

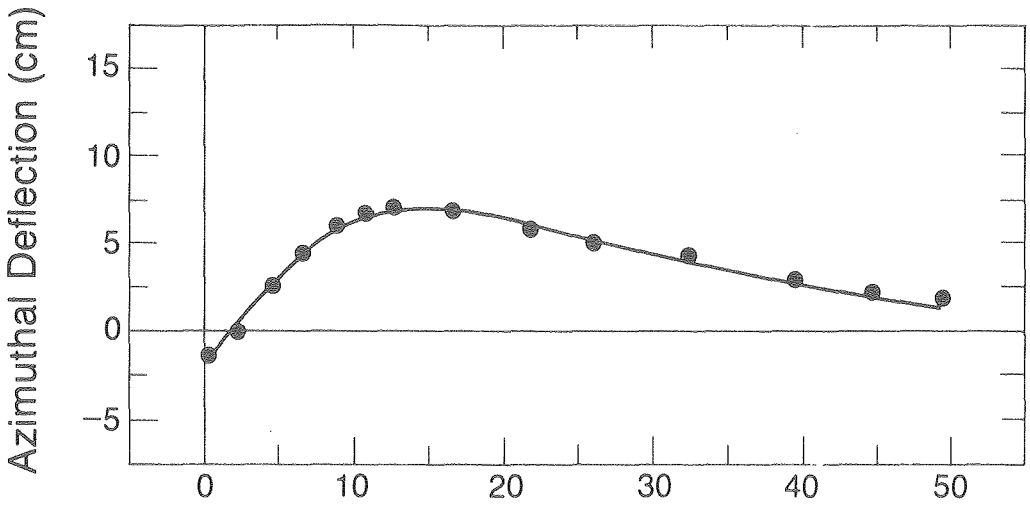

Figure 4.20A 6-30-82C Azimuthal Deflection Data and the Best Computer Fit

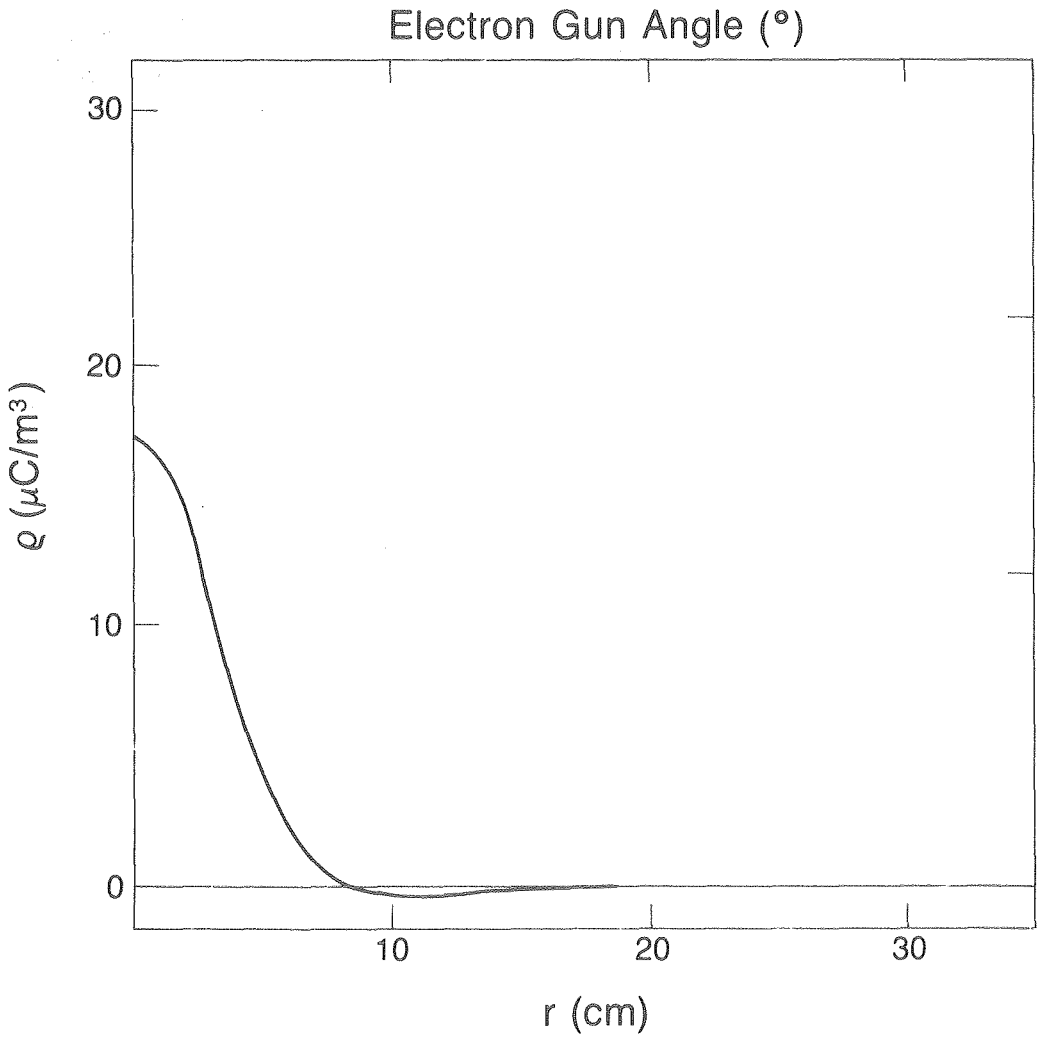

Figure 4.20B Model Charge Distribution Giving the Best Fit for 6-30-82C Data

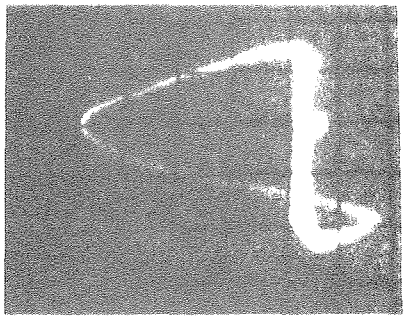

E=7kV
θ=17°

CONTINUOUS BEAM

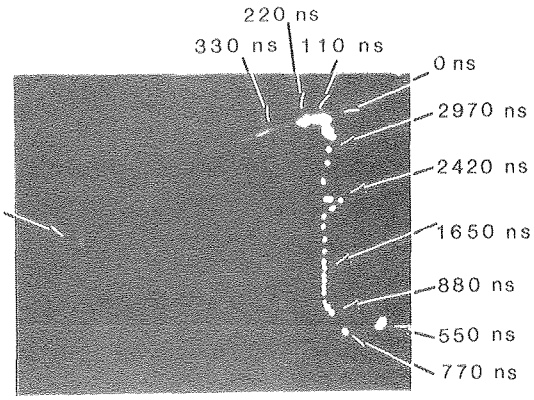

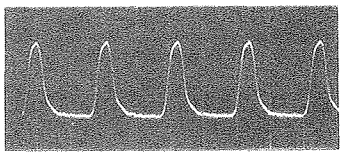

GATING PULSE
10 V/d 50 ns/d

CHOPPED BEAM

ION BEAM DIRECTION

SCALE: 2.5 cm/div

XBB 810-10250

Figure 4.21 A Time Resolved Trace

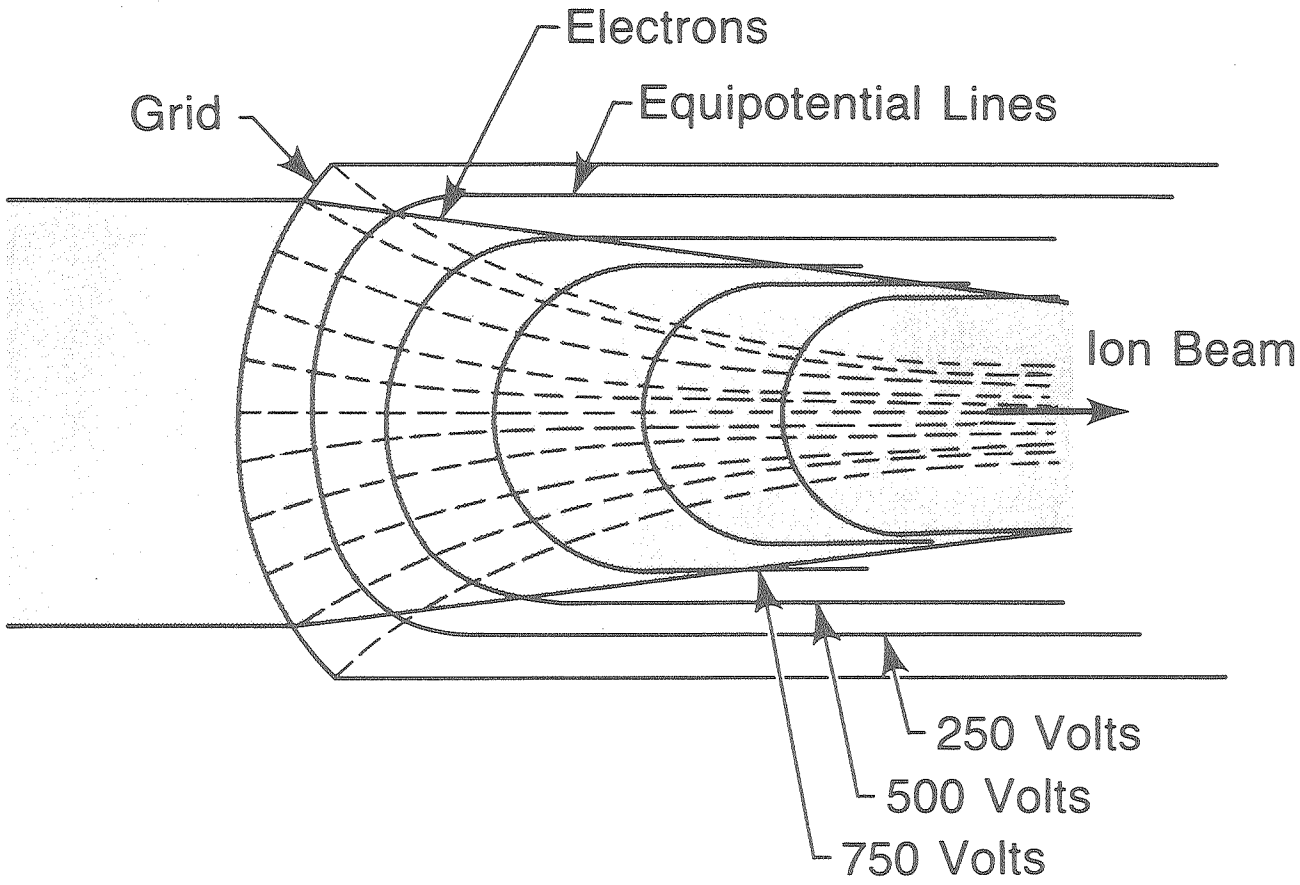

XBL 8312-7404

Figure 5.1 Electrons Streaming into Cesium Ion Beam

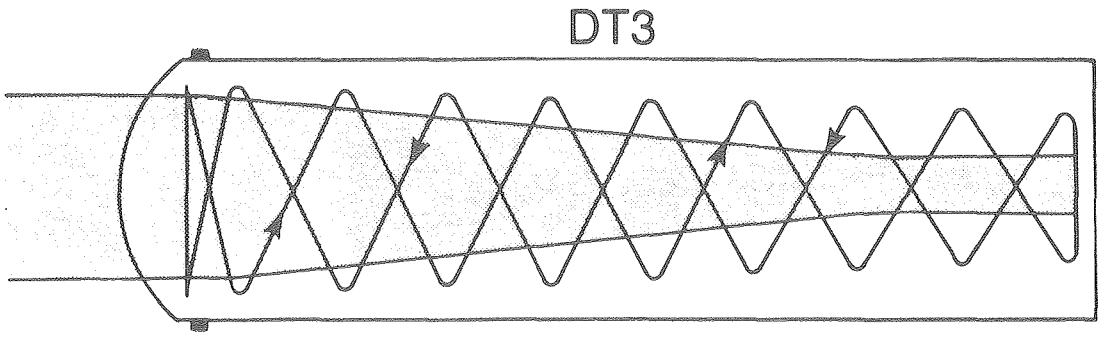

XBL 8312-7409

Figure 5.2 An Electron Trajectory in the Cesium Beam

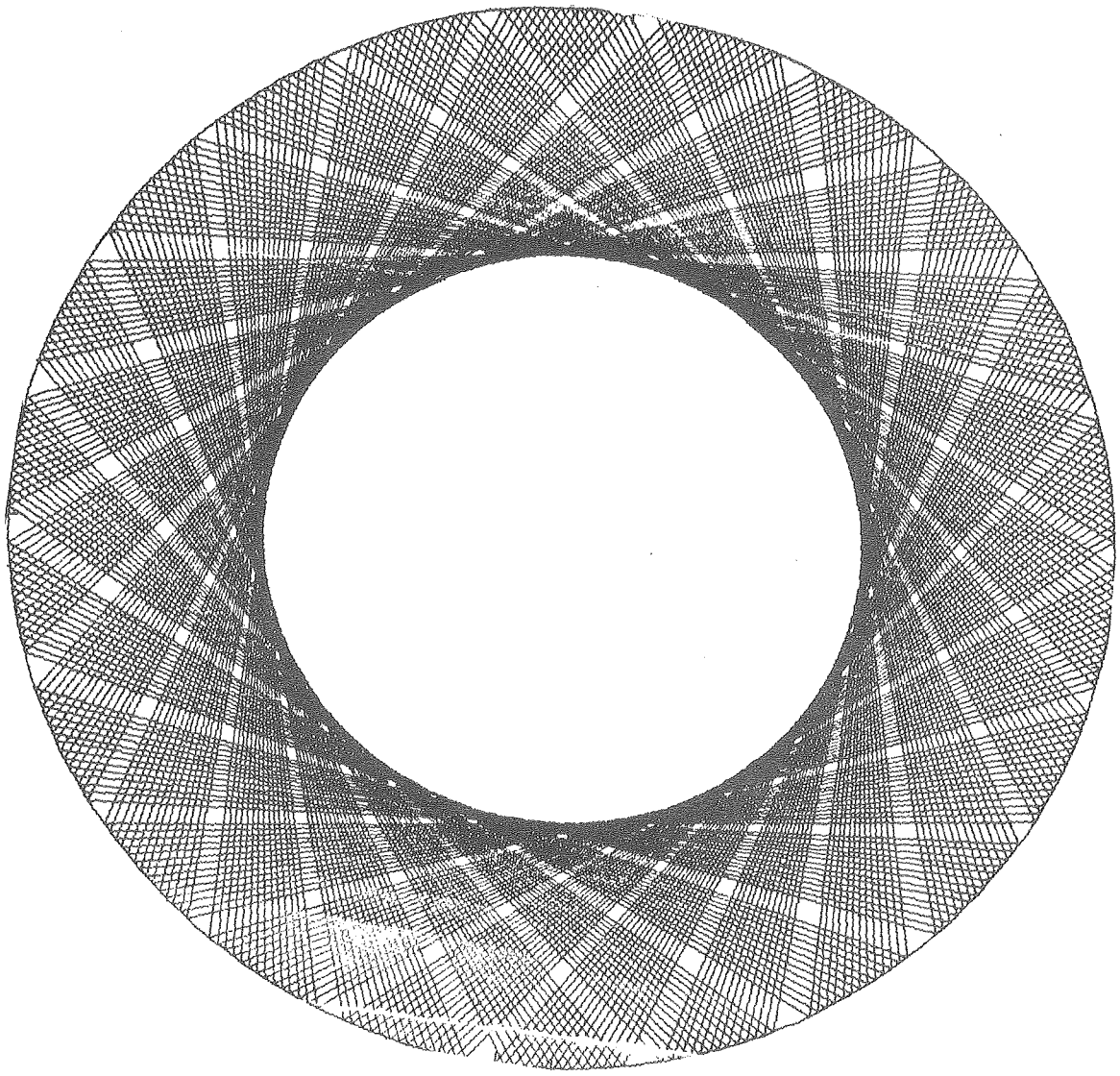

Figure 5.3A Electron Trajectory in a Circular "Waterbag" Potential

XBL 8312-2527

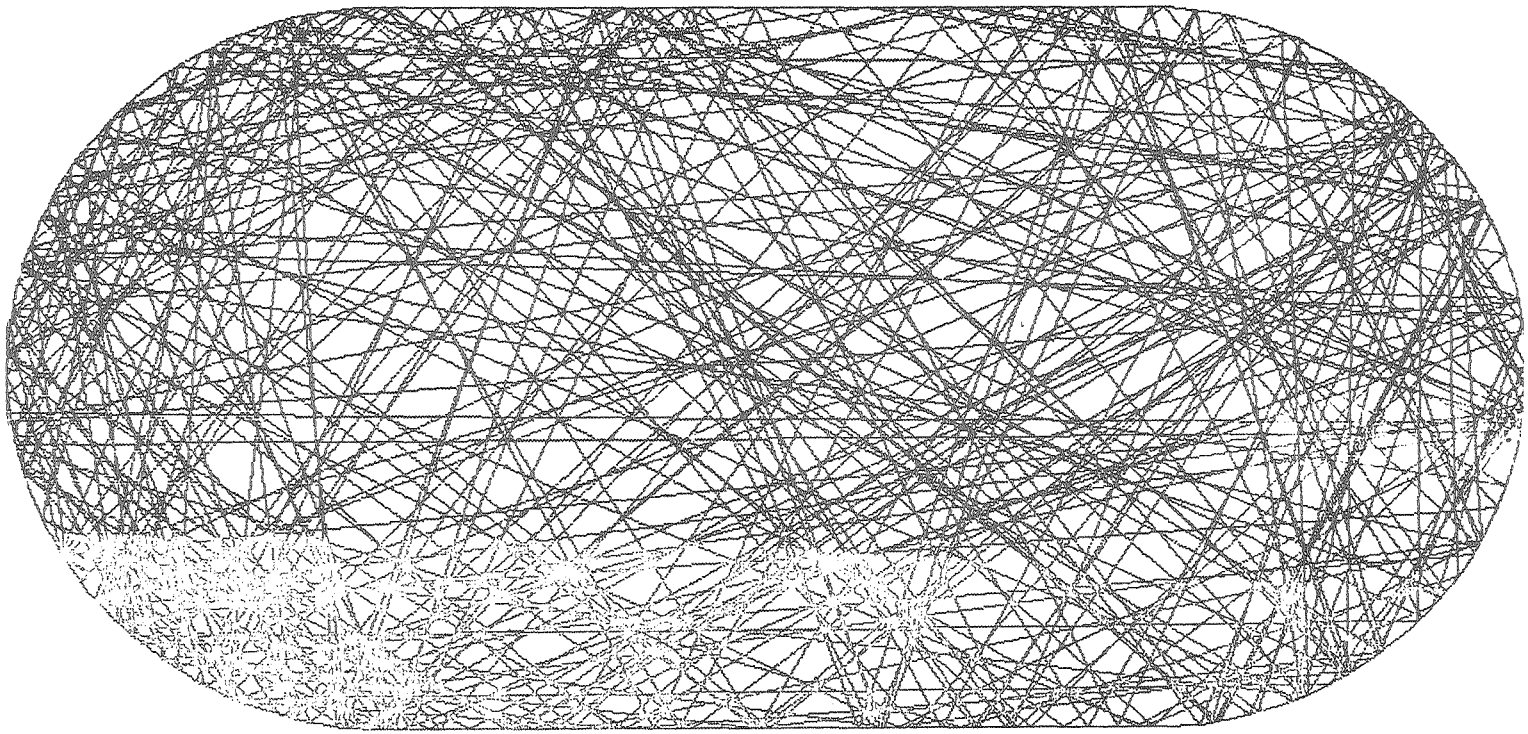

XBL 8312-2619

Figure 5.3B Electron Trajectory in a Stadium "Waterbag" Potential

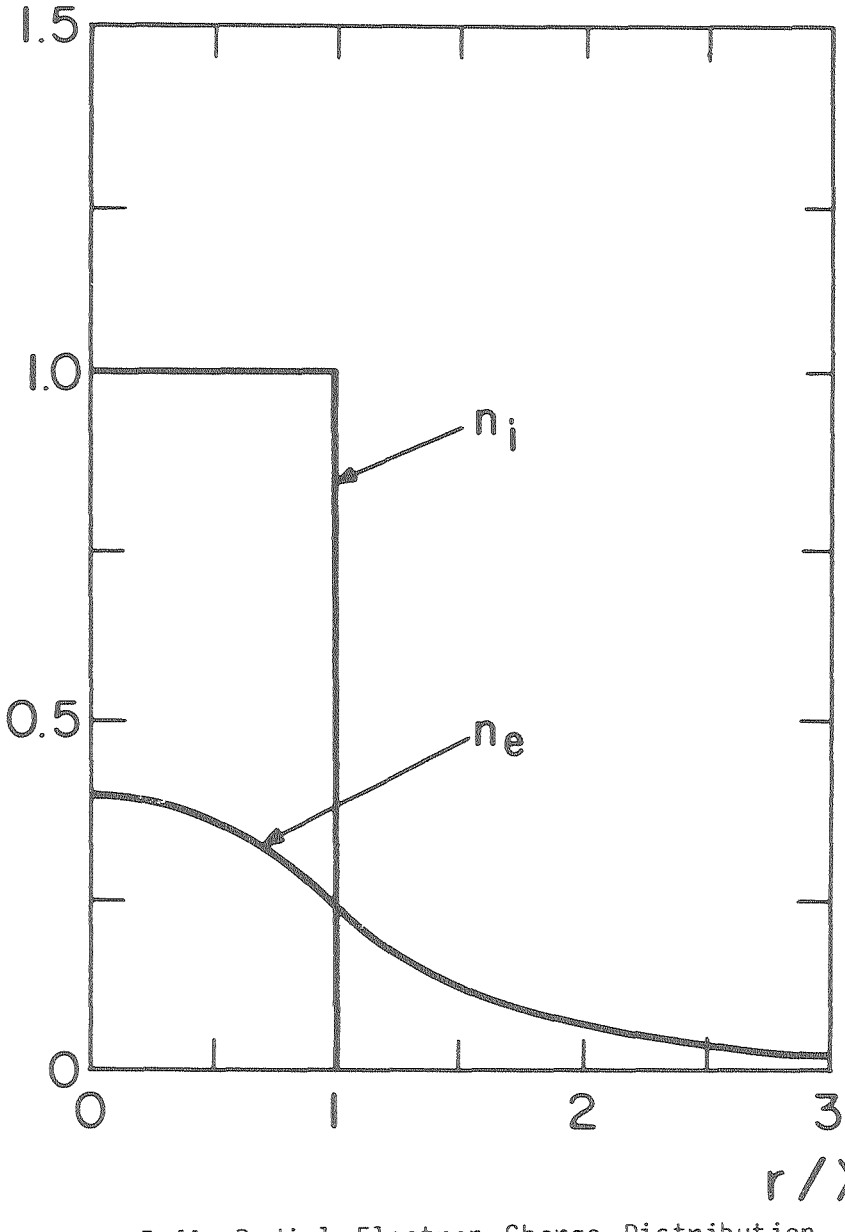

Figure 5.4A Radial Electron Charge Distribution for a Rectangular Radial Ion Charge Distribution for $R/\lambda_D = 1$

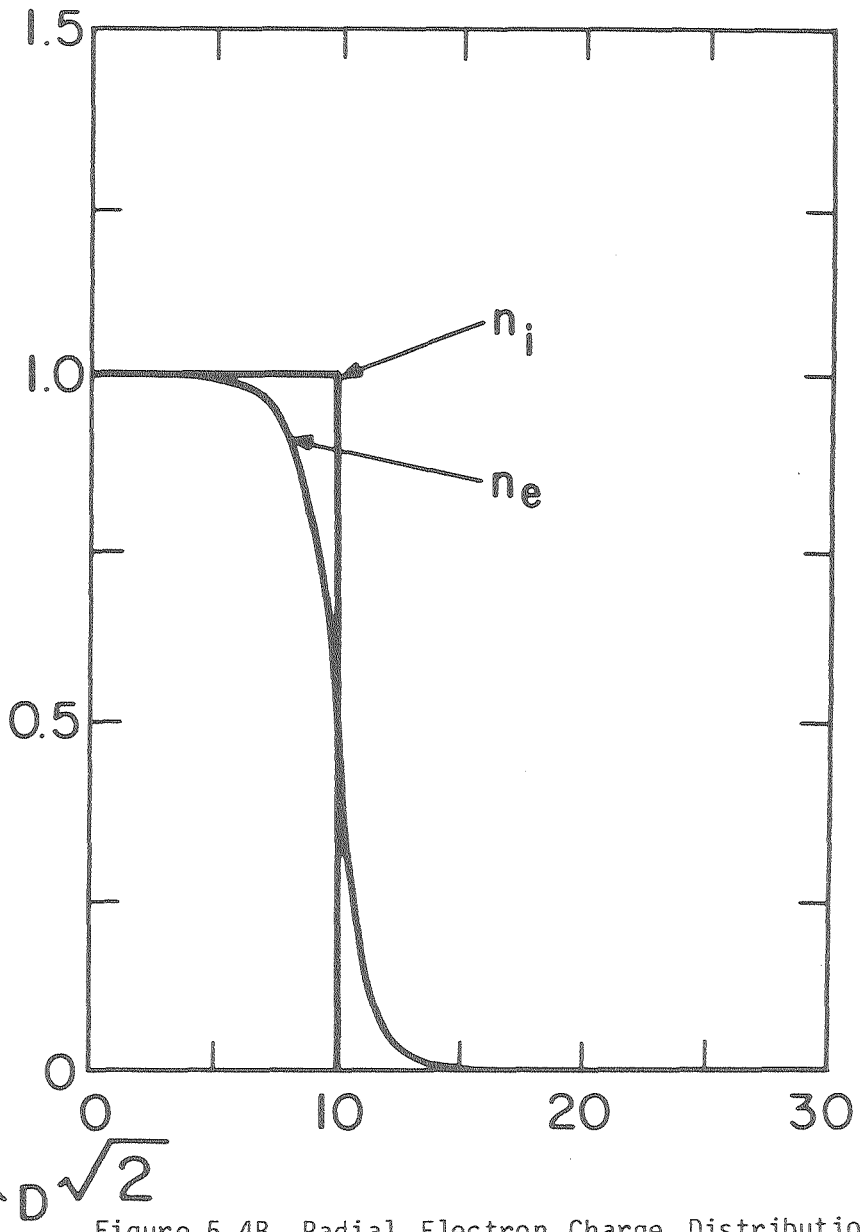

Figure 5.4B Radial Electron Charge Distribution for a Rectangular Radial Ion Charge Distribution for $R/\lambda_D = 10$

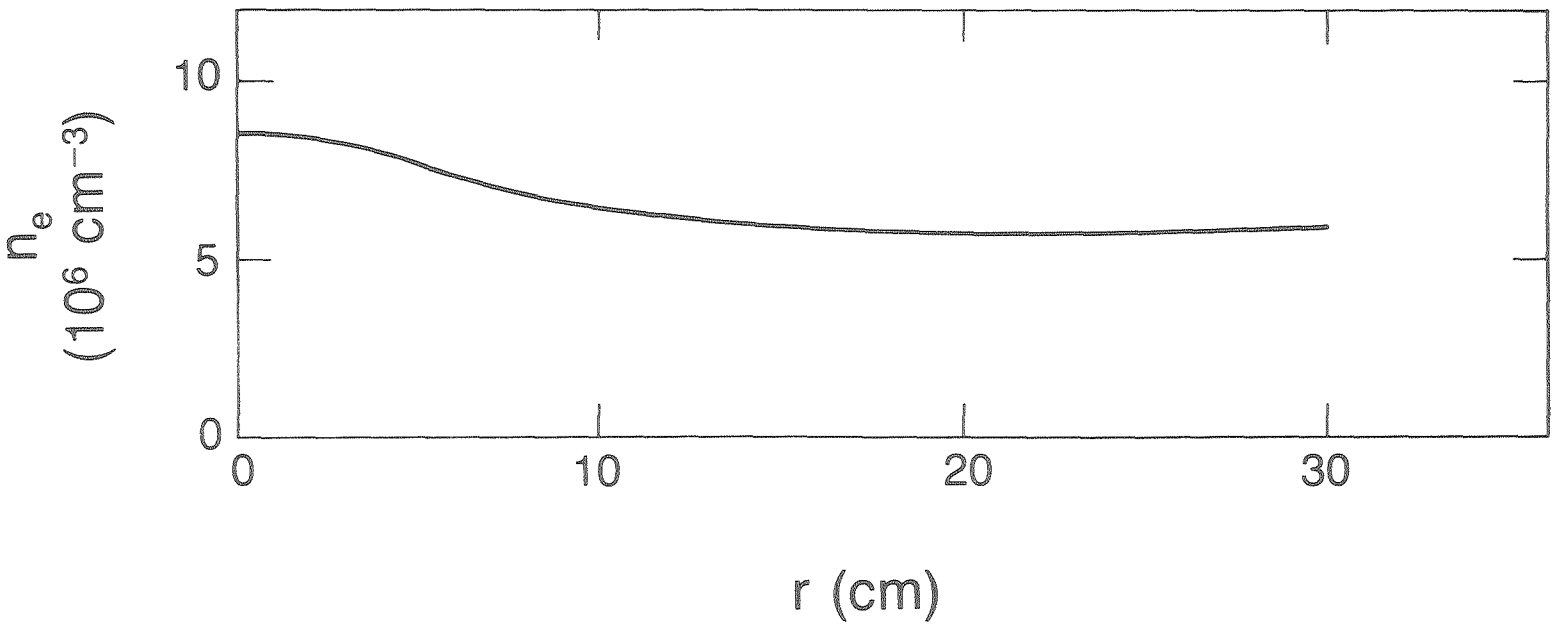

XBL 8311-7357

Figure 5.5 Radial Electron Charge Distribution for the Rigid Rotor Electron Model with $\omega << \omega_p/2$

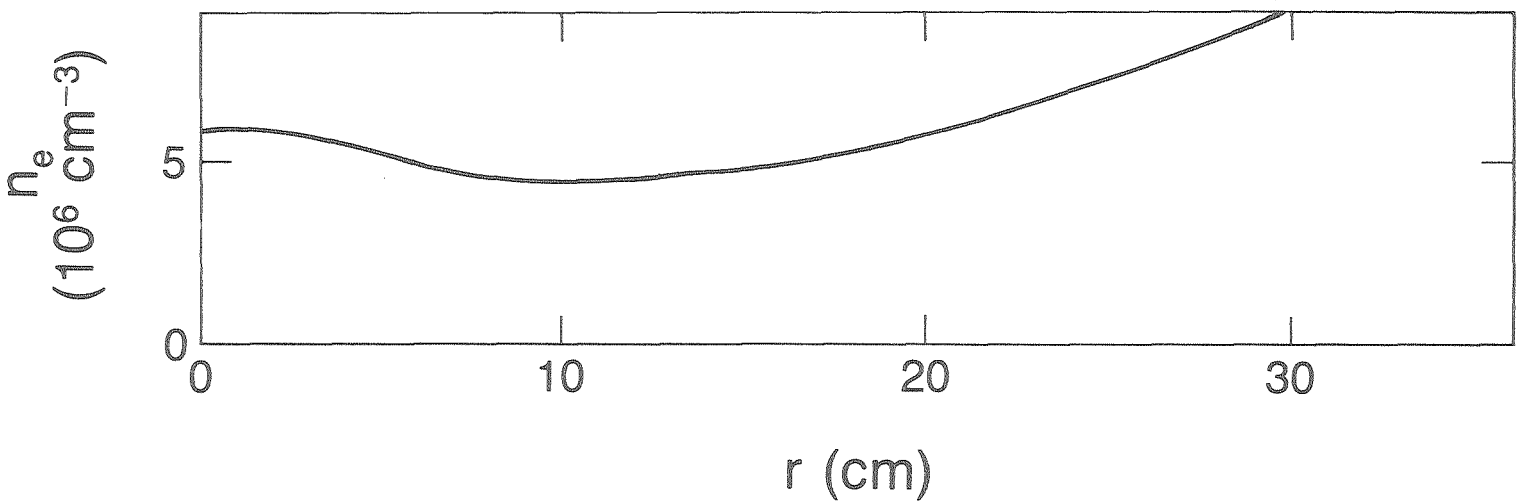

XBL 8311-7362

Figure 5.6 Radial Electron Charge Distribution for the Rigid Rotor Electron Model with $\omega \simeq \omega_p/2$

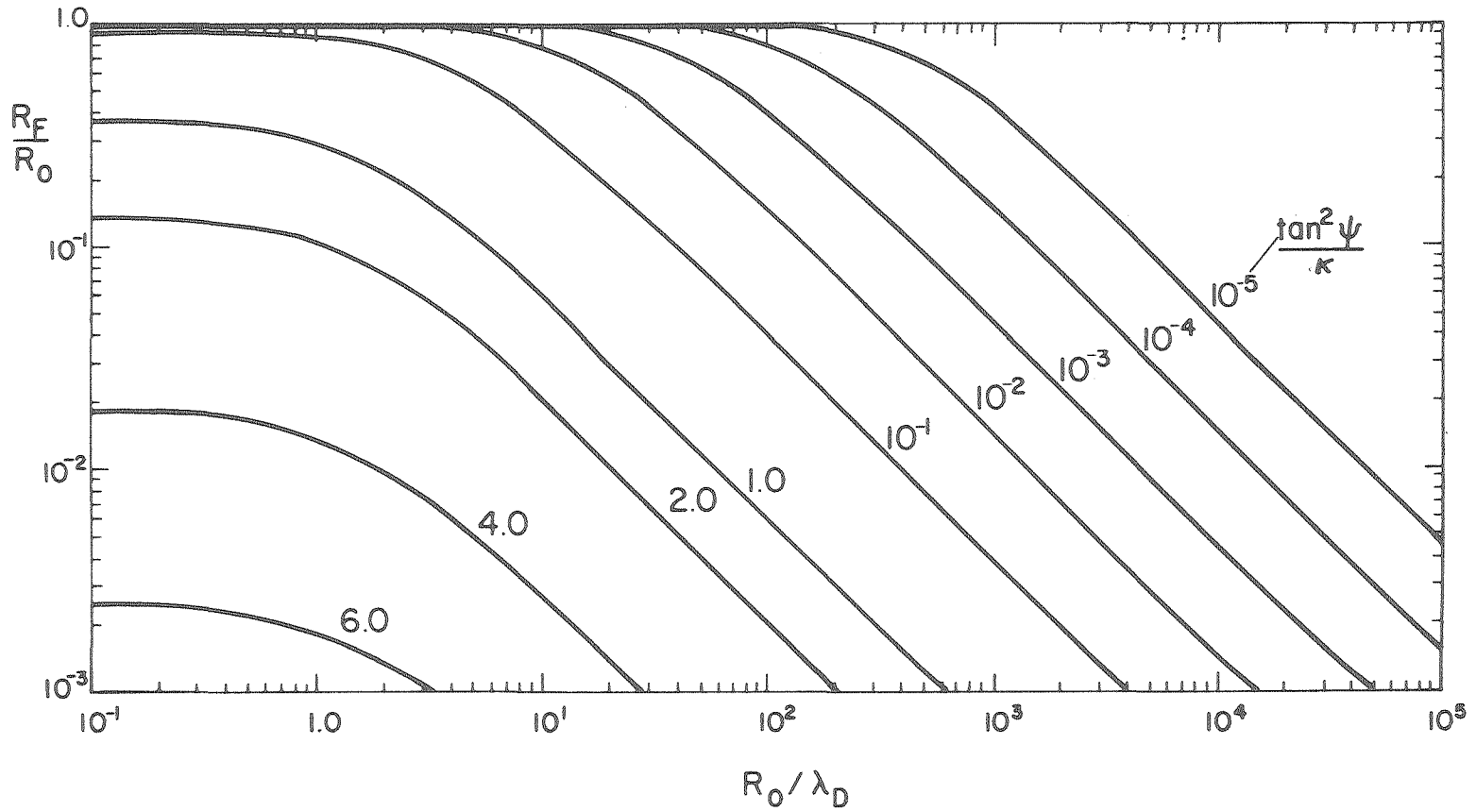

Figure 5.7 Solutions to the RMS Focal Spot Equation (Eq. 13), in Terms of Dimensionless Parameters R_F/R_0, R_0/λ_D, and $\tan^2\psi/k$. R_F is the Focused Beam Radius, R_0 is the Initial Beam Radius, λ_D is the Electron Debye Length, ψ is the Beam Focal Angle, and k is the Ion Beam Perveance

This report was done with support from the United States Energy Research and Development Administration. Any conclusions or opinions expressed in this report represent solely those of the author(s) and not necessarily those of The Regents of the University of California, the Lawrence Berkeley Laboratory or the United States Energy Research and Development Administration.